UNIVERSIDAD DE CHILE
FACULTAD DE CIENCIAS FÍSICAS Y MATEMÁTICAS
DEPARTAMENTO DE ASTRONOMÍA

THE ROLE OF GAS FRAGMENTATION IN THE FORMATION OF PRIMORDIAL SUPERMASSIVE BLACK HOLES

TESIS PARA OPTAR AL GRADO DE
MAGÍSTER EN CIENCIAS, MENCIÓN ASTRONOMÍA

MATÍAS ENRIQUE SUAZO CAMPOS

PROFESOR GUÍA:
ANDRÉS ESCALA ASTORQUIZA
PROFESOR CO-GUÍA:
JOAQUÍN PRIETO BRITO

MIEMBROS DE LA COMISIÓN:
WALTER MAX-MOERBECK ASTUDILLO
DOMINIK SCHLEICHER

Este trabajo ha sido parcialmente financiado por FONDECYT regular 1181663 y Centro de Excelencia en Astrofísica y Tecnologías Afines (PFB-06) que incluye el uso del cluster Geryon en el Centro de Astro-Ingeniería UC. Powered@NLHPC: Esta investigación fue parcialmente apoyada por la infraestructura de supercómputo del NLHPC (ECM-02)

SANTIAGO DE CHILE
2018

RESUMEN DE LA MEMORIA PARA OPTAR
AL TÍTULO DE MAGÍSTER EN CIENCIAS, MENCIÓN ASTRONOMÍA
POR: MATÍAS ENRIQUE SUAZO CAMPOS
FECHA: DICIEMBRE 2018
PROF. GUÍA: ANDRÉS ESCALA ASTORQUIZA

THE ROLE OF GAS FRAGMENTATION IN THE FORMATION OF PRIMORDIAL SUPERMASSIVE BLACK HOLES

El rol de la fragmentación del gas en la formación de agujeros negros supermasivos primordiales

En la presente tesis estudio cómo el proceso de fragmentación afecta la formación de las semillas de agujeros negros supermasivos primordiales utilizando simulaciones cosmológicas hidrodinámicas. Éstos se caracterizan por habitar los centros de los cuásares más brillantes observados en épocas muy tempranas del Universo. Debido a las limitaciones observacionales y a la complejidad de las ecuaciones que gobiernan los fenómenos, las simulaciones computacionales resultan ser la mejor forma de entender como estas estructuras se formaron.

En este trabajo se realizaron cincuenta simulaciones de baja resolución compuestas sólo de materia oscura con el fin de identificar los halos más prometedores para la formación de semillas masivas. Tres halos fueron elegidos con el fin de ser re-simulados con mayor resolución. El criterio de selección se basó en la rotación del halo y en la historia de fusión con otro halos. Lo anterior se realizó requiriendo que todos tuvieran una masa $> 5 \times 10^7$ $M_\odot$. Una vez escogidos los halos, se procedió a re-simularlos incluyéndose la física del gas, mayor resolución, y un fondo uniforme de radiación UV. Además se agregó un algoritmo para formar partículas sumidero, las cuales representan las estructuras no resueltas por el código. Los tres halos escogidos se re-simularon imponiendo dos condiciones de fondo UV: una de intensidad baja, $J_{21} = 10$, y otra de intensidad alta, $J_{21} = 10000$. Se observó que dos de las simulaciones bajo la influencia de un fondo de radiación UV de gran intensidad replicaron muy bien el modelo de colapso directo, en el cual el gas del halo colapsa directamente en un objeto muy masivo ($> 10^5$ $M_\odot$). Estas simulaciones formaron una única partícula sumidero, la que alcanzó masas mayores a 10^5 $M_\odot$ hacia el final de la simulación. En ambos casos la tasa de acreción se mantuvo mayor a 0.1 $M_\odot$/yr durante todo el tiempo que se mantuvo corriendo la simulación y no se observó fragmentación en estos casos. Por el contrario, en la re-simulación de un halo formado como resultado de una gran cantidad de fusiones, una estructura espiral se formó en los 5 pársec centrales. Dicha estructura se fragmentó formando varias partículas sumidero. La primera que se formó alcanzó una masa cercana a los 10^5 $M_\odot$, mientras que las demás alcanzaron masas intermedias entre 10^3 $M_\odot$ y 5×10^4 $M_\odot$. Las simulaciones con un fondo de radiación UV de baja intensidad revelaron en todos los casos fragmentación y formación de varias partículas sumidero. En estos casos las partículas más masivas alcanzaron masas del orden de 10^4 $M_\odot$, la cual es menor que en el caso anterior, pero sigue siendo relevante para la formación de semillas masivas. Como se formaron varias partículas sumidero en todos estos casos, éstas están más propensas a interactuar entre ellas, pudiendo fusionarse intensificando su tasa de acreción, lo cual efectivamente se observó. Finalmente se concluye que la fragmentación no es un impedimento para la formación de semillas masivas, y que la dinámica de los sistemas es relevante para la formación y evolución de las mismas.

Soy humano, luego científico

Agradecimientos

Es realmente díficil para mi acotar los agradecimientos en una sola página, sobre todo sintiendo que cada persona que he conocido ya sea para bien o para mal ha contribuido de alguna manera en mi crecimiento personal y ha moldeado al ser humano que soy, del cual estoy muy orgulloso.

En primer lugar daré gracias a mi familia, quienes han sido la base de mi formación y a quienes siempre deberé mis logros. A mis hermanas Tamara y Johanna, cuyo apoyo incondicional me ha impulsado a perseguir mis metas. A mi tía Irene, quien ha sido el pilar fundamental de mi crianza y mi formación humana. A mi papá, quien me entregó todas las herramientas matemáticas y científicas para estar donde estoy. También agradezco el apoyo con el que he contado por parte de mi tía Mariana, mi primo Roberto y Dantito.

No puedo dejar de agradecer a los amigos que he hecho durante las distintas etapas de mi vida. Agradeceré principalmente a la Coni y a la Pola, cuyo apoyo fue fundamental durante mi estadía en Calán, siendo ambas el soporte principal de mi salud y de mi crecimiento personal durante este proceso. Agradezco también a mi querida pandilla, quienes me demostraron que es posible una amistad sincera: Aurora, Mireya, Camilo, Pablo, Sotito, Pelo, Karina y Calsito, los quiero mucho. También agradezco a la buena oficina, cuya simpatía y valores afines a los míos me hicieron sentir cómodo desde que llegué a Calán: Elise, Jose, Mari y Bica, atesoraré mucho la comunidad que generamos. Mención honrosa a la Tere Paneque. Agradezco también a mis amigos del colegio, Gerardo y Pelao, quienes siempre me han brindado su amistad, y con los que siempre podré contar.

También agradezco a los funcionarios, quienes hacen cada día de Calán un lugar mejor con su buena onda: el Ale, la Nati, Don Mario, la señora Nelly, la señora Jessica, la señora Mari, la Sonia, y David. Incluyo barsamente al Lander y a Camilo en esta lista. Añado finalmente a la Marta, con quién se gestó una muy entretenida relación de complicidad desde aquel memorable primer día, sin duda serás a quien más extrañaré de Calán.

Finalmente agradezco a Joaquín por el apoyo brindado desde que llegué, y por el apoyo incondicional a perseguir mis planes futuros. También agradezco a Andrés, por el apoyo y por su forma distinta de ver las cosas. Siento que ser guiado por ustedes me hizo crecer mucho como persona, y a convertirme en un científico más independiente. También agradezco a Dominik, por toda la crítica constructiva que he recibido desde que nos conocimos, me alegra mucho que existan científicos como tú.

Contents

List of Tables viii

List of Figures ix

Introduction 1
0.1 Structure formation . . . 2
0.2 Supermassive black hole formation . . . 4
0.3 Thesis outline . . . 9

1 Methodology 11
1.1 RAMSES . . . 11
1.1.1 Adaptive Mesh Refinement . . . 11
1.1.2 N-body solver . . . 13
1.1.3 Hydrodynamical solver . . . 16
1.1.4 Cosmological settings . . . 17
1.2 Complementary tools . . . 18
1.2.1 KROME . . . 18
1.2.2 MUSIC . . . 25
1.2.3 Sink Particles . . . 26
1.3 Modifications to the RAMSES code . . . 31
1.3.1 RAMSES . . . 31
1.3.2 Sink particles . . . 31

2 Dark Matter-only simulations 34

3 Hydrodynamic simulations 39
3.0.1 High UV intensity . . . 40
3.0.2 Low UV intensity . . . 53
3.0.3 Extended UV intensity cases . . . 63
3.0.4 Accretion Rates . . . 65

4 Discussion 68

Conclusion 71

Bibliography 73

List of Tables

1.1 Initial abundances for all chemical species included in the simulation 19
1.2 Chemical reactions considered in the simulations 20
1.3 Chemical reactions for deuteride species 24
1.4 Parameters set in the MUSIC code. 26

2.1 Features of halos selected to be re-simulated. 38

3.1 Sink features for the simulations 39
3.2 Sink features for the simulations 40
3.3 Averaged growth time for re-simulated halos under the influence of a strong UV background 43

List of Figures

1 Universe evolution scheme in the actual paradigm 2
2 Large-Scale simulation of the Universe 3
3 Spectrum of J1342+0928 4
4 Summary of possible pathways to form a SMBH seed 5
5 Artistic representation of Pop III stars 6
6 Cooling function for a primordial chemical environment 7

1.1 Example of FTT for a two dimensional Cartesian grid 12
1.2 Working principle of the clumpfinder 29
1.3 Comparison between methods to form sink particles 33

2.1 Dark-matter particle projection plot for a sample simulation 35
2.2 Mass distribution for all dark matter halos simulated 36
2.3 Bullock spin parameter distribution for dark matter halos simulated 37
2.4 Merger-trees halos selected to be re-simulated 38

3.1 Growth time for the high UV intensity runs 41
3.2 Density projections for re-simulated halos under the influence of a strong UV background at 3 kpc and 100 pc 41
3.3 Density projections for re-simulated halos under the presence of a strong UV background at 5 pc 42
3.4 Distance between the first sink particle formed and the ones formed later in halo C 44
3.5 Toomre parameter for halo C 45
3.6 Radial profiles for the $J_{21} = 10000$ runs. 47
3.7 Phase diagrams for halo C under the presence of a high UV background. . . 48
3.8 Temperature and H_2 fraction projections for halo C re-simulations irradiated by a strong UV flux. 49
3.9 Electron fraction for halo C re-simulation irradiated by a UV background of $J_{21} = 10000$ at a scale of 5 pc. Two epochs are shown, Δt represents the age of the simulation relative to the age of the first sink particle formed in the respective run. 50
3.10 Mass and accretion rate time evolution for the $J_{21} = 10000$ runs 52
3.11 Growth time in the low UV intensity simulations 53
3.12 Density projection at 100 pc for halos under the influence of a low UV background 55
3.13 Density projection at 5 pc for halos under the influence of a low UV background 56
3.14 Distance between two sink particles 57

3.15 Density projection for the central 2.5 pc in halo B 58
3.16 Distances to the most massive sink particle as a function of time for halos B and C. 59
3.17 Radial profiles for the $J_{21} = 10$ runs 62
3.18 Mass and accretion rate time evolution for the $J_{21} = 10$ runs 63
3.19 Density projection for re-simulated halos irradiated by a UV background of $J_{21} = 100$ 64
3.20 Density projections for the re-simulation of halo B under the influence of a uniform UV background of $J_{21} = 5$ 65
3.21 Accretion rate time evolution for halo A with no smoothing. Every color represents a sink particle, they are the same used for halo A in Figure 3.18. . 66
3.22 Accretion rate time evolution for halo B with no smoothing. Every color represents a sink particle, they are the same used for halo B in Figure 3.18. . 67

4.1 Critical UV intensity as a function of radiative spectra temperature 70

Introduction

The current understanding of the Universe is based on the Big Bang theory, in which all elementary particles were created at the very beginning, and the Universe has expanded since its creation.

According to this picture, at the beginning the Universe was very dense, and hot that all types of energy and matter were coupled into a single state. Though it is known that the Universe has always been expanding (Hubble, 1929; Lemaître, 1931), there was a very short, but intense expanding period called *Cosmic Inflation* (Guth, 1981). This period has been invoked to explain some phenomena observed in the Universe, like its flatness and the absence of magnetic monopoles. There is no information about what happened previous to this epoch. After inflation, the Universe became colder as it expanded, and subatomic particles formed, this process occurred in less than the first 10 seconds after the Big Bang. Then, protons and neutrons arose as a consequence of the stable association of these subatomic particles, which led to the formation of atomic nuclei. The process of nuclei formation is known as Big Bang nucleosynthesis, and it ended by 20 minutes after the Big Bang. For further reading on this topic see Steigman (2007). From this event $\sim 75\%$ of matter turned into Hydrogen, $\sim 25\%$ became Helium, and deuterium and lithium also formed, but in small traces. For thousands of years, the Universe was too hot to allow the formation of electrically neutral atoms (Peebles, 1968; Zeldovich et al., 1968). But, roughly 370000 yrs after the Big Bang, the temperature dropped to values cool enough to allow the recombination of electrons and ions, leading to the formation of neutral atoms. Unlike plasma, electrically neutral atoms are transparent to many electromagnetic wavelengths, which means the decoupling of both components. The radiation at the time of recombination is observed today, and it is known as a cosmic microwave background (Penzias & Wilson, 1965; Bennett et al., 1996; Hinshaw et al., 2007). After this era, the Universe continued its expansion, hence, its cooling in the so-called Dark Ages, since it contained mainly neutral atoms, and no luminous structures existed to be observed. Though this era may look monotonous, matter attracted each other gravitationally, initial primordial fluctuations amplified and dark matter re-arranged following these perturbations (Harrison, 1970; Zeldovich, 1972; Springel et al., 2005). This phenomenon produced huge potential wells, in which baryons fell and started to form galaxies (Evrard, 1990; Navarro & White, 1993; Bryan et al., 1994) building up what we know as the *Cosmic Web*. In Figure 1 we observe a simplified scheme for the Universe evolution, it includes the development of structures found today, like planets, stars, and galaxies. It also emphasizes that we are in a period dominated by the dark energy accelerated expansion (Perlmutter et al., 1998, 1999; Riess et al., 1998; Schmidt et al., 1998).

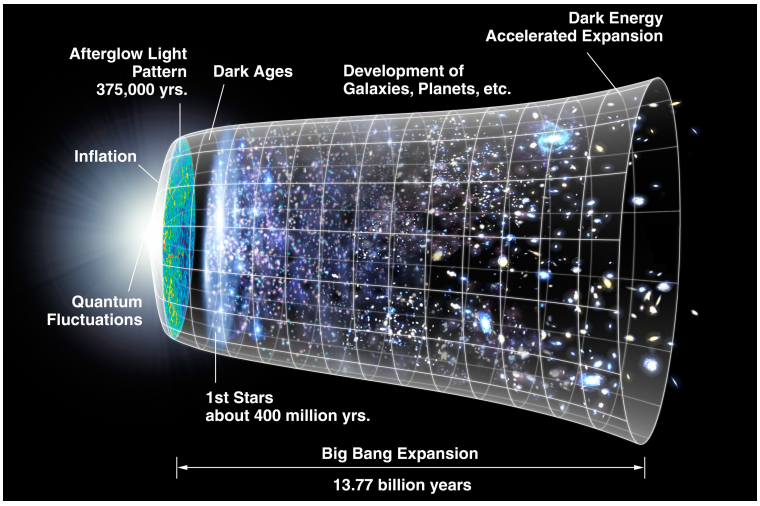

Figure 1: Universe evolution scheme in the actual paradigm. Image credit NASA.

0.1 Structure formation

The Universe is expected to be homogeneous and isotropic at scales larger than 100 Mpc, as it is seen in the cosmic microwave background. Friedmann's equation (1) is obtained by making use of these properties in Einstein's equation. From equation (1), we can understand how the Universe evolves taking into account all its components (baryons, photons, neutrinos, dark matter, dark energy, curvature, etc.).

$$\left(\frac{\dot{a}}{a}\right)^2 = \frac{8\pi G}{3}\rho - \frac{kc^2}{a^2} \tag{1}$$

In the equation above a is the scale factor, ρ is the energy-matter density (includes baryons, dark matter, dark energy, etc.), k is the space curvature, G is the gravitational constant, and c is the speed of light.

We can consider that the Universe has three kinds of components: Radiation, Matter and Dark Energy. Every single one is important in the evolution of large-scale dynamics, but depending on the epoch, one of them has always been more significant than the others. Therefore, three eras can be identified, from which Friedmann's equation (1) can be solved analytically (for the flat Universe case, $k = 0$):

- Radiation dominated era (From inflation up to $z \sim 3600$): In this era $\rho_{\text{rad}} \propto a(t)^{-4}$, so $a(t) \propto t^{1/2}$
- Matter dominated era (From $z \sim 3600$ up to $z \sim 0.3$): In this era $\rho_{\text{matter}} \propto a(t)^{-3}$, so $a(t) \propto t^{2/3}$
- Dark-Energy dominated era (From $z \sim 0.3$ up today): In this era $\rho_\Lambda \propto cte.$, so $a(t) \propto \exp(Ht)$, where $H = \sqrt{8\pi G\rho_\Lambda/3}$

Matter is considered to have two components; Baryons and Dark Matter. Baryons are

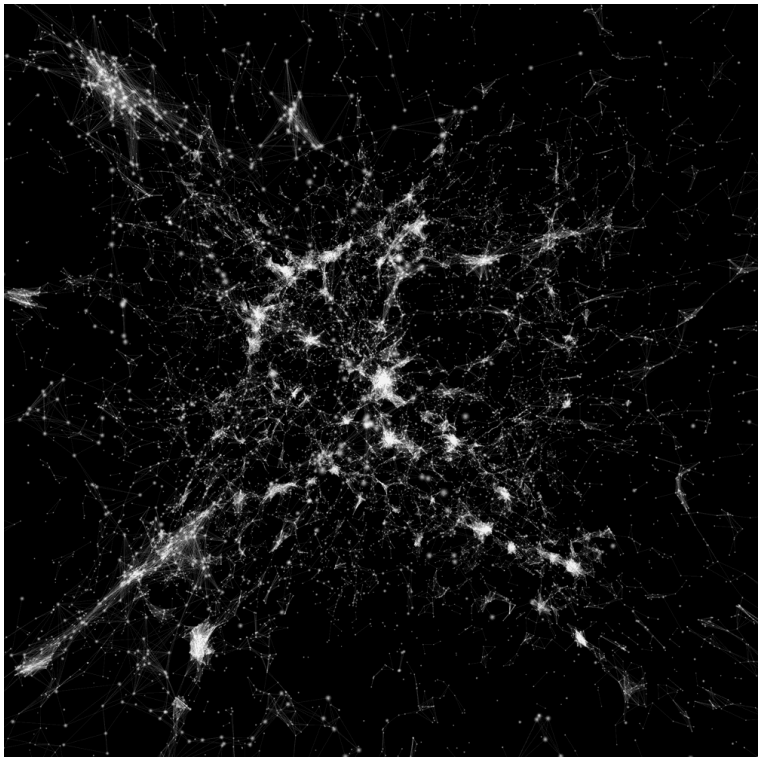

Figure 2: Large-Scale simulation of the Universe. Simulation performed by the Illustris collaboration. Illustration taken from http://cosmicweb.kimalbrecht.com.

ordinary matter that can absorb and emit radiation, while dark matter is an unknown kind of matter that just interacts through gravitation. Observational evidence shows that dark matter is about five times more abundant than baryons (Planck Collaboration et al., 2016).

Dark matter plays a crucial role in structure formation because it feels only the force of gravity. This effect leads to gravitational instabilities which allow compact structures to form not opposed by any force, such as radiation pressure. As a result, dark matter begins to collapse into a complex network of dark matter halos before ordinary matter, which is impeded by pressure forces.

The Universe is known not to be perfectly homogeneous nor isotropic, since small random fluctuations arose due to quantum phenomena in the primeval Universe (Pagels, 1983). These tiny fluctuations grew with the Universe allowing the Jeans instability to be triggered in regions where these fluctuations where larger, decoupling from the Universe expansion at a time called *turnaround*. This process shaped the large scale structure. In Figure 2 we observe the large-scale structure of a Universe simulated by the *Illustris Collaboration*[1]. The formation of dark matter halos generated steep potential wells, in which baryons fell into the center forming the first baryonic structures. Within these first structures we find stars, and quasars.

Quasars are one of the most intriguing astrophysical objects. They are solar system size primordial galaxies powered by supermassive black holes (SMBHs) in their centers. Obser-

[1]Illustration by http://cosmicweb.kimalbrecht.com/

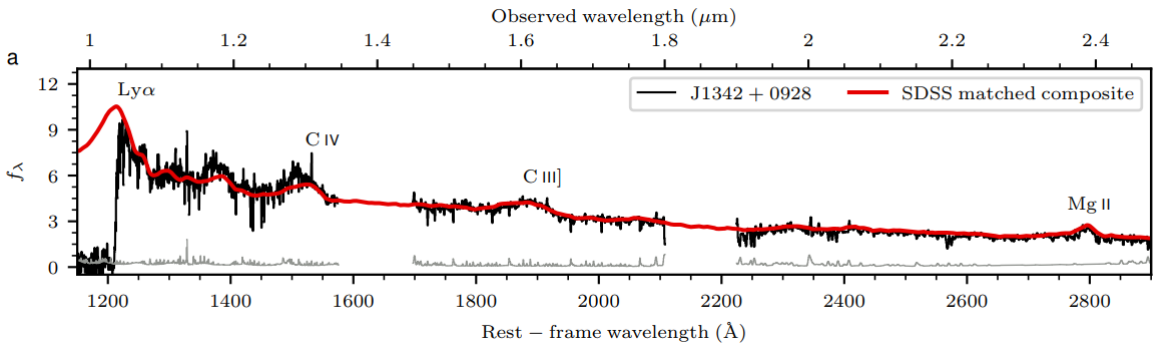

Figure 3: Spectrum of J1342+0928; the highest redshift quasar observed up to date. Image from Bañados et al. (2018).

vations of $z > 6$ quasars (Fan et al., 2006; Mortlock et al., 2011; Wu et al., 2015; Bañados et al., 2018) show that these objects already hosted SMBHs with masses up to 10^9 $M_\odot$ when the universe was ~ 0.7 Gyrs old. The spectrum of the quasar observed at the highest redshift up to date (Bañados et al., 2018) is shown in Figure 3. From this spectrum the following properties are derived: the quasar is localized at $z = 7.527 \pm 0.004$ and the mass of the SMBH in the center is $7.8^{+3.3}_{-1.9} \times 10^8$ $M_\odot$, both properties were calculated in their work using the Mg II line as a tracer.

0.2 Supermassive black hole formation

The formation of SMBHs at early epochs in the Universe is still a puzzle. Various scenarios have been proposed to explain the early assembling of these structures, including primordial stellar remnants, stellar dynamical processes and the direct collapse of protogalactic gas due to dynamic instabilities. Rees (1978) showed one of the first schemes with different pathways that may explain the formation of massive objects. For further reading, see Volonteri (2010); Volonteri & Bellovary (2012); Latif & Ferrara (2016). Figure 4 summarizes several possible pathways to form a supermassive black hole seed considering different physical conditions in the dark matter halo that will host the structure.

Population III of stars

One of the first structures formed in the Universe are thought to be stars, such a population of stars are denominated the Population III (Pop III). Figure 5 represents an artistic impression for this population of stars. These primordial stars formed out of primordial metal-free gas (Abel et al. (2000, 2002); Bromm et al. (1999, 2002); Yoshida et al. (2006)). Recent observations of the 21-cm absorption line due to its interaction with Lyman-α photons reveal that first stars were formed at $z \sim$15 - 20 (Bowman et al., 2018). Pop III are expected to be formed in minihalos of 10^5 - 10^6 $M_\odot$. In these halos molecular hydrogen acts as an efficient coolant, in which star formation takes place. Because these stars are formed out of metal-free

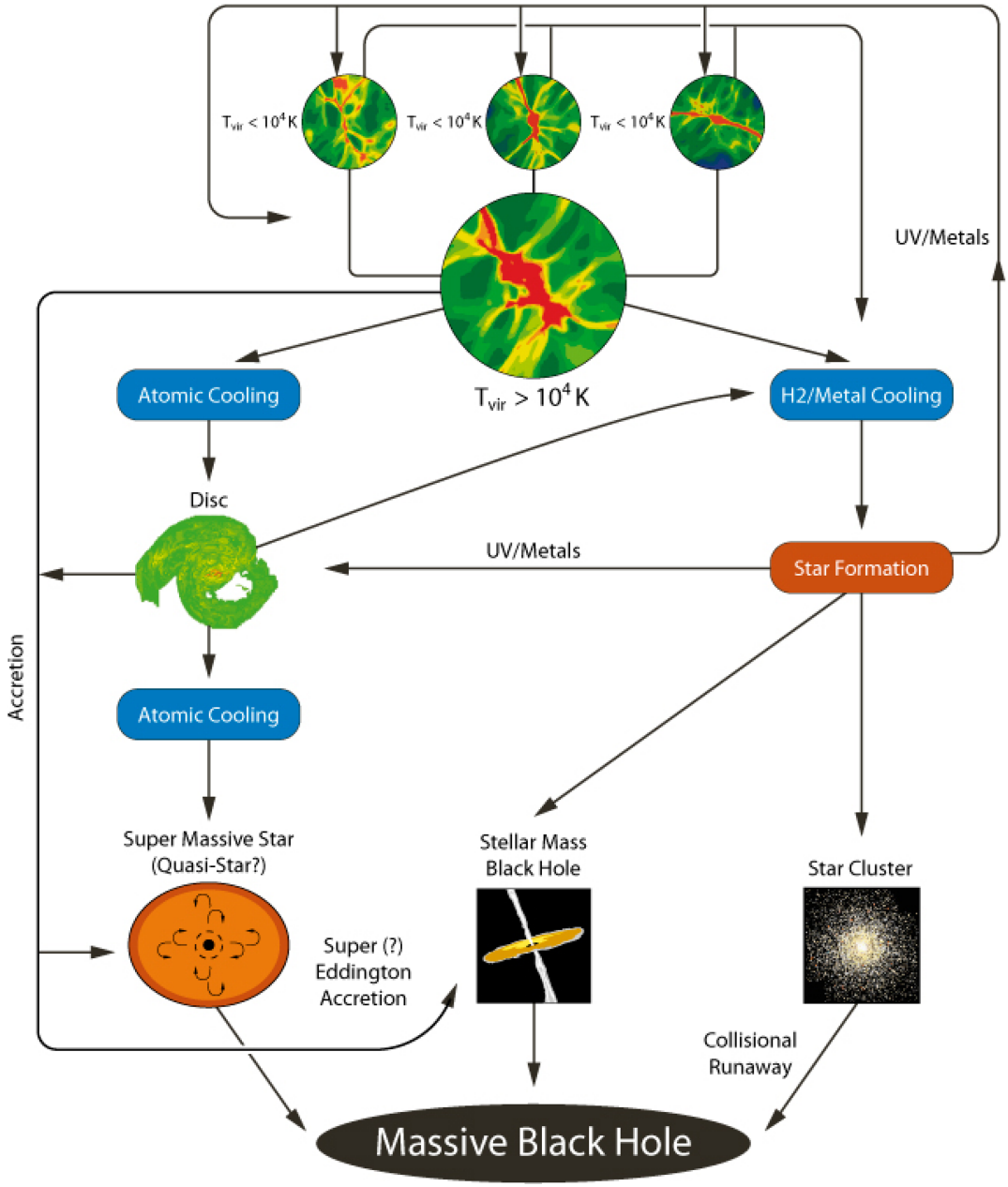

Figure 4: Summary of possible pathways to form a massive black hole according to physical conditions. It shows the formation of different structures that may end up as a massive black hole seed. Image taken from Regan & Haehnelt (2009).

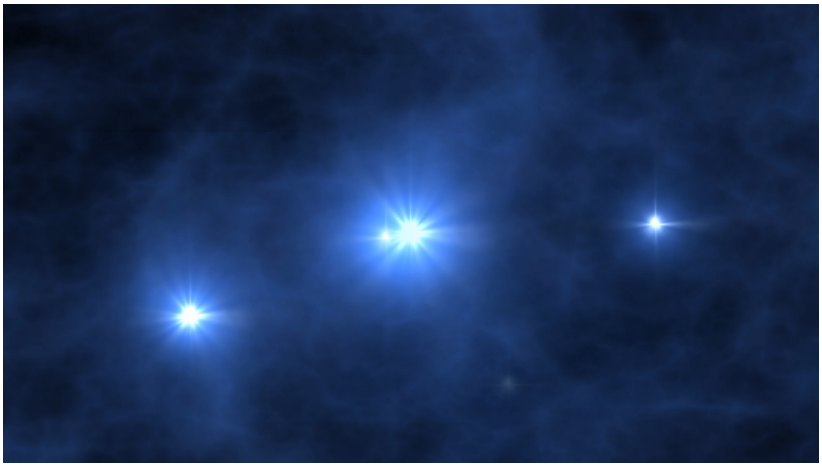

Figure 5: Artistic representation of Pop III stars. Image credit NASA.

gas, they are expected to be more massive than observed local stars. This can be understood from the fact that a primordial Universe is expected to be hotter, implying an increase in the Jeans mass which increases with temperature, allowing the gathering of a larger amount of matter. Three dimensional cosmological simulations show that Pop III stars can reach masses of a few hundred $M_\odot$ (Hirano et al., 2014; Susa et al., 2014). Depending on the star mass, their fate may be different, but most of them end up as stellar black hole remnants (Heger et al., 2003). It is known that radiative feedback effects halt the growing of these structures (Johnson & Bromm, 2007; Alvarez et al., 2009). Stellar black holes would require several super Eddington accretion episodes in order to reach a billion solar masses by redshift $\sim 6-7$ (Volonteri et al., 2015; Pacucci et al., 2015b).

Stellar clusters

The formation of a very massive star (VMS) in dense stellar clusters through runway collisions (Portegies Zwart et al., 1999; Portegies Zwart & McMillan, 2002) has also been proposed to be a candidate for a supermassive black hole seed. If the center of a cluster undergoes core collapse, a single massive compact object may form. In this scenario a fast collapse is key on its feasibility, in order to avoid supernovae feedback from massive stars (Devecchi & Volonteri, 2009; Stone et al., 2017). The formation of binaries is also an obstacle to this scenario, since the heating that may be produced from binaries may delay the core collapse (Heggie, 1975; Hut et al., 1992). Katz et al. (2015) showed that the probability that a star cluster undergoes a runaway collision process is highly dependent on the initial central mass and density of the system. Some recent studies have studied collisions in Population III clusters (Reinoso et al., 2018) and the interaction between collisions and accretion (Boekholt et al., 2018).

Direct collapse black hole

The formation of a massive seed has also been considered in the Direct Collapse Black Hole (DCBH) model. It consists of the immediate collapse of a cloud of gas into a massive seed

of 10^4 - 10^6 $M_\odot$. In this model, the seed would ultimately collapse into a black hole more massive than the ones produced by other models. The seeds would accrete at rates ≥ 0.1 $M_\odot$/yr (Begelman, 2010; Schleicher et al., 2013; Sakurai et al., 2015). However, this scenario demands strict conditions. A very massive halo is indeed necessary to have the gas reservoir to form a massive seed and also to ensure high gas temperature ($\sim$ 8000 K). High temperatures are required to allow the atomic cooling to operate, Figure 6 shows the cooling function as a function of gas temperature for primordial species (Barkana & Loeb, 2001), the solid red line represents the cooling function for atomic species, while the dashed blue line represents the cooling function for molecular species. It can be seen that atomic cooling operates at temperatures $>$ 5000 K.

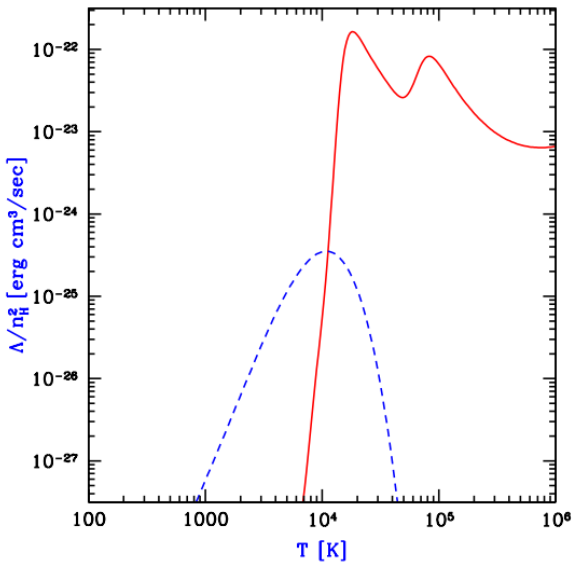

Figure 6: Cooling function as a function of temperature for a primordial chemical environment. The red line represents the cooling function for atomic species, while the blue one pictures the cooling function for molecular species. Image taken from Barkana & Loeb (2001).

In comparison to molecular and metal cooling, atomic cooling is characterized to act more smoothly in the temperature ranges involving a DCBH conditions, permitting an isothermal collapse that does not produce fragments (Latif et al., 2013b, 2014b).

H_2 inhibition is fundamental in the direct collapse model. This molecule can cool the system down to hundreds of Kelvins producing fragments and the formation of minor objects, preventing a single massive body to be assembled. The main mechanism to form molecular hydrogen is shown in Equation 2 which requires the previous formation of H^- that is shown in Equation 3.

$$H + H^- \rightarrow H_2 + e^- \tag{2}$$

$$H + e^- \rightarrow H^- + \gamma \tag{3}$$

One way to prevent the existence of molecular hydrogen is through the direct exposition to photons with energies between 11.2 and 13.6 eV, in the so-called Lyman-Werner (LW) band. The chemical reaction is illustrated in Equation (4), where H_2^* represents an excited state for molecular hydrogen that decays into two hydrogen atoms. Another way to avoid molecular hydrogen formation is preventing the formation of H^-, recognized to catalyze H_2 formation. That can be obtained through the interaction of low energy photons (above 0.76 eV) that photo-detaches the H^- (Equation 5). These two mechanisms are used to impede the major H_2 formation channel in the early Universe.

$$H_2 + \gamma_{LW} \rightarrow H_2^\star \rightarrow H + H \tag{4}$$

$$H^- + \gamma_{0.76} \rightarrow H + e^- \tag{5}$$

The conditions for H_2 inhibition can be fulfilled if there is a star-forming galaxy irradiating the photons mentioned above next to a pristine halo. A galaxy with a spectrum of $T_{\rm eff} = 10^5$ K is more efficient at dissociating H_2 directly (Equation 4) while a $T_{\rm eff} = 10^4$ K is more efficient indirectly (Equation 5).

Molecular hydrogen inhibition is supposed to require a critical value for the UV intensity ($J_{21}^{\rm crit}$) that depends on the spectrum. UV intensities are typically spcecified in units of $J_{21} = 10^{-21}$erg s^{-1}Hz^{-1}cm^{-2}str^{-1}. Latif et al. (2014a) quatified the strength of $J_{21}^{\rm crit}$ by performing 3D cosmological simulations, finding this value to range 400 - 700. Recent estimates for 3D cosmological simulations including realistic Pop II radiation fields and X-rays find that $J_{21}^{\rm crit}$ varies between 20000 - 50000 (Latif et al., 2015). In addition, Glover (2015) argued that the chemical network used in the simulations impact directly in the value of $J_{21}^{\rm crit}$, so he constructed a reduced network of 26 chemical reactions using a reaction-based reduction technique by performing one-zone models. He found $J_{21}^{\rm crit} \sim$18 for $T_{\rm eff} = 10^4$ K and $J_{21}^{\rm crit} \sim$ 1600 for $T_{\rm eff} = 10^5$ K.

Though the DCBH model may explain the formation of massive black hole seeds, there are still some obstacles that gas needs to overcome. One obstacle arises when gas is photo-evaporated, in whose case a dense core is prevented to be formed. Ionization also impedes the formation of a central structure, since it leads to an increase in the electron fraction, which is one of H^- catalysts, which is one of H_2 catalysts (Johnson et al., 2014). Another obstacle corresponds to the tidal interaction that the neighborhood may be exerting against the pristine halo, that could disrupt it, avoiding the formation of a massive central object (Chon et al., 2016).

Other models

Primordial black holes may also be formed in the early universe before the epoch of galaxy formation (Carr, 2003; Khlopov, 2010) in regions where high density fluctuations are large and the whole region can collapse and form a primordial black hole. However, several astrophysical constraints restrict the mass range where primordial black holes are allowed.

Primordial black holes with an initial mass smaller than about 5×10^{14} g are expected to have already evaporated due to Hawking radiation. For larger masses, Ricotti et al. (2008) have constrained the mass upper limit of these black holes up 10^3 $M_\odot$, studying spectral distortions in the cosmic microwave background.

It has also been proposed that dark matter, in the form of Weakly Interacting Massive Particles (WIMPs) may influence the formation of the first stars (Iocco, 2008). If dark matter halos have steep density profiles, during the formation of the first stars the baryonic infall may compress the dark matter further. In whose case, central dark matter densities can be high enough that WIMP annihilation can provide an extra heat source. The energy released by the annihilation of WIMPs in the stellar core overcomes cooling processes and halts stellar collapse ending up as an object called *Dark Star*. Such structure would be supported by dark matter annihilation rather than nuclear fusion (Spolyar et al., 2008; Freese et al., 2008). Dark stars are predicted to be $\sim$500 - 1000 $M_\odot$, with large luminosity (10^6 - 10^7 $L_\odot$), and low surface temperature ($<$ 10000 K). Such massive systems would collapse into BHs, providing alternative seeds. Latif et al. (2018) recently have presented a model in which mirror dark matter: a subdominant dissipative component of dark matter with similar properties to ordinary baryons, may collapse to form massive black holes during the epoch of first galaxies formation.

0.3 Thesis outline

In this thesis, I study the formation of supermassive black hole seeds in different situations by performing cosmological hydrodynamical simulations. I take the DCBH scenario as a reference to mimic and modify. I study the growth of possible SMBH seeds, and the impact of the fragmentation on them and their properties. Simulations have been analyzed using mainly the **yt-code**[2] (Turk et al., 2011).

In Chapter 1, I present a description of the numerical code used to perform the simulations. I also introduce the basic principles of the Adaptive Mesh Refinement technique (AMR) and the numerical solvers implemented in the code. I also discuss several packages, codes, implementations, and modifications included in the code that are necessary to suit the simulations in the best possible way. Finally, I present all modifications I made to the code.

In Chapter 2, I introduce dark-matter only low resolution simulations performed with the only purpose of finding the most promising DCBH candidates, in order to re-simulate them. Some statistics and calculations are presented in this chapter.

In Chapter 3, I show all the results from the re-simulations performed including gas physics. These simulations are performed under the presence of different values for the UV background in order to test its influence. I analyze the dynamics, the profiles, and the growth and accretion in possible seed candidates.

Finally, in Chapter 4 the most important results of this work are shown, also I discuss

[2]http://yt-project.org/

their implications in the actual paradigm and their observability.

Chapter 1

Methodology

For the purpose of this work I use the RAMSES[1] (Teyssier, 2002) code to perform all simulations. Details about the code, packages, tools used, and the modifications I made are specified though this chapter.

1.1 RAMSES

RAMSES is a N-body and hydrodynamical code. It has been developed to study structure formation of the Universe with high spatial resolution. The code is based in the Adaptive Mesh Refinement (AMR) technique with a tree-based data structure allowing recursive grid refinements. The hydrodynamical solver is based on a second-order Godunov method while the N-body solver is based on the solver presented in the ART code (Kravtsov et al., 1997).

1.1.1 Adaptive Mesh Refinement

Adaptive Mesh Refinement (AMR) is a method of adapting the accuracy of a solution within certain sensitive regions of the simulation, dynamically and during the time the solution is being calculated. When solutions are calculated numerically, they are often limited to predetermined quantified grids as in the Cartesian plane which constitute the computational grid. Adaptive mesh refinement provides a dynamic programming environment for adapting the precision of the numerical computation based on the requirements of a numerical problem. It is also a technique used to increase spatial and temporal resolution of numerical simulations beyond the limits imposed by the available resources. The fundamental data structure used in the RAMSES code is called the Fully Threaded Tree (FTT); (Khokhlov, 1998), in which basic elements are not single cells, they are groups of 2^{dim} siblings called *octs*, where dim is the dimension of the simulation (1, 2 or 3). Each oct belongs to a given refinement level labeled "l". A regular Cartesian grid, called the coarse grid, defines the base of the tree

[1] https://www.ics.uzh.ch/ teyssier/ramses/RAMSES.html

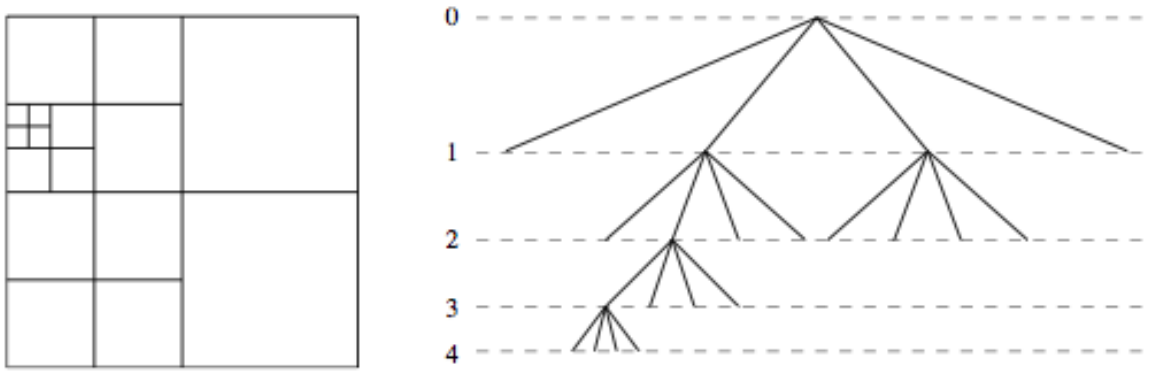

Figure 1.1: Sketch representing a Fully Threaded Tree in a two dimensions. The figure in the left represents the Cartesian grid, while the right represents the tree structure, dashed lines portray the refinement levels.

structure ($l = 0$).

The FTT data structure is illustrated in in Figure 1.1.1. A two-dimensional Cartesian grid in the left, while in the right we observe the tree structure, the numbers assigned to the dashed lines represent the refinement levels, while every group represents an oct.

For a computational cubic volume of side L, cell sizes are related to L by $L/2^{\mathrm{i}}$, where i represents the refinement level. For the integration and refinement algorithms to be effective, the following information must be easily accessible for every cell:

- Level of the cell in the tree
- If the cell is marked to split/unsplit
- Pointer to a parent cell
- Pointer to children
- Pointer to neighbor

All cells in the tree that have children are denominated *split*, while cells with no children are named *leaves*.

Refinement map

The first step into running RAMSES consists of building the refinement map, in which cells are marked for refinement according to a certain refinement criteria defined by the user. In addition, there is an extra strict refinement rule: any oct in the tree must be surrounded by 3^{dim} - 1 neighboring parent cells. By making use of this extra rule a smooth transition is enforced, even in diagonal directions.

For the purpose of this thesis, the Truelove criterion (Truelove et al., 1997) has been used as

the *user-define* criteria. Truelove et al. (1997) realized that 4 cells are required to resolve the Jeans length in order to avoid numerical fragmentation. However, Latif et al. (2013b) studied this criteria using different values of cells per Jeans length in the context of supermassive black seed formation through the Direct Collapse Black Hole scenario. They concluded that 32 cells per Jeans length are the minimum reasonable value to resolve turbulences. Therefore, 32 cells per Jeans length are used in this work as a refinement criteria.

The process of building up the refinement map is summarized in the following points:

- If a split cell contains a children cell that is already marked for refinement, then it is marked for refinement
- Then, the 3^{dim} - 1 neighboring cells are marked for refinement
- If any cell satisfies the used-defined refinement criteria, then it is marked for refinement

The previous steps are performed through each level. From the finer level (l_{max}) down to the coarse level $l = 0$.

Sometimes, the refinement map tends to be noisy. Because of this, an operator can be applied to smooth it. This *smoothing operator* is based in the one used in the ART code. It roughly consists of expanding a cubic buffer around marked cells. The amount of times this cubic buffer is expanded is a free parameter in the code.

Compared to other codes, RAMSES does not require a *de-refinement* criteria set by the user, it automatically *de-refines* cells which are not satisfying the refinement criteria.

Modifying the tree structure

Once the refinement map is done. The next step consists of splitting or destroying children cells. RAMSES performs two passes through each level, starting from the coarse level, up to the finest one:

- If a leaf cell is marked for refinement, then its child oct is created
- If a split cell is not marked for refinement, then its child oct is destroyed

1.1.2 N-body solver

As it was mentioned previously, RAMSES includes particles as elements, they can represent dark matter, stars, or other kind of gravitationally interacting structures. For this work, particles will mostly represent dark matter. A small number will portray not resolved regions (see Section 1.2.3). Regardless of the nature of particles, they will interact with other particles and gas. To integrate the trajectories of the dark matter particles RAMSES uses the following Equations 1.1, 1.2, 1.3:

$$\frac{\mathrm{d}\vec{x}}{\mathrm{d}t} = \vec{v} \tag{1.1}$$

$$\frac{\mathrm{d}\vec{v}}{\mathrm{d}t} = -\nabla\phi \tag{1.2}$$

$$\nabla^2\phi = 4\pi G\rho \tag{1.3}$$

Since the code deals with AMR grids and particles, it is necessary to know how both components interact each other. To achieve this, particles are associated to a given oct. If a particle position fits into the boundaries of an oct, such particle is said to belong to it. Grid-based N-body schemes, usually consists of the following steps:

1. Compute the mass density ρ on the mesh using a *Cloud-in-Cell* (CIC) interpolation scheme.
2. Solve for the potential ϕ on the mesh using the Poisson equation.
3. Compute the acceleration on the mesh using a standard finite-difference approximation of the gradient.
4. Compute each particle acceleration using an inverse CIC interpolation scheme
5. Update each particle velocity according to the acceleration
6. Update each particle position according to its velocity

Density field

The density field is computed using the CIC interpolation scheme (Birdsall & Fuss, 1969; Hockney & Eastwood, 1981). Which basically assigns a density function to a group of particles. In this scheme, density acquires the form shown in Equation 1.4,

$$\rho(x) = \frac{1}{H}\sum_{\mathrm{i}=1}^{N_p} m_{\mathrm{i}} W(x_{\mathrm{i}} - x) \tag{1.4}$$

where W is an interpolation function, m_{i} is the mass of the particles, x_{i} is its position, N_p is the number of particles in the region of interpolation and H is a quantity associated with the extent of the region from which the density is being interpolated. For each level, particles sitting inside level l boundaries are first considered. Particles outside the current level, but whose clouds intersect the corresponding volume are taken into account in the computation of the density field.

Poisson equation

Once the density field has been calculated, to solve the Poisson equation is the next step (Equation 1.3). This equation is solved using a *one-way interface* scheme (Jessop et al.,

1994; Kravtsov et al., 1997) in the coarse level ($l = 0$). This scheme makes use of the fact that the integration in the coarse level does not depend on the finer grids. The Poisson equation is solved by performing a standard Fast Fourier Transform (FFT) since the coarse level consists of a cubic regular grid of fixed resolution. FFT supports periodic boundary conditions. In Equation 1.5, the Fourier transform of the Poisson equation is recalled,

$$-k^2\tilde{\phi}(\vec{k}) = \tilde{\rho}(\vec{k}) \tag{1.5}$$

where $\sim$ stand for Fourier transform of a function, ϕ is the gravitational field, ρ is the density, $\vec{k}$ is the wavelength vector, while k is its magnitude. The Green function corresponds to the Fourier transform of the Laplacian using a seven points (just in 3D simulations) finite difference approximation.

For finer levels ($l > 0$), a relaxation scheme is used instead. The Poisson equation is solved using a seven points (just in 3D simulations) finite difference approximation in the Laplacian, with Dirichlet boundary conditions. In RAMSES, boundary conditions are defined in a temporary buffer region surrounding the level domain, where the potential is reconstructed from level $l - 1$ through linear reconstruction.

Once the boundary conditions are specified, the potential is obtained using a relaxation method. In RAMSES, the Gauss-Seidel (GS) method with the Red-Black Ordering and Succesive Over Relaxation is used (Press et al., 1992). Equation 1.6 shows the discretization used to solve the potential in RAMSES for a two-dimensional grid.

$$\phi_{\mathrm{i},j}^{n+1} = \frac{1}{4}(\phi_{\mathrm{i}+1,j}^{n} + \phi_{\mathrm{i}-1,j}^{n} + \phi_{\mathrm{i},j+1}^{n} + \phi_{\mathrm{i},j-1}^{n}) - \frac{1}{4}\rho_{\mathrm{i},j} \tag{1.6}$$

This iteration is applied first to all cells defined by i and j odd, or i and j even, and then updated to cells defined by i odd and j even or i even and j odd. Once these calculations are made, the result is over-corrected using the relaxation parameter ω as it is shown in Equation 1.7.

$$\phi_{\mathrm{i},j}^{n+1} = \omega\phi_{\mathrm{i},j}^{n} + (1-\omega)\phi_{\mathrm{i},j}^{n+1} \qquad\qquad 1 < \omega < 2 \tag{1.7}$$

For a regular $N \times N$ Cartesian mesh, the optimal ω parameter is given by Equation 1.8, where α is a parameter defined by the boundary conditions, $\alpha = 1$ when Dirichlet boundary conditions are set, while $\alpha = 2$ is for periodic boundary conditions. See Press et al. (1992).

$$\omega \simeq \frac{2}{1 - \alpha\frac{\pi}{N}} \tag{1.8}$$

Acceleration

Acceleration is calculated on the mesh using a five-points finite difference approximation of potential's gradient. The gradient is symmetrical in order to avoid self-forces. Buffer regions are corrected to give correct boundary conditions. Acceleration is interpolated back to the particles of the current level using an inverse CIC scheme, since the Poisson Equation is solved for the density on the mesh.

1.1.3 Hydrodynamical solver

In RAMSES, the Euler equations are solved in their conservative form:

$$\frac{\partial \rho}{\partial t} + \vec{\nabla} \cdot (\rho \vec{v}) = 0 \tag{1.9}$$

$$\frac{\partial}{\partial t}(\rho \vec{v}) + \vec{\nabla} \cdot (\rho \vec{v} \otimes \vec{v}) + \vec{\nabla} p = -\rho \vec{\nabla} \phi \tag{1.10}$$

$$\frac{\partial}{\partial}(\rho \mathrm{e}) + \vec{\nabla} \cdot [\rho \vec{v}(\mathrm{e} + p/\rho)] = -\rho \vec{v} \cdot \vec{\nabla} \phi \tag{1.11}$$

$$p = (\gamma - 1)\rho \left(\mathrm{e} - \frac{1}{2} v^2 \right) \tag{1.12}$$

where ρ is density, $\vec{v}$ is the fluid velocity vector, e is the specific total energy, and p is the thermal pressure.

Equation 1.14 represents the numerical discretization of the Euler equations, gravity is included in the system as a source term in this equation. Cell-averaged quantities of density, velocities and internal energy are summarized in the U_{i}^n variable (Equation 1.13)

$$U_{\mathrm{i}}^n = (\rho, \rho \vec{v}, \rho \mathrm{e}) = (\rho, \rho \vec{v}_x, \rho \vec{v}_y, \rho \vec{v}_z, \rho \mathrm{e}) \tag{1.13}$$

In the previous and the following equations, n stands for the time integration in the simulation (t_n), while i represents the cell.

$$\frac{U_{\mathrm{i}}^{n+1} - U_{\mathrm{i}}^n}{\Delta t} + \frac{F_{\mathrm{i}+1/2}^{n+1/2} - F_{\mathrm{i}-1/2}^{n+1/2}}{\Delta x} = S_{\mathrm{i}}^{n+1/2} \tag{1.14}$$

Time centered fluxes $F_{\mathrm{i}+1/2}^{n+1/2}$ across all interfaces are calculated using a second-order Godunov method, also known as Piecewise Linear Method. Gravitational source terms are included using a time centered fractional step approach (Equation 1.15).

$$S_{\mathrm{i}}^{n+1/2} = \left(0, \frac{\rho_{\mathrm{i}}^{n}\nabla\phi_{\mathrm{i}}^{n} + \rho_{\mathrm{i}}^{n+1}\nabla\phi_{\mathrm{i}}^{n+1}}{2}, \frac{(\rho\vec{v})_{\mathrm{i}}^{n}\cdot\nabla\phi_{\mathrm{i}}^{n} + (\rho\vec{v})_{\mathrm{i}}^{n+1}\cdot\nabla\phi_{\mathrm{i}}^{n+1}}{2}\right) \tag{1.15}$$

The implementation of both methods is based on the work of Colella (1990) and Saltzman (1994).

1.1.4 Cosmological settings

RAMSES allows to solve fluid dynamics or N-body problems in a cosmological context, which is the one used for the purpose of this thesis. In such a case, all variables are re-scaled according to the parameters set by the user, this re-scaling was defined by Martel & Shapiro (1998). Time, position, density, pressure, velocity and the Poisson equation are re-scaled according to Equations 1.16, 1.17, 1.18, 1.19, 1.20, and 1.21.

$$\mathrm{d}\tilde{t} = H_0\frac{\mathrm{d}t}{a^2} \tag{1.16}$$

$$\tilde{x} = \frac{1}{a}\frac{x}{L} \tag{1.17}$$

$$\tilde{\rho} = a^3\frac{\rho}{\Omega_m\rho_c} \tag{1.18}$$

$$\tilde{P} = a^5\frac{P}{\Omega_m\rho_c H_0^2 L^2} \tag{1.19}$$

$$\tilde{\vec{v}} = a\frac{\vec{v}}{H_0 L} \tag{1.20}$$

$$\nabla^2\tilde{\phi} = \frac{3}{2}a\Omega_m(\tilde{\rho} - 1) \tag{1.21}$$

This procedure defines the code's units, i.e. the units the code work with. In the above equations H_0 corresponds to the Hubble constant, Ω_m is the matter density, L is the box size, and ρ_c is the critical density of the Universe. The scale factor is represented by a.

An interesting consequence of the change of variables defined above is that Equations 1.1, 1.9, 1.10, and 1.11 remain unchanged.

1.2 Complementary tools

Typically, simulations require the use of extra tools to suit them as best as possible, due to this, I made use of several packages, codes, and implementations.

Chemistry plays a key role in many astrophysical situations regulating the thermal properties of the gas, which are relevant for instance during gravitational collapse, the evolution of disks and fragmentation processes. Because of this, the KROME[2] (Grassi et al., 2014) package was included. In Section 1.2.1, this package is presented more deeply.

All simulations precise of initial conditions to start with. Initial conditions in this work has been performed with the MUSIC[3] code (Hahn & Abel, 2011), since it allows to optimize the computational resources by focusing in a specific region. See Section 1.2.2

The gravitational collapse of dense regions is a phenomenon quite recurrent in astrophysical simulations. Recalling the limitation of resources, some numerical artifacts have arisen to deal with the small scales. In Section 1.2.3 the *by default* implementation to deal with with the smallest not-resolved regions is presented.

1.2.1 KROME

The KROME (Grassi et al., 2014) package solves the thermal and chemical evolution of the gas. The evolution of a set of initial chemical species that react and form new species via a given set of reactions is described by a system of ordinary differential equations (Equation 1.22),

$$\frac{\mathrm{d}n_\mathrm{i}}{\mathrm{d}t} = \sum_{j \in F_\mathrm{i}} \left(k_j \prod_{r \in R_j} n_{r(j)} \right) - \sum_{j \in D_\mathrm{i}} \left(k_j \prod_{r \in R_j} n_{r(j)} \right) \tag{1.22}$$

where n_i stands for the number density of a determined species i. The first sum represents the contribution to the number rate by the reactions that form that i specie (which belong to the set F_i), while the second part is the analogous, but for the reactions that destroy that i specie (set D_i). Every j reaction (regardless of if it is for formation or destruction) has a set of reactants (R_j), and the number density of each reactants at time t of the reaction j is $n_{r(j)}$, while the corresponding reaction rate coefficient is k_j, which can be a function of any parameter.

The following primordial species has been added for the purpose of this work: H, H^+, H^-, He, He^+, He^{++}, e^-, H_2, H_2^+, their initial abundances are shown in Table 1.1, which have been calculated in various works, for instance see Galli & Palla (1998). The package includes the photo-detachment of H^-, the photo-dissociation of H_2 and H_2^+, collisional dissociation, collisional induced emission, chemical cooling/heating from three body reactions, cooling by collisional excitation, collisional ionization, radiative recombination and bremsstrahlung

[2] http://www.kromepackage.org/
[3] https://www-n.oca.eu/ohahn/MUSIC/

radiation. The package also allows the H_2 self-shielding fitting function (Equation 1.23) by Wolcott-Green et al. (2011).

Table 1.1: Initial abundances for all chemical species included in the simulation. These values are based on abundance estimates from the nucleosynthesis. See Galli & Palla (1998). All species are required to have non-zero values to ensure numerical convergence.

Chemical species	Initial abundance
H	0.75615
e^-	4.4983×10^{-8}
H^+	8.1967×10^{-5}
He	0.24375
He^+	10^{-40}
He^{++}	10^{-40}
H^-	10^{-40}
H_2	1.5123×10^{-6}
H_2^+	10^{-40}

Chemical Reactions

All the chemical reactions used and their respective rate coefficients are listed in Table 1.2. References are shown too. In rate coefficients T is gas temperature in K, T_e is gas temperature in eV, T_{rad} is radiation temperature in K, J_{21} is the UV intensity in units of J_{21} (10^{-21} erg s^{-1} Hz^{-1} cm^{-2} str^{-1}), and n_H is number density for neutral hydrogen in n/cm^3.

Molecular hydrogen is known to be dissociated under the presence of a UV background, however, if there are high concentrations of this molecule, the radiation will just destroy some of them. This effect in quantified by the self-shielding function $f_{sh}(n,T)$, which naturally depends on temperature and density (Equation 1.23). The self-shielding function contains elements from Equations 1.24 and 1.25, in these latter equations H_{mass} stands for neutral hydrogen mass, k is the Boltzmann constant, xN_{H_2} is a normalized H_2 density column where n_{H_2} is H_2 number density.

$$f_{sh}(n,T) = \frac{0.965}{(1+xN_{H_2}/b)^{1.1}} + \frac{0.035}{(1+xN_{H_2})^{0.5}} \cdot \exp[-8.5\times10^{-4}(1+xN_{H2})^{0.5}] \tag{1.23}$$

$$b = \left(\frac{kT}{H_{mass}}\right)^{0.5} 10^{-5} \tag{1.24}$$

$$xN_{H_2} = 7.48\times10^6 \cdot (n_{H_2}\cdot 10^{-3})^{2/3} \tag{1.25}$$

Chemical reactions (1)-(28) are found in the *react_xrays* network included in the KROME package. This network includes the most predominant reactions in a primordial environment,

also existing literature about the rates to create/destroy them. In addition, Glover (2015) argued that the primordial chemical network impacts directly in the value of J_{21}^{crit}, he also found two relevant reactions to be missing in the KROME package networks. The two missing reactions are included in this work, which are reactions (29) and (30).

Table 1.2: Chemical reactions with their respective rate coefficient and references. Rate coefficients are in units of $cm^{3(n-1)}s^{-1}$ were n is the number of reactants.

Reaction	**Rate coefficient ($cm^{3(n-1)}s^{-1}$)**		**Ref.**
(1) $H + e^-$	$k_1 = \exp[-32.71396786$		1
$\rightarrow H^+ + 2e^-$	$+13.5365560 \ln T_e$		
	$-5.73932875 (\ln T_e)^2$		
	$+1.56315498 (\ln T_e)^3$		
	$-0.28770560 (\ln T_e)^4$		
	$+3.48255977 \times 10^{-2} (\ln T_e)^5$		
	$-2.63197617 \times 10^{-3} (\ln T_e)^6$		
	$+1.11954395 \times 10^{-4} (\ln T_e)^7$		
	$-2.03914985 \times 10^{-6} (\ln T_e)^8]$		
(2) $H^+ + e^-$	$k_2 = 3.92 \times 10^{-13} T_e^{-0.6353}$	$T \leq 5000$ K	2
$\rightarrow H + \gamma$	$k_2 = \exp[-28.61303380689232$	$T > 5500$ K	
	$-7.241125657826851 \times 10^{-1} \ln T_e$		
	$-2.026044731984691 \times 10^{-2} (\ln T_e)^2$		
	$-2.380861877349834 \times 10^{-3} (\ln T_e)^3$		
	$-3.212605213188796 \times 10^{-4} (\ln T_e)^4$		
	$-1.421502914054107 \times 10^{-5} (\ln T_e)^5$		
	$+4.989108920299513 \times 10^{-6} (\ln T_e)^6$		
	$+5.755614137575758 \times 10^{-7} (\ln T_e)^7$		
	$-1.856767039775261 \times 10^{-8} (\ln T_e)^8$		
	$-3.071135243196595 \times 10^{-9} (\ln T_e)^9]$		
(3) $He + e^-$	$k_3 = \exp[-44.09864886$		1
$\rightarrow He^+ + 2e^-$	$+23.91596563 \ln T_e$		
	$-10.7532302 (\ln T_e)^2$		
	$+3.05803875 (\ln T_e)^3$		
	$-0.56851189 (\ln T_e)^4$		
	$+6.79539123 \times 10^{-2} (\ln T_e)^5$		
	$-5.00905610 \times 10^{-3} (\ln T_e)^6$		
	$+2.06723616 \times 10^{-4} (\ln T_e)^7$		
	$-3.64916141 \times 10^{-6} (\ln T_e)^8]$		
(4) $He^+ + e^-$	$k_4 = 3.92 \times 10^{-13} T_e^{-0.6353}$	$T \leq 9280$ K	3
$\rightarrow He + \gamma$	$k_4 = 3.92 \times 10^{-13} T_e^{-0.6353}$	$T > 9280$ K	
	$+ 1.54 \times 10^{-9} T_e^{-1.5}$		
	$\times([1 + 0.3/\exp(8.099328789667/T_e)]$		
	$/[\exp(40.49664394833662/T_e)])$		

1: Janev et al. (1987), 2: Abel et al. (1997) fit by data from Ferland et al. (1992)
3: Cen (1992); Aldrovandi & Pequignot (1973)

Reaction	Rate coefficient		Ref.
(5) $He^+ + e^-$	$k_5 = \exp[-68.71040990212001$		4
$\rightarrow He^{++} + 2e^-$	$+43.93347632635 \ln T_e$		
	$-18.48066993568 (\ln T_e)^2$		
	$+4.701626486759002 (\ln T_e)^3$		
	$-7.692466334492 \times 10^{-1} (\ln T_e)^4$		
	$+8.113042097303 \times 10^{-2} (\ln T_e)^5$		
	$-5.324020628287001 \times 10^{-3} (\ln T_e)^6$		
	$+1.975705312221 \times 10^{-4} (\ln T_e)^7$		
	$-3.165581065665 \times 10^{-6} (\ln T_e)^8)]$		
(6) $He^{++} + e^-$	$k_6 = 1.891 \times 10^{-10}/(a\sqrt{T/9.37})$		5
$\rightarrow He^+ + \gamma$	$a = (1.0 + \sqrt{T/9.37})^{0.2476}(1.0 + \sqrt{T/2.774 \times 10^6})^{1.7524}$		
(7) $H + e^-$	$k_7 = 1.4 \times 10^{-18} \, T^{0.928} \exp(-T/16200)$		6
$\rightarrow H^- + \gamma$			
(8) $H^- + H$	$k_8 = a_1(T^{a_2} + a_3 T^{a_4} + a_5 T^{a_6})$		7
$\rightarrow H_2 + e^-$	$/(1.0 + a_7 T^{a_8} + a_9 T^{a_{10}} + a_{11} T^{a_{12}})$		
	$a_1 = 1.3500 \times 10^{-9}$		
	$a_2 = 9.8493 \times 10^{-2}$		
	$a_3 = 3.2852 \times 10^{-1}$		
	$a_4 = 5.5610 \times 10^{-1}$		
	$a_5 = 2.7710 \times 10^{-7}$		
	$a_6 = 2.1826$		
	$a_7 = 6.1910 \times 10^{-3}$		
	$a_8 = 1.0461$		
	$a_9 = 8.9712 \times 10^{-11}$		
	$a_{10} = 3.0424$		
	$a_{11} = 3.2576 \times 10^{-14}$		
	$a_{12} = 3.7741$		
(9) $H + H^+$	$k_9 = 2.10 \times 10^{-20} \, (T/30)^{-0.15}$	$T < 30$ K	8
$\rightarrow H_2^+ + \gamma$	$k_9 = \mathrm{dex}[-18.20 - 3.194 \log_{10} T$	$T > 30$ K	
	$+1.786(\log_{10} T)^2 - 0.2072(\log_{10} T)^3]$		
(10) $H_2^+ + H$	$k_{10} = 6.0 \times 10^{-10}$		9
$\rightarrow H_2 + H^+$			

4: Aladdin database, see Abel et al. (1997), 5: Verner & Ferland (1996)
6: de Jong (1972), 7: Kreckel et al. (2010)
8: Coppola et al. (2011), 9: Karpas et al. (1979)

Reaction	Rate coefficient		Ref.
(11) $H_2 + H^+$	$k_{11} = \exp(-a/T)$	100 K $\leq T \leq$ 30000 K	10
$\rightarrow H_2^+ + H$	$\times[b_1 + b_2 \ln T + b_3(\ln T)^2$		
	$+b_4(\ln T)^3 + b_5(\ln T)^4 + b_6(\ln T)^5$		
	$+b_7(\ln T)^6 + b_8(\ln T)^7]$		
	$a = 2.1237150 \times 10^4$		
	$b_1 = -3.3232183 \times 10^{-7}$		
	$b_2 = 3.3735382 \times 10^{-7}$		
	$b_3 = -1.4491368 \times 10^{-7}$		
	$b_4 = 3.4172805 \times 10^{-8}$		
	$b_5 = -4.7813728 \times 10^{-9}$		
	$b_6 = 3.9731542 \times 10^{-10}$		
	$b_7 = -1.8171411 \times 10^{-11}$		
	$b_8 = 3.5311932 \times 10^{-13}$		
(12) $H_2 + e^-$	$k_{12} = 35.5\ T^{-2.28} \exp(-46707/T)$		11
$\rightarrow H + H^-$			
(13) $H_2 + e^-$	$k_{13} = 4.38 \times 10^{-10}\ T^{0.35} \exp(-102000/T)$		12
$\rightarrow H + H + e^-$			
(14) $H_2 + H$	k_{14}, see ref.		13
$\rightarrow H + H + H$			
(15) $H^- + e^-$	$k_{15} = \exp[-18.01849334273$		1
$\rightarrow H + 2e^-$	$+2.360852208681 \ln T_e$		
	$-2.827443061704 \times 10^{-1} (\ln T_e)^2$		
	$+1.623316639567 \times 10^{-2} (\ln T_e)^3$		
	$-3.365012031362999 \times 10^{-2} (\ln T_e)^4$		
	$+1.178329782711 \times 10^{-2} (\ln T_e)^5$		
	$-1.656194699504 \times 10^{-3} (\ln T_e)^6$		
	$+1.068275202678 \times 10^{-4} (\ln T_e)^7$		
	$-2.63128580920710 \times 10^{-6} (\ln T_e)^8]$		
(16) $H^- + H$	$k_{16} = 2.5610 \times 10^{-9}\ T_e^{1.781860}$	$T \leq 1160$ K	14
$\rightarrow H + H + e^-$	$k_{16} = \exp[-20.37260896533324$	$T > 1160$ K	
	$+1.139449335841631 \ln T_e$		
	$-1.421013521554148 \times 10^{-1} (\ln T_e)^2$		
	$+8.46445538663 \times 10^{-3} (\ln T_e)^3$		
	$-1.4327641212992 \times 10^{-3} (\ln T_e)^4$		
	$+2.012250284791 \times 10^{-4} (\ln T_e)^5$		
	$+8.66396324309 \times 10^{-5} (\ln T_e)^6$		
	$-2.585009680264 \times 10^{-5} (\ln T_e)^7$		
	$+2.4555011970392 \times 10^{-6} (\ln T_e)^8$		
	$-8.06838246118 \times 10^{-8} (\ln T_e)9$		

10: Savin et al. (2004), 11: Capitelli et al. (2007)
12: Mitchell & Deveau (1983), fit of data by Corrigan (1965)
13: Martin et al. (1996), 14: Abel et al. (1997) based on Janev et al. (1987)

Reaction	Rate coefficient		Ref.
(17) $H^- + H^+$	$k_{17} = 2.96 \times 10^{-6}/\sqrt{T}$	$10\ \mathrm{K} < T < 10^5\ \mathrm{K}$	15
$\rightarrow H + H$	-1.73×10^{-9}		
	$+2.5 \times 10^{-10}\sqrt{T}$		
	$-7.77 \times 10^{-13}T$		
(18) $H^- + H^+$	$k_{18} = 10^{-8}\ T^{-0.4}$		16
$\rightarrow H_2^+ + e^-$			
(19) $H^- + \gamma$	$k_{19} = J_{21} \times 10^{[(a+bT_{\rm rad})^{-1/c} - {\rm d}]}$		17
$\rightarrow H + e^-$	$a = 9.08944 \times 10^{-2}$		
	$b = 3.27940 \times 10^{-5}$		
	$c = 5.98490 \times 10^{-1}$		
	${\rm d} = 10.9867$		
(20) $H_2 + \gamma$	$k_{20} = f_{sh}(n,T) \times J_{21} \times 10^{[1.0/(a+bT_{\rm rad}+cT_{\rm rad}^2) - {\rm d}]}$		18
$\rightarrow H + H$	$a = 1.17350 \times 10^{-1}$		
	$b = 2.49580 \times 10^{-4}$		
	$c = 3.48559 \times 10^{-9}$		
	${\rm d} = 11.902$		
(21) $H_2^+ + \gamma$	$k_{21} = J_{21} \times [(a + bT_{\rm rad})^{-1/c} + {\rm d}]$		18
$\rightarrow H^+ + H$	$a = -3.83012 \times 10^6$		
	$b = 5.06447 \times 10^2$		
	$c = 6.20988 \times 10^{-1}$		
	${\rm d} = 3.68778 \times 10^{-12}$		
(22) $H_2^+ + e^-$	$k_{22} = 10^6[4.2278 \times 10^{-14}$	$T \leq 10000\ \mathrm{K}$	19
$\rightarrow H + H + \gamma$	$-2.3088 \times 10^{-17}T$		
	$+7.3428 \times 10^{-21}T^2$		
	$-7.5474 \times 10^{-25}T^3$		
	$+3.3468 \times 10^{-29}T^4$		
	$-5.528 \times 10^{-34}T^5]$		
(23) $H_2^+ + H^-$	$k_{23} = 5 \times 10^{-7}\ \sqrt{100/T}$		20
$\rightarrow H + H_2$			
(24) $H + H + H$	$k_{24} = 6 \times 10^{-32}T^{-0.25} + 2 \times 10^{-31}\ T^{-0.5}$		21
$\rightarrow H_2 + H$			
(25) $H_2 + H + H$	$k_{25} = k_{24}/8$		22
$\rightarrow H_2 + H_2$			
(26) $H_2 + H_2$	$k_{26} = kh_{26}^{(1.0-a_{26})} \times kl_{26}^{a_{26}}$		23
$\rightarrow H + H + H_2$	$kl_{26} = 1.18 \times 10^{-10} \exp(-6.95 \times 10^4/T)$		
	$kh_{26} = 8.125 \times 10^{-8}\ T^{-0.5}$		
	$\times \exp(-5.2 \times 10^4/T)\ (1.0 - \exp(-6 \times 10^3/T))$		
	$ncr_{26} = {\rm dex}[4.845 - 1.3\log(T/10^4) + 1.62[\log(T/10^4)]^2]$		
	$a_{26} = 1/(1 + ({\rm nH}/ncr_{26}))$		
(27) $He^+ + H$	$k_{27} = 1.2 \times 10^{-15}\ (T/300)^{0.25}$		24
$\rightarrow He + H^+$			

15: Stenrup et al. (2009), 16: Poulaert et al. (1978)
17: Latif et al. (2015), see also Miyake et al. (2010), 18: Latif et al. (2015)
19: Coppola et al. (2011), 20: Dalgarno & Lepp (1987), 21: Forrey (2013)
22: Adopted from Forrey (2013), 23: Omukai (2001), 24: Yoshida et al. (2006)

Reaction	Rate coefficient		Ref.
(28) He + H^+	$k_{28} = 1.26 \times 10^{-9}\ T^{-0.75}$	$T \leq 10^4$ K	24
$\rightarrow He^+ + H$	$\times \exp(-1.275 \times 10^5/T)$		
	$k_{28} = 4 \times 10^{-37} T^{4.74}$	$T > 10^4$ K	
(29) H + H	$k_{29} = 1.2 \times 10^{-17}\ T^{1.2} \exp(-1.578 \times 10^5/T)$		25
$\rightarrow H^+ + e^- + H$			
(30) H + He	$k_{30} = 1.75 \times 10^{-17} T^{1.3} \exp(-1.578 \times 10^5/T)$		25
$\rightarrow H^+ + e^- + He$			

25: Glover (2015)

Deuterium and molecules containing this element are expected to be outcomes of the nucleosynthesis, however, their abundances are so low that cooling from these species is irrelevant compared to molecular hydrogen cooling. They are potentially important in environments with sufficient electron fraction to catalize the HD formation (Shchekinov & Vasiliev, 2006). The simulations performed in this work do not include these chemical species, for the reason mentioned above and to save computational memory. One simulation was performed including a deuteride chemistry to test its relevance, and as a check the dissociation assumption. The following species were added: D, D^-, HD, D^+, HD^+. The chemical reactions and their coefficient rates are shown in Table 1.3. The initial abundance for all the species correspond to the same in Table 1.1 adding deuteride species with an initial abundance of 10^{-40} for all.

Table 1.3: Chemical reactions for deuteride species with their respective rate coefficient and references. Rate coefficients are in units of $cm^{3(n-1)}s^{-1}$ were n is the number of reactants.

Reaction	Rate coefficient ($cm^{3(n-1)}s^{-1}$)		Ref.
(31) H^+ + D	$k_{31} = 2.00 \times 10^{-10} T^{0.402} \exp(-37.1/T)$	T $\geq$ 50 K	26
$\rightarrow$ H + D^+	$-3.31 \times 10^{-17} T^{1.48}$		
(32) H + D^+	$k_{32} = 2.06 \times 10^{-10} T^{0.396} \exp(-33/T)$	T $\geq$ 50 K	26
$\rightarrow$ H^+ + D	$+2.03 \times 10^{-9} T^{-0.332}$		
(33) H_2 + D^+	$k_{33} = 10^{-9}[0.417 + 0.846 \log_{10}(T)$		27
$\rightarrow$ HD + H^+	$-0.137(\log_{10}(T))^2]$		
(34) HD + H^+	$k_{34} = \exp(-457/T) \times 10^{-9}$		28
$\rightarrow$ H_2 + D^+			
(35) H_2 + D	$k_{35} = \mathrm{dex}[-56.4737 + 5.88886 \log_{10} T$	T $\leq$ 2000 K	29
$\rightarrow$ HD + H	$+7.19692(\log_{10} T)^2 + 2.25069(\log_{10} T)^3$		
	$-2.16903(\log_{10} T)^4 + 0.317887(\log_{10} T)^5]$		
	$k_{35} = 3.17 \times 10^{-10} \exp(-5207/T)$	T > 2000 K	
(36) HD + H	$k_{36} = 5.25 \times 10^{-11}$	T > 200 K	30
$\rightarrow$ H_2 + D	$\exp(-4430/T + 1.739 \times 10^5/T^2)$		

26: Galli & Palla (2002) from Savin (2001), 27: Galli & Palla (2002) from Gerlich (1982)
28: Galli & Palla (2002) from Gerlich (1982) with modification by Gay et al. (2011)
29: Glover & Savin (2009) from data by Mielke et al. (2003)
30: Galli & Palla (2002), from Shavitt (1959)

Reaction	Rate coefficient	Ref.
(37) $D + H^- \rightarrow HD + e^-$	$k_{37} = 1.5 \times 10^{-9}(T/300)^{-0.1}$	31
(38) $D^+ + e^- \rightarrow D$	$k_{38} = 3.6 \times 10^{-12}(T/300)^{-0.75}$	31
(39) $H + D \rightarrow HD$	$k_{39} = 10^{-25}$	31
(40) $HD^+ + H \rightarrow HD + H^+$	$k_{40} = 6.4 \times 10^{-10}$	31
(41) $H^+ + D \rightarrow HD^+$	$k_{41} = \mathrm{dex}[-19.38 - 1.523\log_{10}T + 1.118(\log_{10}T)^2 - 0.1269(\log_{10}T)^3]$	31
(42) $HD^+ + e^- \rightarrow H + D$	$k_{42} = 7.2 \times 10^{-8}/\sqrt{T}$	31
(43) $D + e^- \rightarrow D^-$	$k_{43} = 3 \times 10^{-16}(T/300)^{0.95}\exp(-T/9320)$	31
(44) $D^+ + D^- \rightarrow D + D$	$k_{44} = 5.7 \times 10^{-8}(T/300)^{-0.5}$	31
(45) $D^- + H^+ \rightarrow D + H$	$k_{45} = 4.6 \times 10^{-8}(T/300)^{-0.5}$	31
(46) $H^- + D \rightarrow D^- + H$	$k_{46} = 6.4 \times 10^{-9}(T/300)^{0.41}$	31
(47) $H^- + D \rightarrow D^- + H$	$k_{47} = 6.4 \times 10^{-9}(T/300)^{0.41}$	31
(48) $D^- + H \rightarrow HD + e^-$	$k_{48} = 1.5 \times 10^{-9}(T/300)^{-0.1}$	31

31: Galli & Palla (1998)

1.2.2 MUSIC

MUlti-Scale Initial Conditions for cosmological simulations (MUSIC) (Hahn & Abel, 2011) is a software used to generate nested grid initial conditions for high-resolution "zoomed" cosmological simulations. It generates Gaussian random fields that follow a prescribed power spectrum and act as source terms for the initial density, and initial velocity perturbations. This code performs a smoother transition for the initial velocities between different levels in the zoomed-in region.

The physical parameters set to generate the initial conditions in the simulations presented in this work are displayed in Table 1.4. Cosmological parameters were chosen according to the cosmology given by the Planck Collaboration et al. (2016). The box length was set to be 1 cMpc/h in order to sample cosmological scales. The initial redshift of 99 is a standard number to let the initial perturbations grow properly, these values were also chosen to optimize the available computational resources.

Table 1.4: Box length, initial redshift, $\Omega_{\rm m}$, $\Omega_{\rm baryons}$, Ω_Λ, H_0, σ_8, $n_{\rm spec}$ parameters and their values set in the code to perform initial conditions.

Parameter	Value
Box length	1 [cMpc/h]
Initial redshift	99
$\Omega_{\rm m}$	0.3089
$\Omega_{\rm baryons}$	0.0486
Ω_Λ	0.6911
H_0	67.74 [km/s/Mpc]
σ_8	0.8159
$n_{\rm spec}$	0.9667

1.2.3 Sink Particles

Unlike previous sections, sink particles are an implementation in the code rather than a package or an analysis tool. Here I will review some key concepts.

The gravitational collapse of dense regions is a phenomenon quite recurrent in astrophysical simulations, and because of this, a large dynamical range is required to properly resolve the dynamics of the problem. However, limited computational resources are not always sufficient to solve the small scales. As a consequence of this issue, some numerical artifacts to deal with this problem have arisen. One of them, includes a change in the equation of state, heating the gas in small regions, and avoiding their collapse. However, the change in the physics at those scales sometimes is more a problem than a solution. Instead of stopping the collapse artificially, another way to approximate the unresolved scales has been formulated, the so-called sink particles.

The *sink* concept was coined by Boss & Black (1982) in the context of rotating, isothermal interstellar clouds. They used an Eulerian code where they defined *sink cells*. A sink cell corresponded to the innermost cell in order to remove from calculations details about what was happening to the core of the cloud. These sink cells had the disadvantage that they were fixed in the grid. Based on this approach, Bate et al. (1995) were the first ones into implement sink particles such as. They took the advantage of the Lagrangian nature of smoothed particle hydrodynamics (SPH) codes to build them up. Krumholz et al. (2004) introduced sink particles in Eulerian, grid-based codes, built upon the adaptive mesh refinement (AMR) technique. Their implementation has been a role model for further implementation in grid-based codes.

A sink particle is a particle that approximates the unresolved scale by an immediate collapse into a single point. This point is disconnected from hydrodynamics, and interacts with the remaining gas through gravity and accretion only, it also interacts gravitationally with other sink particles that may be formed. In principle, sink particles are meaningless from a physical point of view, however, according to the formulation to create them and the context, they can be treated as specific structures, for example: stars, stellar clusters or black holes.

RAMSES is a code that allows the implementation of sink particles, the current formulation is presented in Bleuler & Teyssier (2014), which is the formulation used in this work with slight modifications, see Section 1.3.2. There are also several phenomena considered whose specifications are shown in the next section.

There exists several implementations of sink particles into AMR codes, in some of them particles are formed based on purely local quantities, it means gas properties associated to the corresponding cell only (Krumholz et al., 2004). In some others, a small volume is considered around density peaks above a given density threshold, and a criteria based on quantities integrated over such a volume is applied to allow sink formation. This volume is typically chosen to be a sphere of a radius equal to the *accretion radius*. Such a region is typically defined by the user. Four times the smallest cell size is commonly used in the literature. The formulation used in the code is an extension of the latter technique.

Sink particle formation in RAMSES

RAMSES includes a self-denominated *clump-based* technique to form sink particles. Unlike other techniques, this one requires a peak to have a certain *prominence*; defined in the code as the ratio between a peak density and its closest saddle point. Peaks that fail this criterion are considered as *noise* and are merged to neighbouring ones. This provides a more robust segmentation of the volume into a discrete set of sub-regions, excluding small density fluctuations from the analysis. The method consists roughly of the following steps: Checking for the creation of new sink particles after every coarse time step. Running the clump finder to identify peaks and their associated regions denominated clumps. The peak locations identified by the clump finder are taken into account as possible locations for sink formation. For each of these locations it is defined a region containing all the cells that lie within the accretion radius from the location considered. The gas inside this region must fulfill several checks in order to form the sink particle. A clumpfinder is used to identify the regions from which sink particles may form. The clumpfinder algorithm is schemed in Figure 1.2 and described below (for further details see Bleuler & Teyssier (2014)):

- All cells are identified (Figure 1.2.a in grey).
- In a first step, every cell whose density is higher than a given threshold $\rho_{\rm sink}$ is marked (Figure 1.2.b in green).
- Every marked cell is then assigned to a density peak by following the path of steepest ascent. The found maxima are labeled with a global peak-id. All cells above the threshold are sorted in descending density. Then, every cell is assigned to the peak-id of its densest neighbour. All cells sharing the same peak-id form a so called 'peak patch' (Figure 1.2.c in color).
- The saddle point densities connecting between all peak patches are identified. The highest saddle point lying on the boundary of a certain peak patch is the relevant one for the analysis. By looking at the ratio of the peak density to the maximum saddle density of a peak it is decided whether this is a significant one or not, this ratio is called 'prominence' and its value is usually required to be bigger than 2. If a peak patch is isolated, its density peak is compared to the density threshold $\rho_{\rm sink}$.

– The peak patches are sorted by ascending peak density. Insignificant peak patches are merged to the one they are connected to through the highest saddle point. Isolated peak patches which are insignificant are rejected (Figures 1.2.d and 1.2.e).

– After the previous step all insignificant peak patches have been rejected or merged to form significant ones, these ones are now labeled as clumps (Figure 1.2.f).

If a clump is well-defined and all the checks are satisfied in the accretion region, the sink particle formation will take place, its mass will be a fraction of the densest cell in the region from which it is going to form.

Merger

Sink particles are allowed to merge each other if a certain criteria is met, in this case the criteria is if they are close enough. This *close enough* is a free parameter, but I set it up to be the accretion radius, for this thesis such a value has been set to be 4 times the smallest cell in the simulation.

If a couple of sink particles merge, the new mass, position and velocity for the new sink are calculated following the next equations.

$$m_{new} = m_1 + m_2 \tag{1.26}$$
$$\vec{r}_{new} = (\vec{r}_1 \cdot m_1 + \vec{r}_2 \cdot m_2)/m_{new} \tag{1.27}$$
$$\vec{v}_{new} = (\vec{v}_1 \cdot m_1 + \vec{v}_2 \cdot m_2)/m_{new} \tag{1.28}$$
$$\dot{M}_{new} = \dot{M}_1 + \dot{M}_2 \tag{1.29}$$

Here m represents the mass of the sink, $\vec{r}$ stands for the position of the particle, $\vec{v}$ the velocity and $\dot{M}$ the accretion rate, the subscript represent of which sink I am referring to.

Accretion

Sink particles accrete gas from nearby cells, there are different methods to calculate the accretion rate, thus the new physical parameters. Regardless of the adopted scheme, velocity and position of accreted gas relative to the particle are used to update sink position and velocity, angular momentum removed from gas is kept by the sink too, the code updates physical parameters from sink following the equations

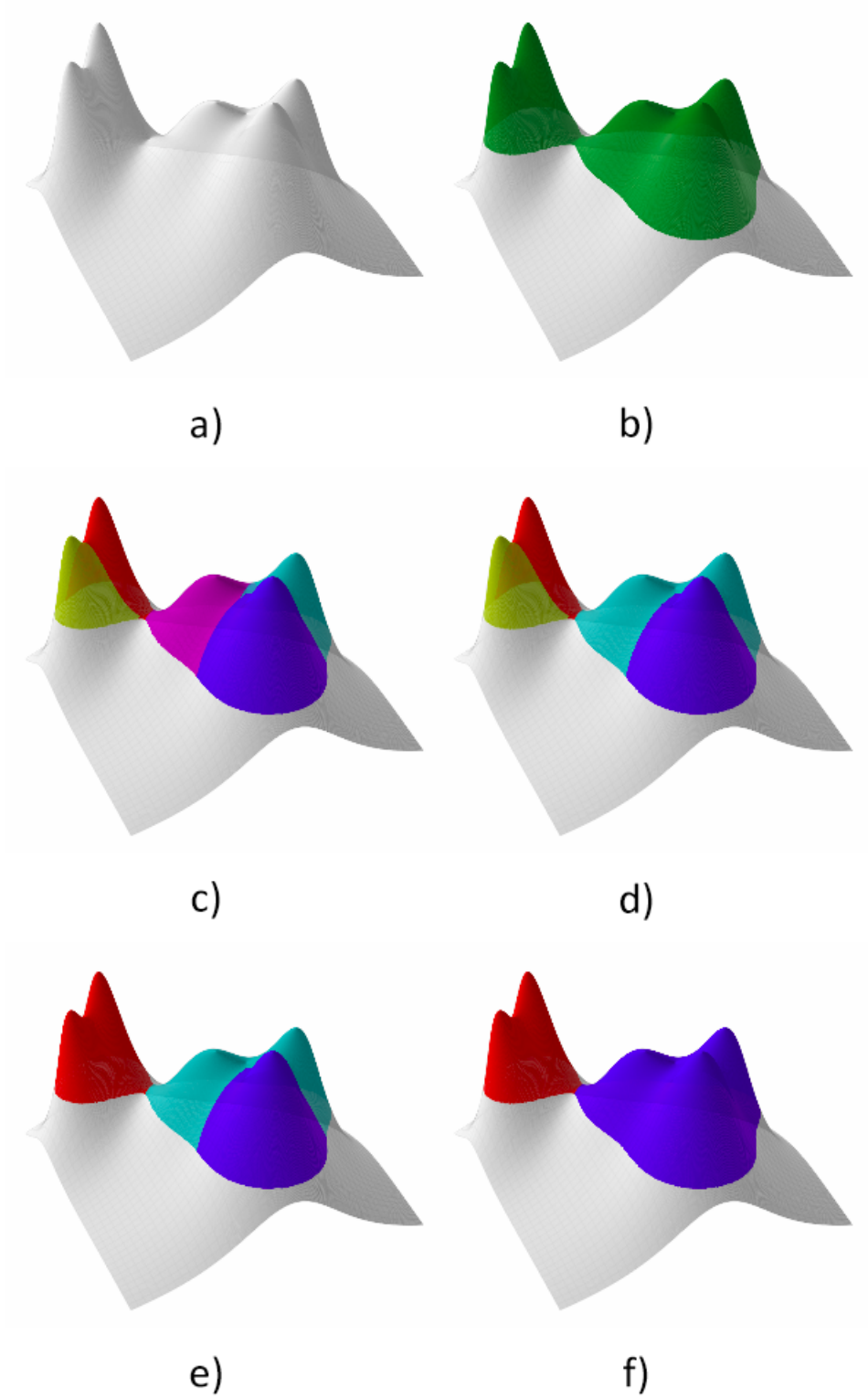

Figure 1.2: Working principle of the clumpfinder represented on a 2d-surface. a.- The whole domain is identified. b.- All cells above a given threshold $\rho_{\rm th}$ are marked. c.- All cells above the density threshold are grouped up with the densest peak. d, e.- Irrelevant groups are merged to one connected through the highest saddle point. f.- Once all irrelevant peaks are merged, the remaining ones are labeled as clumps, from which sink particles can be formed. Image modified from Bleuler & Teyssier (2014).

$$M_s^{\text{new}} = M_s^{\text{old}} + \sum_{\text{i}} \Delta m_{\text{i}} \tag{1.30}$$

$$\vec{R}_s^{\text{new}} = \left(\vec{R}_s^{\text{old}} M_s^{\text{old}} + \sum_{\text{i}} \vec{r}_{\text{i}} \Delta m_{\text{i}} \right) / M_s^{\text{new}} \tag{1.31}$$

$$\vec{V}_s^{new} = \left(\vec{V}_s^{\text{old}} M_s^{\text{old}} + \sum_{\text{i}} \vec{v}_{\text{i}} \Delta m_{\text{i}} \right) / M_s^{\text{new}} \tag{1.32}$$

$$\vec{L}_s^{\text{new}} = \vec{L}_s^{\text{old}} + \left(\vec{R}_s^{\text{new}} - \vec{R}_s^{\text{old}} \right) \times \left(\vec{V}_s^{\text{new}} - \vec{V}_s^{\text{old}} \right) M_s^{\text{old}} + \sum_{\text{i}} (\vec{R}_s^{\text{new}} - \vec{r}_{\text{i}}) \times \left(\vec{V}_s^{\text{new}} - \vec{v}_{\text{i}} \right) \Delta m_{\text{i}} \tag{1.33}$$

In Equations 1.30, 1.31, 1.32, 1.33, M_s^{new} corresponds to the update in the sink particle mass after a time step, M_s^{old} is the sink particle mass before of it, Δm_{i} corresponds to the mass of every cell i from which matter is accreted, $\vec{R}_s^{\text{new}}$ is the update in sink particle position, $\vec{R}_s^{\text{old}}$ is the sink particle position previous accretion, $\vec{r}_{\text{i}}$ is the position of the cells i from which matter is being accreted, $\vec{V}_s^{\text{new}}$ is the update in sink particle velocity, $\vec{V}_s^{\text{old}}$ is the sink particle velocity previous accretion, $\vec{v}_{\text{i}}$ is the velocity of the cells i from which matter is being accreted, $\vec{L}_s^{\text{new}}$ is the angular momentum of sink particles after a time step, $\vec{L}_s^{\text{old}}$ is the angular momentum of sink particles after a time step,

From all the methods available in RAMSES for the sinks to accrete gas, I have used the one denominated *Flux accretion*, it basically sets the accretion rate equal to the mass flux rate into the sink accretion zone. This equation comes from applying the Gauss' divergence theorem into the continuity equation.

$$\dot{M}_{\text{flux}} = -\int_{\Omega_{\text{acc}}} \nabla \cdot (\rho(\vec{v} - \vec{v}_{\text{sink}}))\text{d}V \tag{1.34}$$

where $\dot{M}_{\text{flux}}$ is the mass accreted, Ω_{acc} is the accretion region, ρ is gas density, $\vec{v}$ is gas velocity, and $\vec{v}_{\text{sink}}$ is accreting sink velocity.

Bleuler & Teyssier (2014) take a fraction of this value, to keep the gas density inside the accretion zone close to the sink threshold density in the long term.

$$\dot{M}_{\text{FA}} = \left[1 + 0.1 \log \left(\frac{\bar{\rho}}{\rho_{\text{sink}}} \right) \right] \dot{M}_{\text{flux}} \tag{1.35}$$

In the above equation $\bar{\rho}$ is the mean density in the accretion zone, while ρ_{sink} is the threshold density set by the user.

From the accretion rate, the gas mass removed from a cell Δm_{i} in the accretion zone is computed in mass-wighted fashion

$$\Delta m_{\rm i} = \begin{cases} \Delta t \frac{\dot{M}_{\rm FA}}{n_{\rm cells}} \frac{\rho_{\rm i}}{\bar{\rho}} & \text{if } \dot{M}_{\rm flux} \geq 0 \\ 0 & \text{if } \dot{M}_{\rm flux} < 0 \end{cases} \tag{1.36}$$

where $n_{\rm cells}$ is the number of cells in the accretion zone, $\rho_{\rm i}$ is the density in the cell and $\bar{\rho}$ is the mean density in the accretion zone.

1.3 Modifications to the RAMSES code

I made several changes in the implementation of the code in order to suit in the best possible way the physical conditions. These changes are crucial for the proper performance of the phenomena that will happen.

1.3.1 RAMSES

The RAMSES code by default includes a scheme in which gas is heated in regions where the Truelove criterion (see Section 1.1.1) is violated by setting an artificial temperature floor. The implementation of this approach prevents the gravitational collapse beyond the highest level of refinement, which correspond to regions where the formation of massive seeds is made through the formation of sink particles. Because of this, this scheme was removed from the code. This implementation is compatible with the original implementation in the formation of sink particles, however, it is not compatible with the changes presented in Section 1.3.2.

1.3.2 Sink particles

Creation

Bleuler & Teyssier (2014) defined three conditions for a sink particle to be created, these are called checks, and they are based on physical conditions necessary for the collapse to proceed, all the quantities associated to them are calculated in the region containing all the cells in the accretion radius. First, the *virial check* must be satisfied, this is a condition that states that the region must be contracting by following $\ddot{I}_{\rm cm} < 0$ according to the virial theorem, recalling that virial equilibrium is sustained when $\ddot{I}_{\rm cm} = 0$, where $I_{\rm cm}$ is the moment of inertia in the center of mass frame.

Second, the *collapse check* must be accomplished, which requires that the region must be collapsing along its three main axis in order to form a sink particle. Finally, the *proximity check*, in which a sink particle cannot be created if it is in the accretion region of another one, even if it meets all previous criteria for its formation.

Even though Bleuler & Teyssier (2014) defined three physically reasonable checks, the first test simulations that I performed did not form any sink particle, or when they did, they

were localized in low density regions. Also, the code also ended up crushing and the KROME code did not work properly. Because of this, I replace the checks with another ones. The new ones are denominated *max level check*, *jeans check*, while I kept invariant the *proximity check*, the new checks are based on the work made by Latif & Volonteri (2015).

The *max level check* consists of allowing a sink particle form if the clump density peak is localized in a cell at the highest resolution level, by doing this I ensure that sink particles will form in dense regions. I also added the *jeans check*, in which a sink particle forms if the mass of the densest cell is larger than the Jeans mass, as a criterion to determine if gravity will overcome pressure gradient.

Also, when a sink particle forms, under the *by default* algorithm, the sink particle mass became 10^{-10} times the mass of the densest cell in the formation region, which is not sustained by any numerical nor physical condition. Because of this, I change the mass of the sink based on what was done by Latif & Volonteri (2015). Sinks have assigned masses so that a cell becomes Jeans stable after the subtraction of the sink mass. Basically:

$$m_{\text{sink}} = m_{\text{old-cell}} - m_{\text{jeans}} \tag{1.37}$$

$$m_{\text{new-cell}} = m_{\text{jeans}} \tag{1.38}$$

where m_{sink} is the mass of the sink particle created, $\text{m}_{\text{old-cell}}$ is the mass of the cell before the sink particle creation, m_{jeans} is the Jeans mass of the cell from which the sink particle will be created, and $\text{m}_{\text{new-cell}}$ is the mass of the cell after the sink particle is created.

In Figure 1.3, I show an example of a test in which I compared both checks to form sink particles. Black dots represent sink particles formed using Bleuler & Teyssier (2014) checks, while red dots represent sink particles formed using the changes mentioned above. As can be seen, black dots are formed in low density regions that are properly resolved in the code, while red dots are located in overdense regions in which the collapse is not being well resolved and the formation of a structure may take place.

For this work I have used a threshold density to allow cells to become sink particles of $\rho_{\text{sink}} = 10^{-18}$ gr/cm^3 and the accretion radius has been defined to be 4 times the smallest cell in the run.

Accretion

The scheme for sink particles to accrete matter from nearby cells is described in Section 1.2.3, and is represented in Equation 1.35. However, that rate is modified in order to make accretion independent of the threshold chosen, so the accretion rate is simply the following

$$\dot{M}_{\text{FA}} = \dot{M}_{\text{flux}} \tag{1.39}$$

where $\dot{M}_{\text{FA}}$ is the sink accretion rate used to update the sink particle mass, and $\dot{M}_{\text{flux}}$ is defined in Equation 1.34

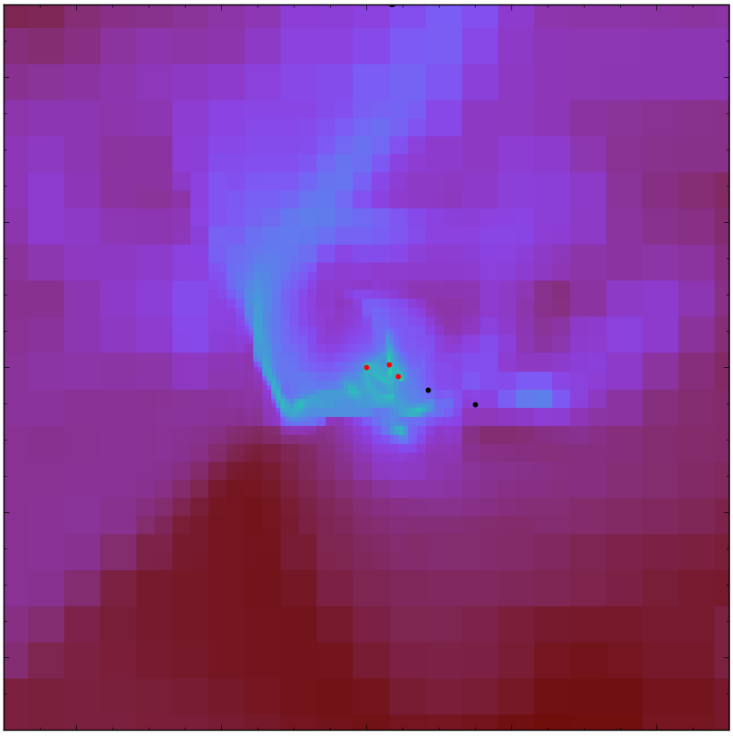

Figure 1.3: Density projection for a test simulation. Black dots represent sink particles formed out by making use of the *by default* algorithm. Red dots represent sink particles formed out by including all the changes in the checks.

Chapter 2

Dark Matter-only simulations

I performed 3D simulations to study the effect of gas fragmentation in the formation of primordial SMBHs in three different dark matter halos. I started from only Dark Matter (DM) low-resolution simulations initialized at $z = 99$ in 1 cMpc/h box side with the use of the MUSIC code (Hahn & Abel, 2011). In these simulations all dark matter particles have the same mass, which is roughly 60000 $M_\odot$. Fifty simulations were performed, in order to have a variety of halos to be re-simulated. The runs were stopped at redshift ~ 9, then I proceeded to use the HOP halo finder (Eisenstein & Hut, 1998) to find all dark matter halos.

In total 15552 halos were found from a total of 50 low-resolution simulations. However, 341 halos had to be discarded, since they were positioned at one of the edges of the box. In Figure 2.1 there is an example of one of the large structures simulated. Also it is shown a halo identified close to one of the box boundaries. The white circle encloses the virial radius for that halo. The problem with halos positioned at edges arises when they are tried to be re-simulated. The MUSIC code, by making use of the zoom-in technique locates the region of interest in the center of the box, the relocation of the halo may generate numerical issues. Also, the calculation of some physical parameters (e.g. spin parameter) for these halos turns to be troublesome.

From the 15211 halos not localized at one of the box edges, 7689 ($\sim 50\%$) correspond to halos composed of more than 100 dark matter particles. Below this value, dark matter halos found are considered noise, since they lack enough particles to rely on their dynamics and internal processes. From the total amount of dark matter halos found, 454 ($\sim 3\%$) are more massive than 5 $\times 10^7$ $M_\odot$, which is the mass that I am interested in. In a Direct Collapse Black Hole scenario, such amount of mass is necessary, due to the virial temperature associated with this value. All virialized halos with masses higher than 5×10^7 $M_\odot$ have virial temperatures of the order of 8000 of Kelvin and above. This value can be checked by making use of equation 2.1, and by setting $T_{\rm vir} = 8000$ K, $R_{\rm vir} = 2$ kpc, and considering μ for a primordial chemical composition. At those temperatures, the atomic cooling overcomes molecular cooling (See Section 0.2).

$$T_{\rm vir} = \frac{2GM_{\rm vir}\mu m_H}{3R_{vir}k_B} \tag{2.1}$$

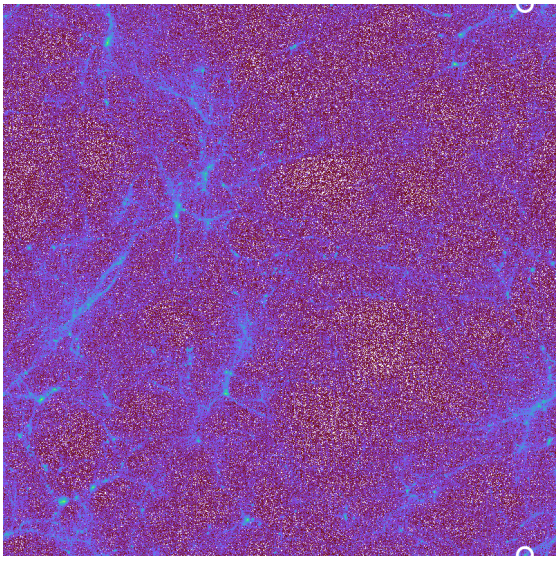

Figure 2.1: Dark-matter particle projection plot for one of the fifty simulations. The white circle encloses a dark matter halo identified at one of the box edges.

In Figure 2.2, the halo mass distribution is shown for all dark matter halos found by the end of the runs. The red line represents the halos composed of 100 dark matter particles. On the other hand, the orange line in the figure denotes the lower limit in mass for dark matter halos to reach the virial temperature required to allow the atomic cooling, it means 5×10^7 $M_\odot$.

Once the information of all halos found was acquired, three of them were selected. This selection was based on three criteria: i) halo mass, ii) halo spin parameter, and iii) merger history. Halo masses were required to be higher than $\sim 5 \times 10^7$ $M_\odot$, for reasons explained above. However, massive isolated halos are rare to find in 1 cMpc/h box sizes, this is the main reason to have performed 50 low-resolution simulations.

In addition to high temperatures, hence, massive halos, UV intensity (J_{21}) is used as a parameter to determine the feasibility of a DCBH scenario. However, it is too simplistic, since dynamics affect the chemistry and the conditions to allow such a scenario. This is why we also made our choice based on selecting various halo spin parameters and by checking the merger status using merger trees.

There are two ways to quantify spin in galactic halos. Peebles (1969) first proposed a dimensionless spin parameter (Equation 2.2),

$$\lambda \equiv \frac{\sqrt{E}|\vec{J}|}{GM^{5/2}} \tag{2.2}$$

where E is the total energy, $|\vec{J}|$ is the magnitude of the total angular momentum and M is the virial mass. However, this spin parameter includes an annoying term, which is the potential energy. This value cannot be obtained directly in observations, and from the side of numerical simulations, the calculation of such a term is computationally expensive.

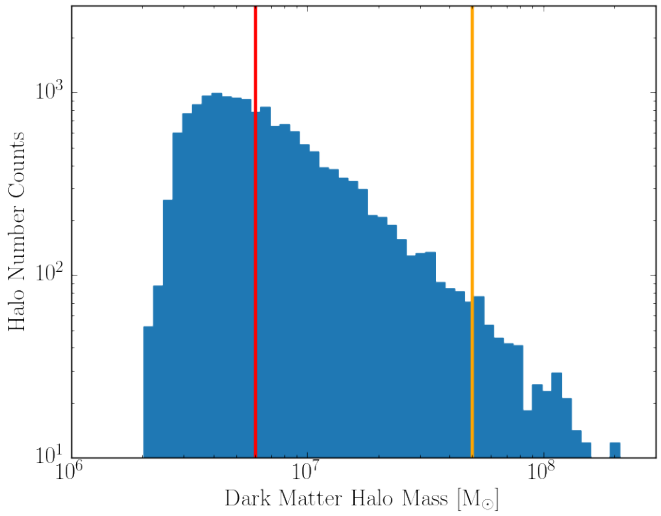

Figure 2.2: Mass distribution for all halos found in our 50 DM-only low-resolution simulations. The red line delimits the region at which halos are made up 100 dark matter particles. The orange line represents the threshold at which atomic cooling becomes efficient.

On the other hand, Bullock et al. (2001) proposed an alternative spin parameter to quantify rotation in dark matter halos (Equation 2.3),

$$\lambda \equiv \frac{|\vec{J}|}{2MRV} \tag{2.3}$$

where $|\vec{J}|$ is the magnitude of the total angular momentum, M is the virial mass of the halo, and V is the virial velocity defined as $V = \sqrt{GM/R}$, where R is the virial radius. This parameter is more straightforward to calculate, so it will be the one used for spin analysis. M and R are numbers given by the HOP algorithm for each halo, therefore, V. So, to calculate spin parameters the angular momentum $|\vec{J}|$ is the only number left. Equation 2.4 shows the formula used to calculate the angular momentum in halos. This formula is just the angular momentum definition applied to all particles in the halo.

$$\vec{J} = \sum_{\mathrm{i}}^{n_{\mathrm{part}}} m_{\mathrm{i}} \vec{r}_{\mathrm{i}} \times \vec{v}_{\mathrm{i}} \tag{2.4}$$

In this equation n_{part} represents the total number of particles in the halo, m_{i} represents the mass of the particles, $\vec{r}_{\mathrm{i}}$ stands the position of a particle relative to the center of mass of the halo, while $\vec{v}_{\mathrm{i}}$ is the velocity relative the halo bulk velocity. In addition to virial masses and virial radii, HOP also gives the position and velocity of the center of mass. The HOP algorithm was used through the **yt-code** (Turk et al., 2011).

Bullock et al. (2001) also showed that the spin parameter defined in this same work follows a log-normal distribution (Equation 2.5), with a μ and a σ of 0.035 ± 0.005 and 0.5 ± 0.03 respectively. In Figure 2.3 the spin distribution for all halos found in my DM-only low-

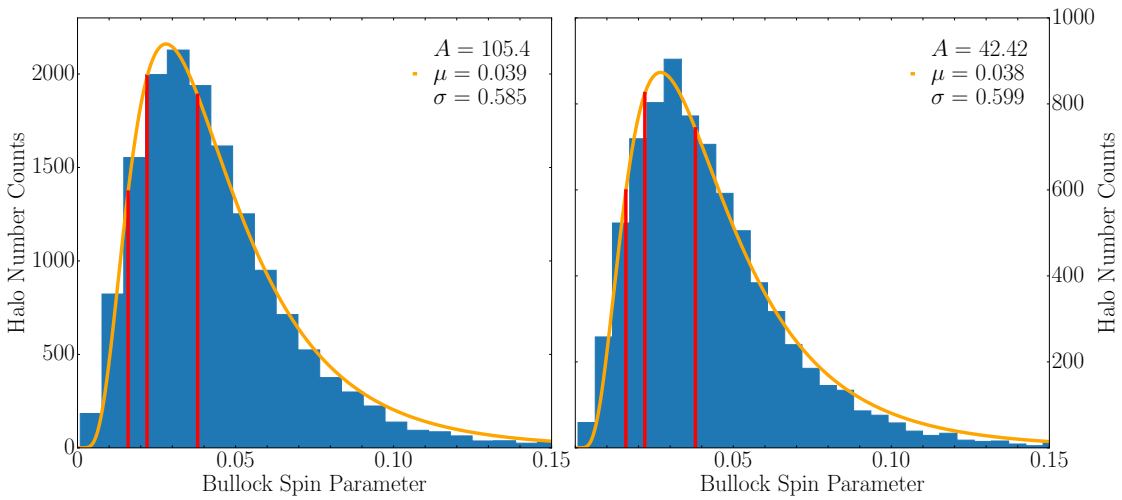

Figure 2.3: Bullock spin parameter distribution for dark matter halos simulated. In the left the spin distribution is shown for all halos found in the halo finder, while in the right the distribution just considers halos composed of more than 100 dark matter particles. On both cases the orange line represents the best log-normal fitting function, with their respective fitting parameters. The red vertical lines represent the spin parameter of the halos chosen to be re-simulated.

resolution simulations is shown. In the left panel, the spin distribution corresponds to all halos found, while in the right, it is just considering the distribution for all halos composed of more than 100 dark matter particles. In both cases, halos close to the edges are not considered, since their spin parameter could not be calculated. In both panels the orange line represents the best log-normal fitting function. Values of $A = 105.4$, $\mu = 0.039$, and $\sigma = 0.585$ are obtained for the fitting function in the left plot. These values correspond to a mean and a standard deviation values of 0.046 and 0.029 respectively in this distribution. In the right plot $A = 42.42$, $\mu = 0.038$ and $\sigma = 0.599$, which corresponds to a mean and a standard deviation of 0.045 and 0.029 respectively. In both cases the fitting parameters μ and σ stay very similar, while A is just a normalization factor which takes the total number of halos considered into account, so their mismatch is expected. Also, in both figures red vertical lines are plotted, which represent the spin parameters for the halos selected. From left to right, they resemble spin parameter values of 0.016, 0.022, and 0.038.

$$p(x) = \frac{A}{x\sqrt{2\pi}\sigma} \exp\left(-\frac{\ln^2(x/\mu)}{2\sigma^2}\right) \tag{2.5}$$

The chosen spin parameters lie at 1.02, 0.82, and 0.27 standard deviations from the mean value in the function (relative to the spin distribution that considers all halos found). All chosen values are below the mean, but they still represent a good diversity, therefore, dynamics.

The chosen halos are denominated A, B and C and their properties such as Bullock spin parameter (Bullock et al., 2001), virial mass, virial radius, and the number of dark matter

Table 2.1: Virial Mass, Virial radius, spin parameter and number of particles in the low resolution DM-only simulated halos

Halo	Virial Mass [$M_\odot$]	Virial Radius [kpc]	Spin Parameter	n_{part}
A	9.68 $\times 10^7$	2.07	0.016	1612
B	4.90 $\times 10^7$	2.14	0.022	821
C	2.68 $\times 10^8$	2.30	0.038	4471

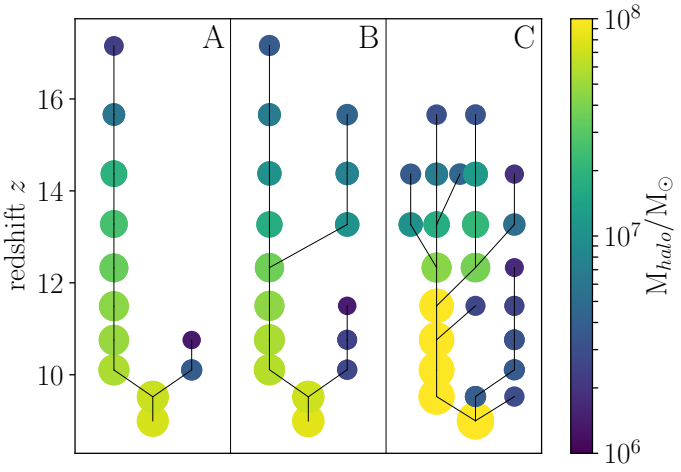

Figure 2.4: Merger-trees for selected halos, evolution goes downwards. Halos A, B, and C go from left to right respectively. Masses are represented with colors, also circle radii. The y-axis represents redshift while the x-axis remains dummy

particles are shown in Table 2.1. In Figure 2.4 merger trees for all selected halos are shown. The number of halo mergers is one for A, while it is two for B. The mass ratio for the only merger in A is 0.067. This halo is characterized to have the lowest spin parameter value. For halo B, mass ratios are 0.60 and 0.04 (top and bottom respectively according to the figure). Halo C turns to be the one formed out of a high number of mergers. Also, it is the halo with the highest spin parameter from my sample. Successive mergers seem to be necessary to ensure a high spin parameter (Peirani et al., 2004).

Chapter 3

Hydrodynamic simulations

Once the halos were chosen, they were re-simulated including gas physics, also making use of the KROME package and the zoom-in technique included in the MUSIC code. I also added the modified algorithm to form sink particles (see Section 1.2.3). The zoom-in was made enclosing a spherical region of a size equal to the virial radius for the respective halo. Such a choice does not affect the final results since all structures are formed at scales orders of magnitude below the virial radius as we will see in next sections. In all DM-only low-resolution simulations, virial radius had a value of $\sim$2 kpc at the end of their run.

For all re-simulations, a uniform UV background was added with intensity values of $J_{21} = 10000$ and $J_{21} = 10$, several extra intensities are analyzed by the end of this chapter. In Tables 3.1 and 3.2 some sink features for the results are summarized; the redshift at the moment at which the first sink particle formed and its corresponding cosmic age, the total number of sink particles formed during the run, the number of sink particle mergers, the initial first sink particle mass, the final first sink particle mass, and two average accretion rates for the first sink particle.

Table 3.1: Sink features for the simulations: redshift and cosmic age at which the first sink particle formed, amount of sinks formed during the run, and amount of mergers during the run for each respective halo.

Halo	J_{21}	z	Cosmic age (Myr)	N° sinks formed	Sink mergers
A	10000	11.28	400.1	1	-
	10	13.11	324.4	3	1
B	10000	10.08	466.9	1	-
	10	11.03	412.5	8	2
	5	11.04	412.0	9	2
C	10000	10.80	425.0	3	1
	10	12.37	351.9	7	2

Table 3.2: Sink features for the simulations: UV intensity, initial and final mass for the first sink particle created, average accretion rate for the first sink particle created in each run considering the first 300 kyrs in the simulation, and also the whole run.

Halo	J_{21}	Initial sink mass ($M_\odot$)	Final sink mass ($M_\odot$)	Average accretion rate in 300 kyrs ($M_\odot$/yr)	Average accretion rate ($M_\odot$/yr)
A	10000	132	8.8×10^4	0.293	0.299
	10	13	2.7×10^4	0.009	0.005
B	10000	518	2.2×10^5	0.574	0.374
	10	18	1.6×10^4	0.008	0.002
	5	194	1.2×10^4	0.008	0.002
C	10000	43	5.5×10^4	0.138	0.108
	10	187	2.4×10^4	0.007	0.005

From Table 3.1, it can be observed that sink particles are formed earlier in cosmic time when UV intensity is decreased. This can be understood from the fact that $M_{jeans} \propto T^{3/2}$. At low UV intensities, the gas is cooled down, so the thermal jeans mass decreases and regions collapse sooner compared to high UV intensities, in which gas remains hot and allows the assembly of baryons for a more extended period of time.

3.0.1 High UV intensity

Results will vary depending on every halo and UV intensity. Halos with a high UV intensity, are expected to behave in similar ways, as H_2 is expected to be inhibited, a DCBH is expected to form (Shang et al., 2010; Latif et al., 2014b). For this section, I will adopt a $J_{21} = 10000$ value.

Dynamics

I performed simulations for each halo using a uniform UV background of $J_{21} = 10000$. The evolution was followed during roughly 350 kyrs after the first sink particle formed, which corresponds to a couple of growing times $t_{\rm growth} = M_{\rm sink}/\dot{M}_{\rm sink}$ for these runs. This characteristic time $t_{\rm growth}$ varies for all runs and sink particles, as can be seen in Figure 3.1. This time tends to increase as the simulations go on, but is kept roughly constant in the range of 50 - 300 kyrs after the first sink particle forms in every simulation. This time increases almost continuously with time, as a consequence of the increase in the sink mass and a decrease in the accretion rate as it is shown later. In Table 3.3, average growth times are summarized. It is observed how this value increases when moving from halo A to C. Also, it can be seen how it changes if just the first 300 kyrs are considered to compute the average. For halo C just the growth time for the first sink particle formed is shown in Figure 3.1, also in Table 3.3.

Figure 3.2 represents projections of all halos at a scale of 3 kpc (top) and a scale of 100 pc (bottom) at the end of each respective run. The projection for halos A and B is centered

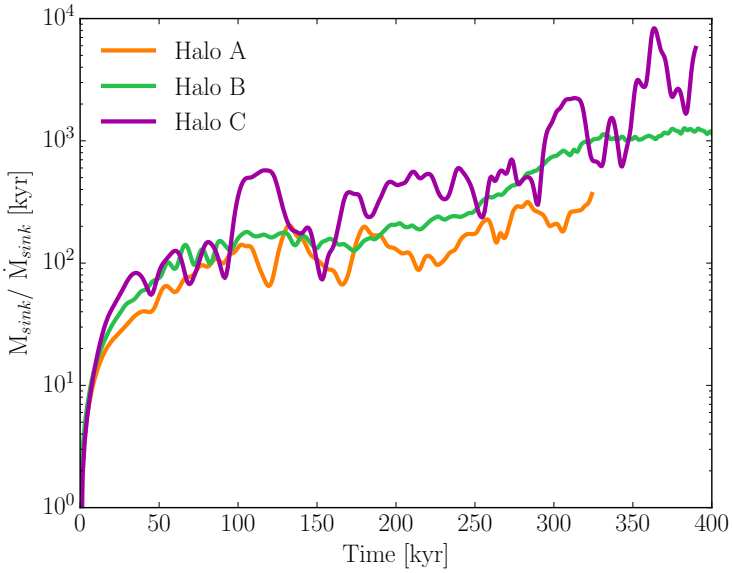

Figure 3.1: Growth time as a function of time for the sink particles formed in each respective run. For halo C, just the first sink particle formed is considered.

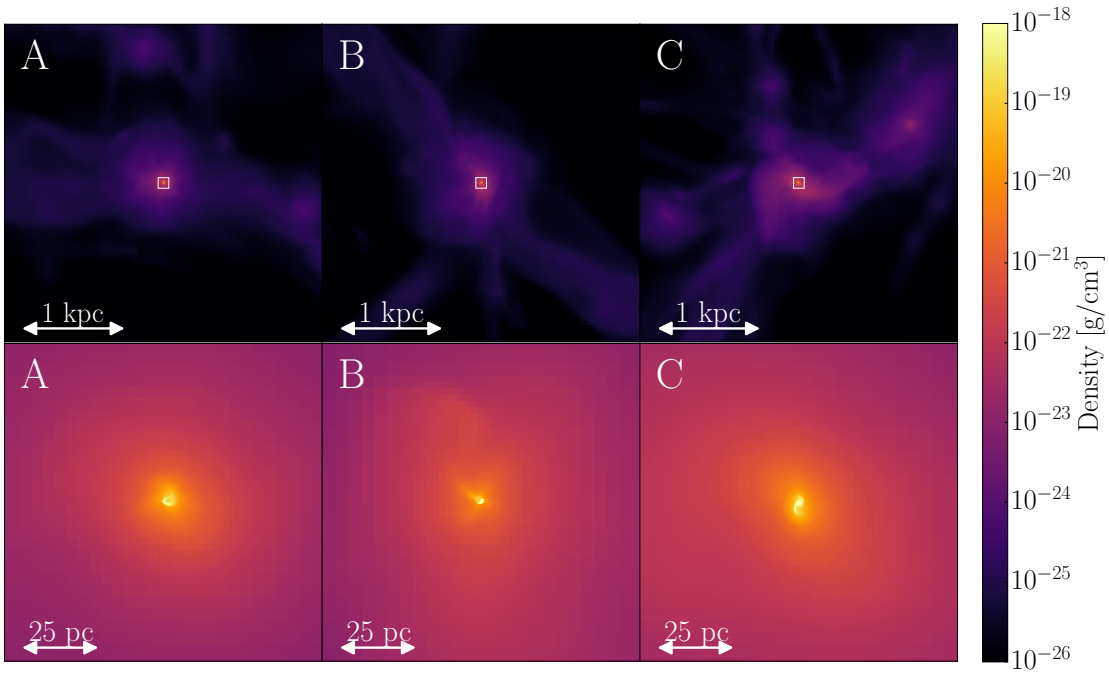

Figure 3.2: Density projection for all re-simulated halos irradiated by a UV background of $J_{21} = 10000$ at the time when the runs finish. Halos A, B, and C go from left to right respectively. At the top, projections correspond to 3 kpc, where white squares correspond to 100 pc regions, which are shown at the bottom.

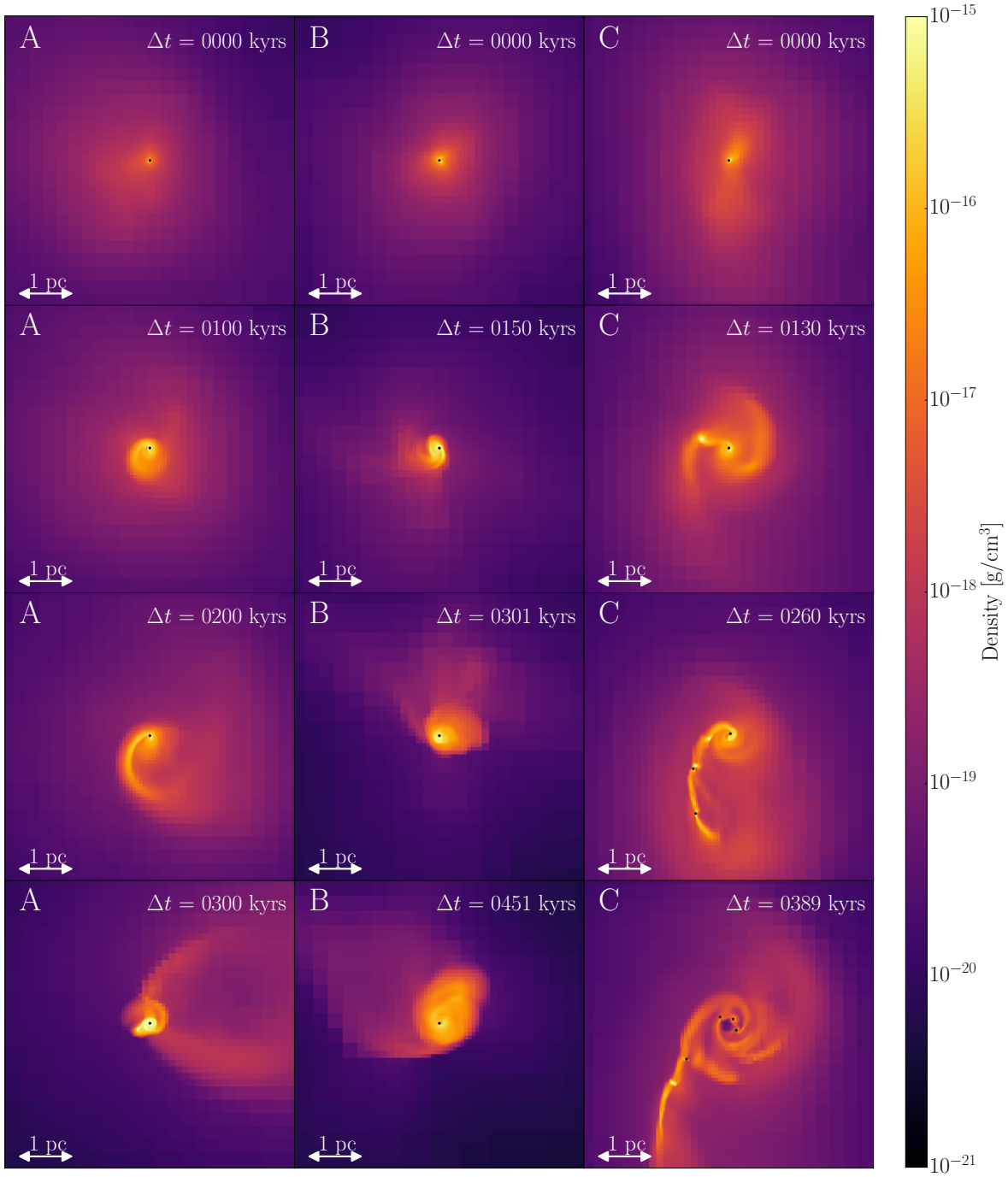

Figure 3.3: Density projection for all re-simulated halos irradiated by a UV background of $J_{21} = 10000$ at a scale of 5 pc. Halos A, B and C go from left to right respectively. Several epochs are shown, Δt represents the age of the simulation relative to the age of the first sink particle formed in the respective run.

Table 3.3: Averaged growth time for re-simulated halos under the influence of a strong UV background. The average in the left considers the whole run, while the average in the right just the first 300 kyr.

Halo	Average growth time [kyr]	Average growth time in the first 300 [kyr]
A	154	141
B	678	225
C	977	341

in the only sink particle formed, while for C it is in the center of mass of all sink particles. We can observe the formation of a dense central spherical structure at both large and small scales. At large scales, we can see some filaments feeding with gas every halo. This picture does not change significantly with time. At the center of these structures sink particles are created (not shown in the plots) and no significant dynamical evolution nor fragmentation is observed during the run.

In Figure 3.3 density projections at a 5 pc scale are portrayed. In all simulations a gas disk was formed, so the projection has been preferred to be in the axis perpendicular to the disk plane. The times shown in the plots (Δt) are the times relative to the first sink particle formed in the respective simulations (see Table 3.1). Δt values shown were chosen based on the growing time, as it was analyzed previously, and also to span the dynamical evolution for the available outputs. Each black dot represents a sink particle. Structure evolution is able to be observed in more detail.

Halos A and B form a structure which initially starts with a spherical shape but soon becomes a disk with spiral arms from which matter is accreted, in both cases just one sink particle forms. Halo C structure evolution is different than the others: it begins with a spherical shape, similar to A and B, from which the first sink particle forms, then a disk structure with two spiral arms is formed by $\Delta t = 130$ kyrs. After that, just one spiral arm survives, which fragments and create consecutively new sink particles. Finally, these particles fall to the center, where they begin to interact gravitationally. Just one sink particle merges to the central one during the run. In Figure 3.4 distances between the first one created and the following are shown as a function of time. The second sink particle formed (orange) falls directly to the center, merging with the first sink particle. The third and fourth (green and purple, respectively) oscillate with the resulting sink particle from the merger. And the fifth sink particle (blue) falls to the center, but it does not reach the same distances as the other ones.

Several mechanisms may trigger the formation of sink particles. However, a stability Toomre analysis allows us to know if they are formed due to local instabilities. The Toomre parameter (Toomre, 1964) is defined as follows (Equation 3.1),

$$Q = \frac{\kappa c_s}{\pi G \Sigma} \tag{3.1}$$

where κ is the epicyclic frequency, c_s is the sound speed, and Σ is the surface density. Toomre

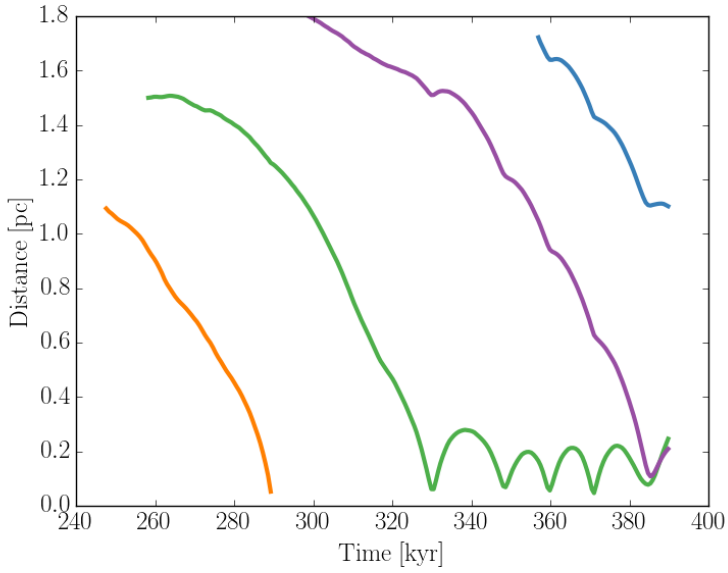

Figure 3.4: Distance between the first sink particle formed and the ones formed later. The orange line represents the second sink particle formed which disappear since it merges with the first sink particle created. The third and the fourth sink particle oscillate around the first. The fifth is farther, but it is seen to fall as well.

parameter values above one represent stable regions, while values lower than one represent unstable regions, hence, regions that will collapse. Unfortunately, κ calculation turns to be problematic, due to its mathematical form (Equation 3.2),

$$\kappa^2(R) = \frac{2\Omega(R)}{R}\frac{\mathrm{d}}{\mathrm{d}R}(R^2\Omega(R)) \tag{3.2}$$

where $\Omega(R)$ is the angular velocity, and R is the distance, both calculated from a given center. Despite of this issue, it is known that κ is constrained between Ω and 2Ω. This fact allows us to use 2Ω instead of κ resulting in the form presented in Equation 3.3. To calculate this parameter with this change turns to be easier and it represents an upper limit.

$$Q = \frac{2\Omega c_s}{\pi G\Sigma} \tag{3.3}$$

In Figure 3.5, a Toomre parameter map is shown for halo C at different epochs. Unlike previous figures, Δt values are picked to be previous to sink particles time creation. As can be seen, regions from which sink particles are made, are regions where the Toomre parameter remains much lower than one, implying an imminent collapse. This simple analysis confirms that sink particles are formed in locally unstable regions.

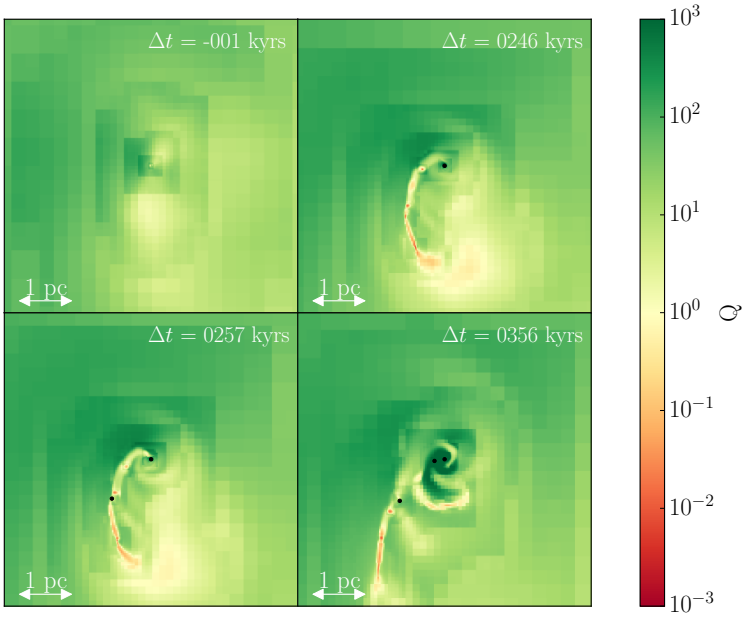

Figure 3.5: Toomre parameter for halo C, Δt were picked one snapshot previous to sink particle creation. Black dots represent sink particles. It can be seen that spiral arms present the smallest Q values. Value higher that one for Q represent stable regions (green), while unstable regions are represent by Toomre parameter values lower than one (red).

Radial Profiles

In addition to the density projections, in Figure 3.6 radial profiles for these simulations are shown. It includes density, temperature, H_2 fraction and mass infall rate. The profiles are also plotted for the same Δt used in Figure 3.3. All the plots are centered in the first sink particle formed, and they span from resolution scales ($\sim 10^{-2}$ pc) up to virial radius scales (1 kpc) since virial radii range 0.9 - 1.5 kpc at the end of the runs. The whole halo is being sampled, i.e. 5 decades in spatial scales.

All density profiles exhibit a nearly isothermal profile $\rho \propto r^{-2}$ (gray dashed line in the top row) with some deviations. For halos A and B there are some peaks in the profiles that represent some spiral arms and the extent of dense regions, as can be seen in the density projections of Figure 3.3. For halo C, several peaks appear at different times. Peaks at $\Delta t = 130$ kyr are related to the spiral arms that can be seen in the disk-like structure formed. For $\Delta t = 260$ kyr the peaks represent other sink particles and their accretion regions, while for $\Delta t = 390$ kyr they represent an overdense clump with no sink particles in it, and the region surrounding the three central sink particles.

Temperature remains roughly constant for halo A and B, with minor and no relevant drops. In both halos, temperature decreases at high densities slowly due to the Lyman-α cooling. This slope has been observed in other works e.g. Latif et al. (2013a). For halo C at $\Delta t = 0$ and 130 kyrs, the temperature profiles are nearly constant with a small slope, similar to halos A and B. But, at $\Delta t = 260$ kyr and 390 kyr, profiles drastically change and drop to lower values at some radii.

The H_2 fraction profiles for A and B show some localized H_2 enhancement with time, but in both halos this effect does not lead to a significant change in temperature profiles, which is due to the fact that H_2 fraction does not exceed 10^{-3} - 10^{-4} value. At roughly such numbers, phase diagrams show that cooling becomes efficient, lowering central temperatures.

The fact that H_2 fractions $> 10^{-3}$ - 10^{-4} are the number needed to ensure molecular cooling can be appreciated in Figure 3.7, which corresponds to phase diagrams for halo C at $\Delta t = 389$ kyrs (Last snapshot shown for this halo). H_2 fraction-Density diagram shows two regions at high densities, one at high H_2 fraction and another one to relatively low H_2 fraction. On the other hand, in the Temperature-Density diagram a similar behavior is appreciated since two regions are identified at high densities, one at thousands of Kelvin degrees, and another at hundreds. Clearly, high temperature region correspond to low H_2 fraction region, in the same way, low temperature regions correspond to high H_2 fraction regions. The transition between both regimes occurs between 10^{-4} and 10^{-3} H_2 fractions.

For halo C there is a huge increase in the H_2 fraction, specially at later stages. In Figure 3.8 projections for temperature and H_2 fraction, selecting Δt according to the projections and radial profiles are shown. In the left side, temperature is plotted, while in the right H_2 fraction is displayed. Molecular hydrogen is observed to be gathered in the spiral arm seen in the density projection. The increase in H_2 also cools down the system. There are several mechanisms to form molecular hydrogen. To know if the direct formation (Equations 2 and 3) is the main one, electron fractions are quantified, since it is a catalyst. Electron fraction maps

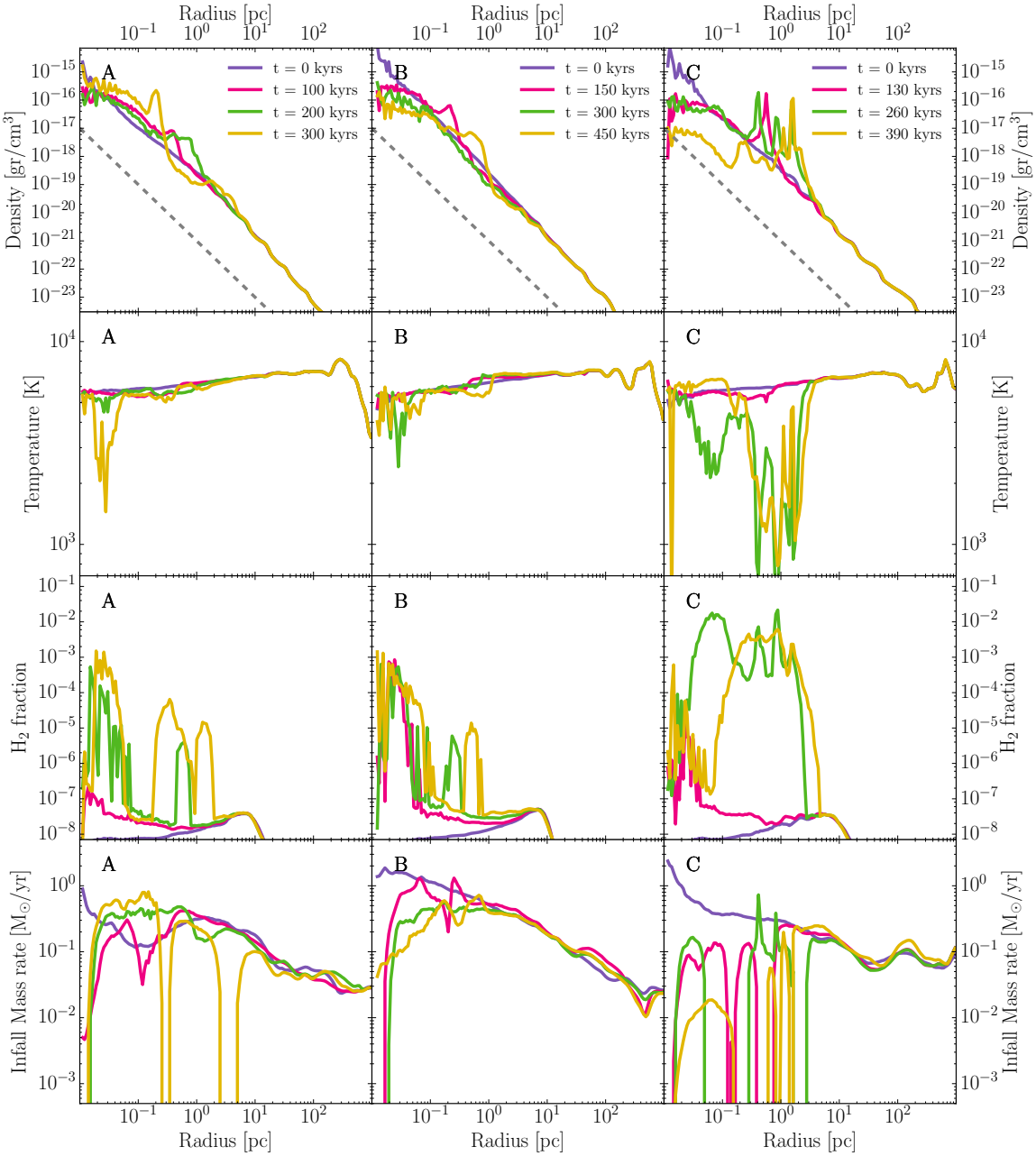

Figure 3.6: Radial profiles for the $J_{21} = 10000$ runs. They include density, temperature, H_2 fraction and infall mass rate. Halos A, B and C go from left to right respectively. The profiles are calculated at the same times (Δt) shown in Fig. 3.3. In density profiles, a dashed gray line is plotted, it represents an isothermal profile $\rho \propto r^{-2}$.

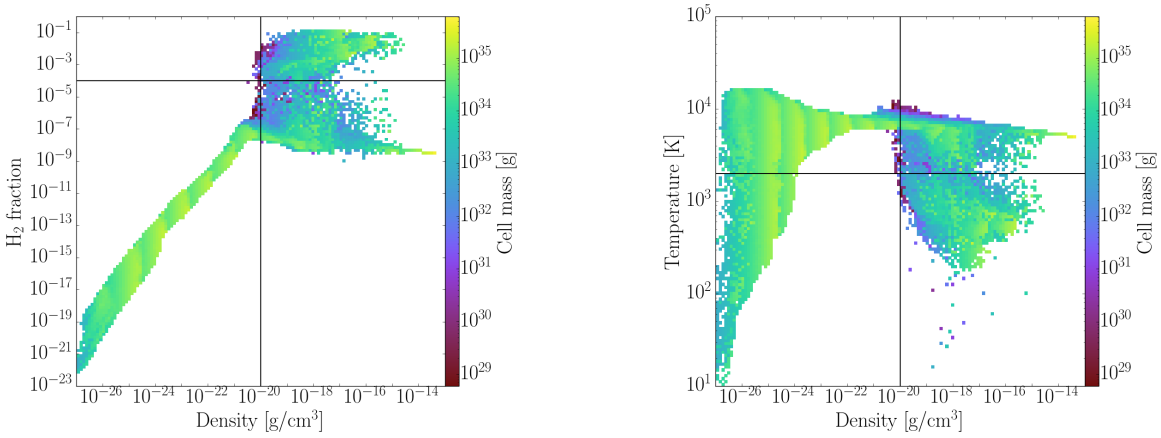

(a) (b)

Figure 3.7: Phase diagrams for halo C under the presence of a UV background of $J_{21} = 10000$. (a) H_2-Density diagram (b) Temperature-Density diagram. Both diagrams were made at the end of the run for this halo.

for halo C are shown in Figure 3.9. There is a lack of electrons in the spiral arms compared to the rest of the structure. This phenomenon explains the huge abundance of H_2, since this element was used to form ionized hydrogen (H^-), which is one of molecular hydrogen catalysts.

In addition to density, temperature, and H_2 fraction, I also added mass infall rates to radial profiles. The previous profiles were calculated by using the implementation presented in the yt-code to compute radial profiles. Mass infall rates were calculated in a different way, it was made by using Equation 3.4, centered in the first sink particle formed position. Equation 3.4 counts all cells at a given radius and calculates the amount of matter crossing a determined area at a given velocity. In equation 3.4, $\rho_{\mathrm{cell,i}}$ represents cell density, $v_{\mathrm{infall,i}}$ corresponds to cell speed along the radial axis towards the center chosen, and $\Delta\Omega_{\mathrm{cell,i}}$ is the solid angle subtended from the center to the portion of the cell that is contributing to the calculations. Notice that $v_{\mathrm{infall,i}}$ has been chosen to be positive if the cell is falling down to the center, and negative if it is moving away from it. Distances, densities, and infall velocities are physical parameters given by the code, while $\Delta\Omega_{\mathrm{cell,i}}$ was calculated exploiting the intrinsic cubic geometry implemented in the RAMSES code: a polyhedron formed between the intersection of the sphere of radius r and the cell that is contributing to the profile was divided in a set of numerous tetrahedrons whose solid angles were determined by using the method described in Oosterom & Strackee (1983).

$$\dot{M}(r) \approx \sum_{\mathrm{i}=0}^{ncells} r^2 \rho_{\mathrm{cell,i}} v_{\mathrm{infall,i}} \Delta\Omega_{\mathrm{cell,i}} \tag{3.4}$$

In all of the runs we can observe regions in which gas is falling down to the center, and regions where the gas is moving away. At most radii, infall mass rate calculations turn out to be positive, implying that most gas is being accreted compared to gas being pushed away.

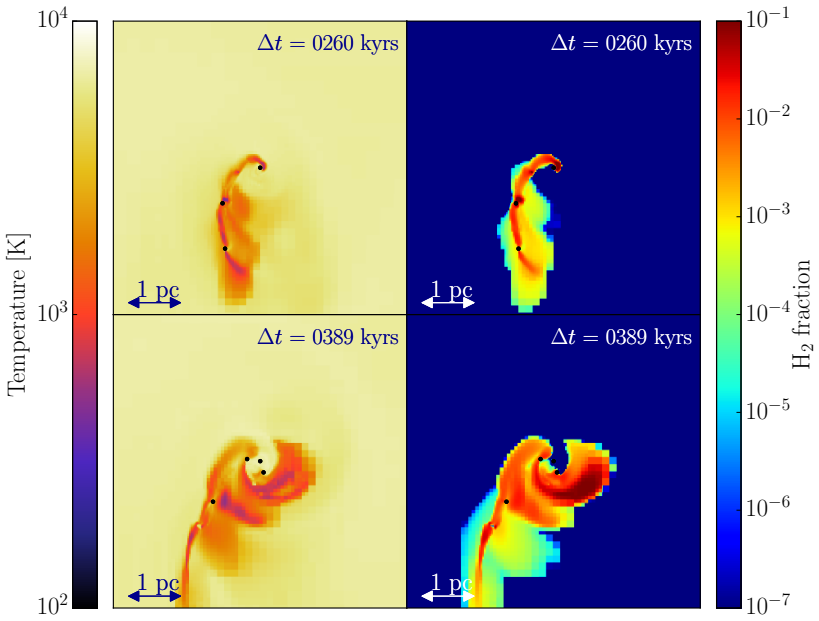

Figure 3.8: Temperature and H_2 fraction projections for halo C re-simulation irradiated by a UV background of $J_{21} = 10000$ at a scale of 5 pc. Temperatures are shown in the left, while H_2 fractions are represented in the right. Two epochs are shown, Δt represents the age of the simulation relative to the age of the first sink particle formed in the respective run.

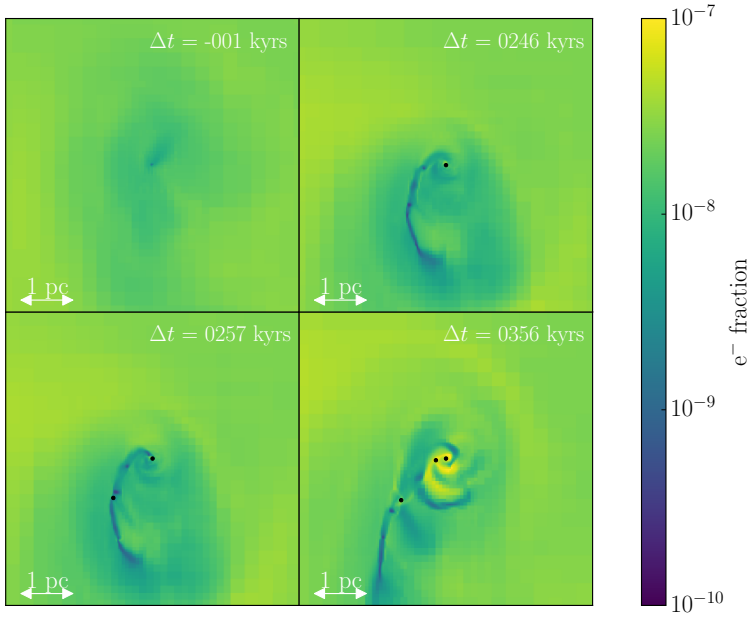

Figure 3.9: Electron fraction for halo C re-simulation irradiated by a UV background of $J_{21} = 10000$ at a scale of 5 pc. Two epochs are shown, Δt represents the age of the simulation relative to the age of the first sink particle formed in the respective run.

But there are some regions where most gas is being pushed away, which create gaps in mass infall rate profiles.

At some radii we can observe similar behaviors regardless of the halo, this is due to the fact that $\dot{M}(r)$ scales with r^2, ρ, and v_{infall}. At high radii, the area considered increases highly, but density and infall velocities are small compared to their values close to the center. On the other hand, the areas taken into account close to the center are small compared to the ones at high radii, but infall velocities are larger. At $\Delta t = 0$ kyr for all runs, density have the highest values in the center, which makes infall mass rates also have their highest values at these radii and time. When considering later times, density values close to the center decrease.

It is interesting to address the fact that mass infall rates are very high in halos A and B, having infall rates > 0.1 $M_\odot$ at different times with a few outflows in halo A. Halo C starts with accretion rates comparable to A and B, but at later times the formation of new sink particles and the interaction between them alters the infall mass rate, reducing the value and generating more outflows, this behavior is observed in the central 5 pc.

Sink particles

As mentioned previously, all black points in Figure 3.3 represent sink particles, which were allowed to accrete and interact with other elements in the simulation. Figure 3.10 shows the

time evolution for all sink particles in the $J_{21} = 10000$ runs. Mass and accretion rate time evolution are displayed: dashed gray lines represent the times that have been used to picture the projection plots (Figure 3.3) and to calculate the radial profiles (Figure 3.6). Each color represents a single sink particle, the time in the x-axis is the time relative to the first sink particle formed in the respective run. As mentioned in section 1.2.3, sink particles were allowed to merge each other. These events are represented with arrows in the mass profiles, they are bi-colored and start from the end of the mass profile of the least massive sink in the pair that is merging, and head to the new profile for the resulting sink particle. The color of the arrow's tail is the same as the one used for the least massive particle in the pair, while the head has the same color as the most massive sink particle. In mass and accretion rate profiles, the resulting new sink particle maintains the color used for the most massive sink particle in the pair.

It is clarified that accretion rates for all halos have been smoothed, in order to emphasize long-term variations and variations between sink particles. The smoothing has been performed by averaging the raw accretion rates value at a given time with its previous and next value (except by the extremes). The weights were 0.6 for the central one, and 0.2 for each neighbor. The accretion rates shown went through this process for 1000 iteration. This process erased all tiny variations in short time scales, which are associated with gas dynamics around the particles.

From Figure 3.10, we can see how sink particles evolve with time, observing a considerable increase in the masses of the sink particles. In halo A, the sink particle ends up with 8.7 $\times$ 10^4 $M_\odot$ near 300 kyrs after its formation. Accretion rate is kept above 0.1 $M_\odot$/yr during the run. Slight variations within this order of magnitude have been observed. For halo B a similar behavior is found compared to A; there is a huge increase in the mass of the sink particle, ending up with 2.2 $\times$ 10^5 $M_\odot$. In this case, the accretion rate is also kept over 0.1 $M_\odot$/yr but, unlike A, the accretion rate starts from a higher accretion rate $\sim$1 $M_\odot$/yr, due to the higher initial sink mass. Soon it decays slightly, but it maintains a value higher than 0.1 $M_\odot$/yr during the run. This sink particle reaches 10^5 $M_\odot$ in 161 kyrs after its formation.

In halo C five sink particles are formed. The first one forms in a similar environment compared to A and B; a spherical cloud collapses into a sink particle. However, several instabilities arise leading to the formation of a dense cold arm from which sink particles are created and fall to the center of the system. The first sink particle (red) formed accretes at a rate higher than $>$ 0.1 $M_\odot$/yr at the beginning. This value decreases quickly when more structures are formed, specially the cold arm from which sink particles are formed. All other sink particles formed also start with an accretion rate $>$ 0.1 $M_\odot$/yr which decreases quickly. Anyways, all accretion rates are kept over 10^{-2} $M_\odot$/yr during the run.

A remarkable result from the sink particle analysis is that we cannot observe a correlation between the growth time and the mass obtained by the sink particles. Table 3.3 shows that growth time has it lowest value for halo A, while halo B is more massive that halo A. This inconsistency relies in the fluctuations seen in the accretion rates.

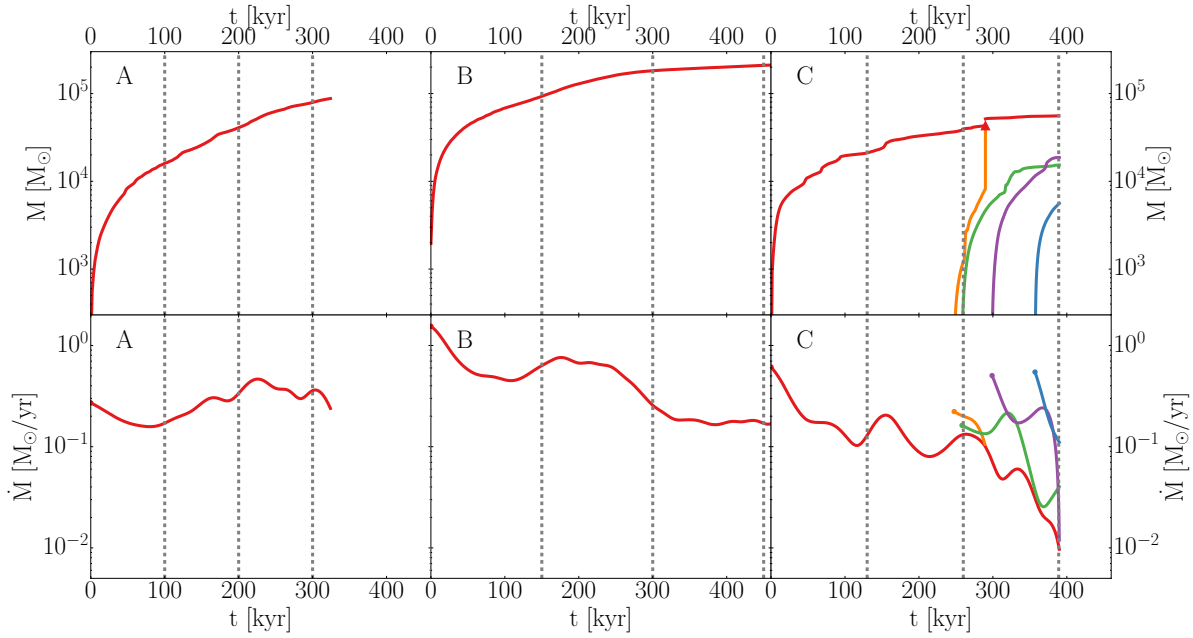

Figure 3.10: Mass and accretion rate time evolution for the $J_{21} = 10000$ runs. Halos A, B, and C go from left to right. Each color represents a single sink particle, the time in the 'x'-axis is the time relative to the first sink particle formed in the respective run. Arrows represent merger in the mass profiles, they are bi-colored and start from the end of the mass profile of the least massive sink in the pair that is merging, and head to the new profile for the resulting sink particle. The color of the arrow's tail is the same as the one used for the least massive particle in the pair, while the head has the same color as the most massive sink particle. In mass and accretion rate profiles, the resulting new sink particle maintains the color used for the most massive sink particle in the pair. Accretion rate evolution has been smoothed, in order to follow the long-term evolution.

3.0.2 Low UV intensity

In addition to the runs with $J_{21} = 10000$, simulations with $J_{21} = 10$ were also performed. Fragmentation and the formation of a larger number of sink particles are expected since at a low UV intensity molecular hydrogen does not dissociate, and its cooling is expected to overcome the atomic cooling.

Dynamics

I performed simulations for each halo using a uniform UV background of $J_{21} = 10$. Their evolution was followed for a larger period of time compared to the $J_{21} = 10000$ runs. They were followed by ∼3 Myr after the first sink particle formed in their respective run. In these simulations $t_{\rm growth}$ varies much more widely than in the $J_{21} = 10000$ case. In Figure 3.11 $t_{\rm growth}$ is illustrated as a function of time. For these cases, growth time remains at very large values compared to the 3 Myr simulated. Growth time averages 5.4 Myr for halo A, while it averages 9.1 Myr for halo B and 12.3 Myr for halo C. Though $t_{\rm growth}$ is much larger than the time-scale I could have gotten, 3 Myr were chosen since it is in time-scale of massive stars to explode, also it is in nuclear burning time-scale found by (Begelman, 2010), in case sink particles represent quasi-stars.

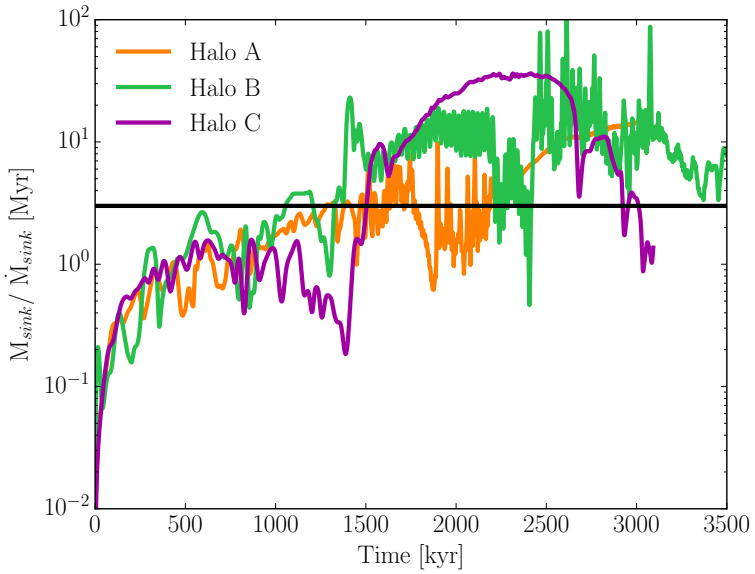

Figure 3.11: Growth time for the first particle formed in each simulation. The black horizontal line represents 3 Myr.

In Figures 3.12 and 3.13 gas density projections are displayed at various cosmic times. In these simulations more than one structure is formed, so the projection was made along the z-axis due to a lack of a preferred plane. Figure 3.12 represents the projection at a scale of 100 pc, while Figure 3.13 pictures it at a scale of 5 pc. The times shown in the plots (Δt) are snapshots relative to the first sink particle formation time in the respective simulations

(see Table 3.1). The Δt values were chosen based on spanning the dynamical evolution for the available outputs.

In Figure 3.12 projections are centered in the position of the first sink particle formed due to the lack of a reference as a consequence of the larger amount of structures. More structures are observed this time, compared to the $J_{21} = 10000$ runs at 100 pc. For halo A a disk is formed surrounding the sink particle by the time it forms. Later, a sort of double-disk forms, from which two central cores are identified. One of these cores contains the first sink particle formed in its center. In the neighborhood of this core, a second sink particle is formed by $\Delta t = 1.3$ Myrs. In the other clump, a third sink particle arises at $\Delta t = 2.1$ Myrs, residing in the clump center. For halo B, it is initially observed a central core embedded in a filamentary structure extended along the 100 pc shown in Figure 3.12. The filament fragments, as it can be seen as it approaches this core. New sink particles are created in these filaments. For halo C, a filament with a central structure is seen. By $\Delta t = 1$ Myr it has developed four cores, having sink particles been made up in these cores. Also, the three central cores seem to approach each other with time.

In Figure 3.13 a 5 pc scale zoom-in is portrayed from Figure 3.12. Every black dot represents a sink particle. Unlike the runs with $J_{21} = 10000$, this time the structures are so extended that information is lost from the whole halo by zooming-in. Halo A forms at the beginning a single structure within these 5 pc. Later, and as it was mentioned previously, another sink particle is formed in its surroundings, however, their interaction is not shown due to the time sampling used to make the figures. The second sink particle is formed at $\Delta t = 1.3$ Myr. By $\Delta t = 2$ Myr, both particles can be seen close to merging, they look overlapped, but are actually at a distance of 0.045 pc. They finally merge at $\Delta t = 2.2$ Myr. At $\Delta t = 2.8$ Myr the third sink particle is formed, which is localized in the center of one of the cores. By $\Delta t = 3$ Myrs, the central structure is observed with the resulting sink particle in its center, along with the approach of another dense region visible, which contains another sink particle in it. In Figure 3.12 such dense region can be also identified. When the simulation finishes, the two remaining sink particles are at distance of ~ 4.5 pc. In Figure 3.14 the distance of the sink particles residing in the two cores formed is shown, this distance is calculated at the time both particles are in the simulation. Close to ~ 2.8 Myrs an oscillatory motion is observed, but at later times their direct approach can be identified.

In Halo B the formation of a sink particle inside of a spherical shape structure at the beginning is appreciated. Later, this sphere becomes a disk-like structure with the sink particle in its center at $\Delta t = 1$ Myr. After that, a second sink particle is created in the disk surroundings at $\Delta t = 1.1$ Myr. This particle falls to the center, but instead of merging with the central one, it starts to orbit the other one forming a binary system. The binary remains stable, and a density gap between them arises (del Valle & Escala, 2014, 2015). Later, another sink particle is formed in the 5 pc region, created from a dense region that can be seen at $\Delta t = 2$ Myr approaching to the center. This sink particle falls to the center, merging with the least massive member of the binary. The resulting sink particle forms a new binary system with the left particle. By $\Delta t = 3$ Myr, we can see the interaction of this new binary. After the formation of the new binary mentioned previously, another sink particle is created in the surroundings at $\Delta t = 3.07$ Myr. This new particle plays a different role; instead of merging with one of the binary members, it forms a triple system. In Figure 3.15

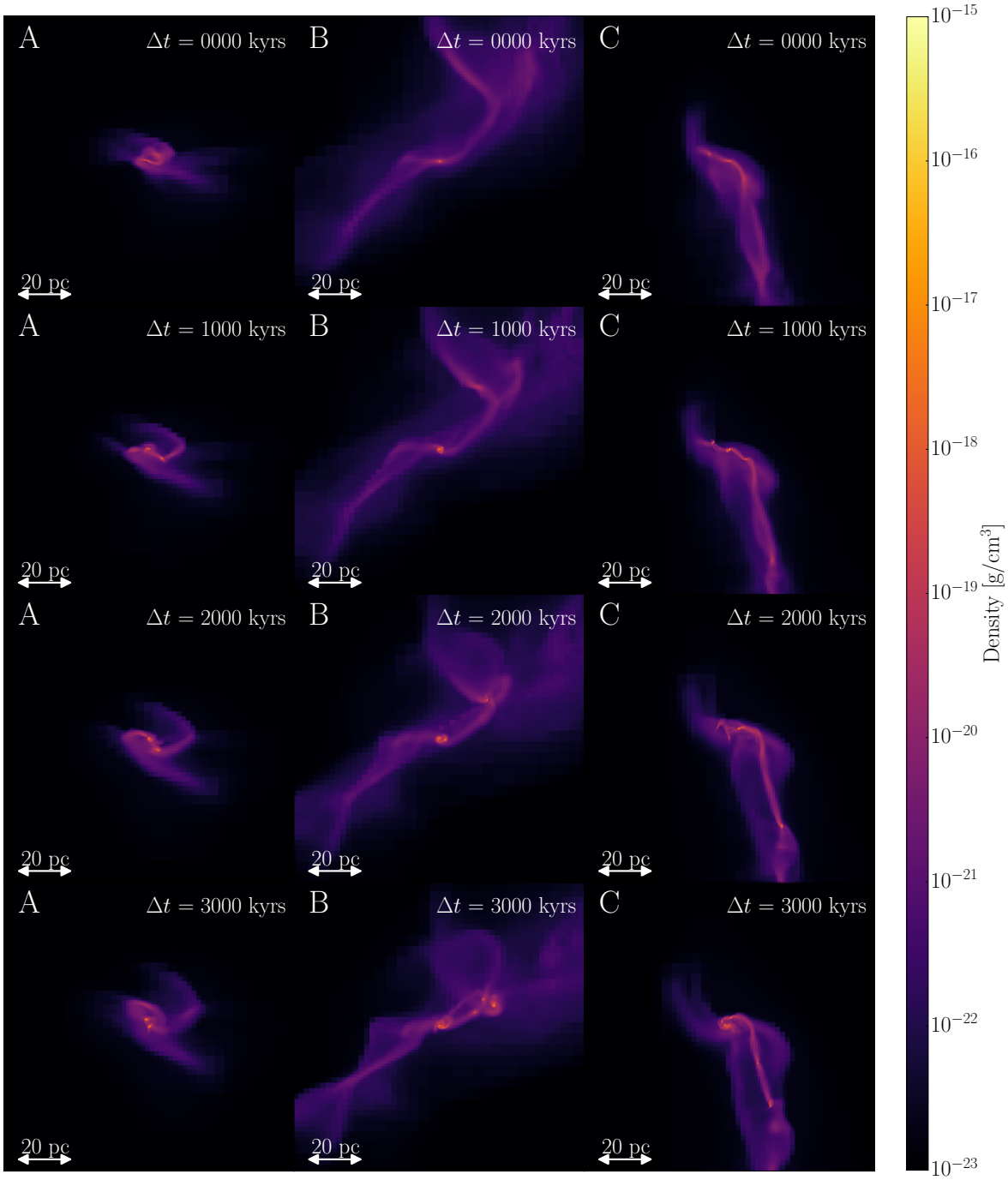

Figure 3.12: Density projection for all re-simulated halos irradiated by a UV background of $J_{21} = 10$ at a scale of 100 pc. Halos A, B and C go from left to right respectively. Two epochs are shown, Δt represents the age of the simulation relative to the age of the first sink particle formed in the respective run.

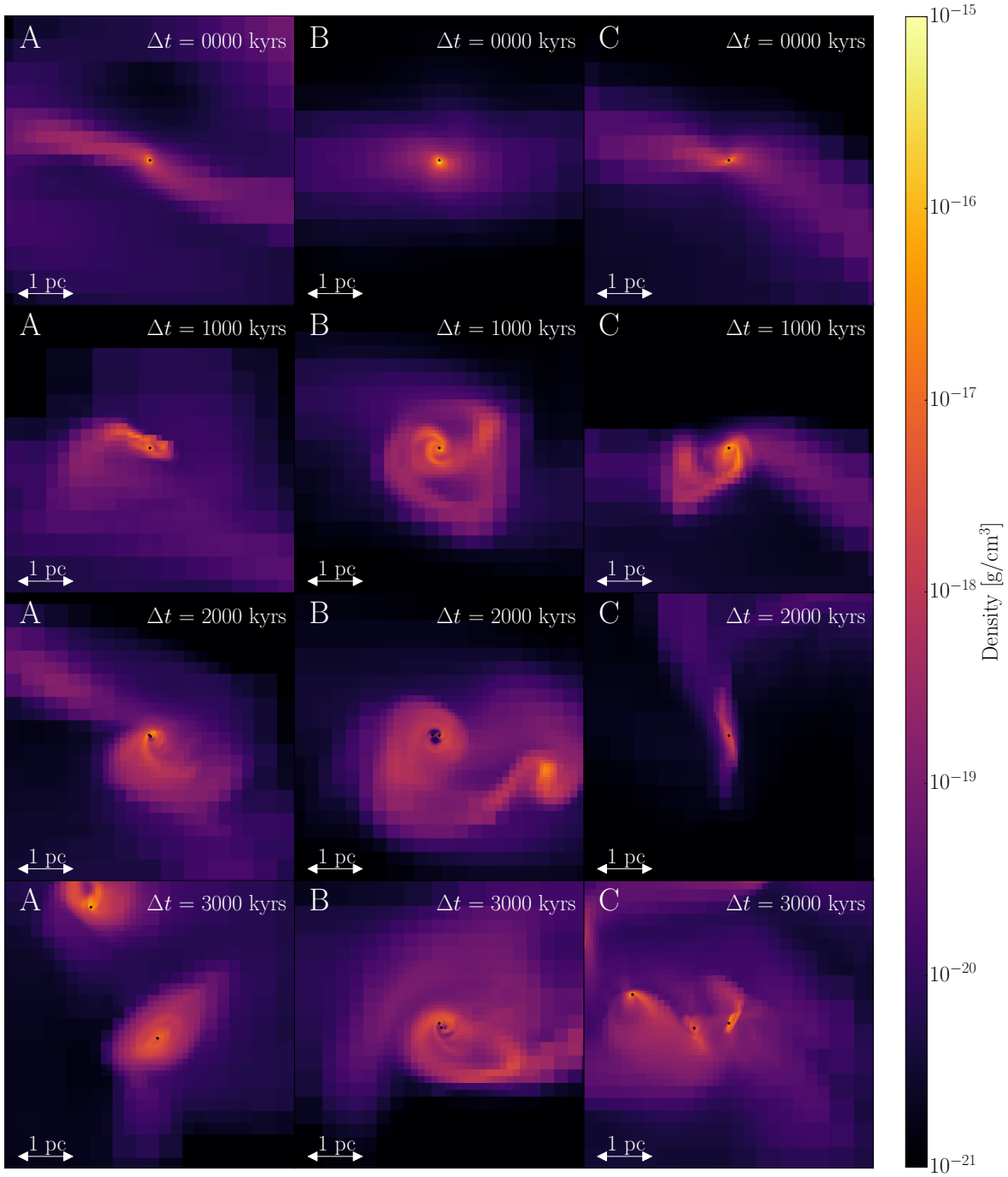

Figure 3.13: Density projection for all re-simulated halos irradiated by a UV background of $J_{21} = 10$ at a scale of 5 pc. Halos A, B and C go from left to right respectively. Several epochs are shown, Δt represents the age of the simulation relative to the age of the first sink particle formed in the respective run.

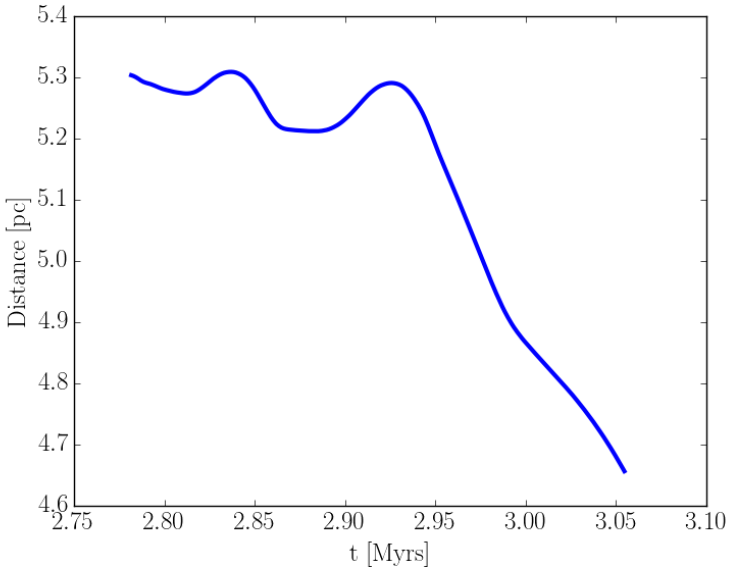

Figure 3.14: Distance as a function of time between the only two surviving sink particles in halo A close to the end of the run.

I show a later stage for this halo ($\Delta t = 3.35$ Myr), where we can see the approach of this sink particle just mentioned to the center. However, the three-body interaction soon leads to the merging of the previous binary, remaining again, in another binary system. In this run 8 sink particles are created, but they are so widely distributed, that not all of them are shown in Figure 3.13.

In Halo C a single filament, from which sink particles are formed, is observed. At $\Delta t = 0$ Myr we find the first sink particle embedded in a dense isolated region. At $\Delta t = 1$ Myr, we recognize this single particle to be in a disk. By this time, two other sink particles were already formed, but at distances too far to be included in Figure 3.13. One of these sink particles is 6.2 pc away from the first sink particle, while the other one is at 7.5 pc. Both particles were formed in the same filament observed in Figure 3.12. At $\Delta t = 2$ Myr, the first sink particle in the center is still isolated, but the disk is now seen edge-on. By this time, a fourth sink particle has been formed, but at a further distance of $\sim$35 pc from the first sink particle. At $\Delta t = 3$ Myr we observe three denser regions with sink particles within them approaching each other. One of them having experienced a gravitational pull that moved this particle away, to then come back to end up in the configuration shown. At $\Delta t = 3.08$ Myr two of them merge.

In Figure 3.16 sink particle distances to the most massive as a function of time are shown for halo B and C respectively. Every color represents a different sink particle. As can be seen, three sink particles in halo B do interact with the most massive one, forming an oscillating system, from which two (blue and purple) eventually merge. Four remain far from the most massive sink particle. For halo C, it is seen that all sink particles move towards the most massive sink particle during the run, from which two of them reach the oscillatory regime (blue and green).

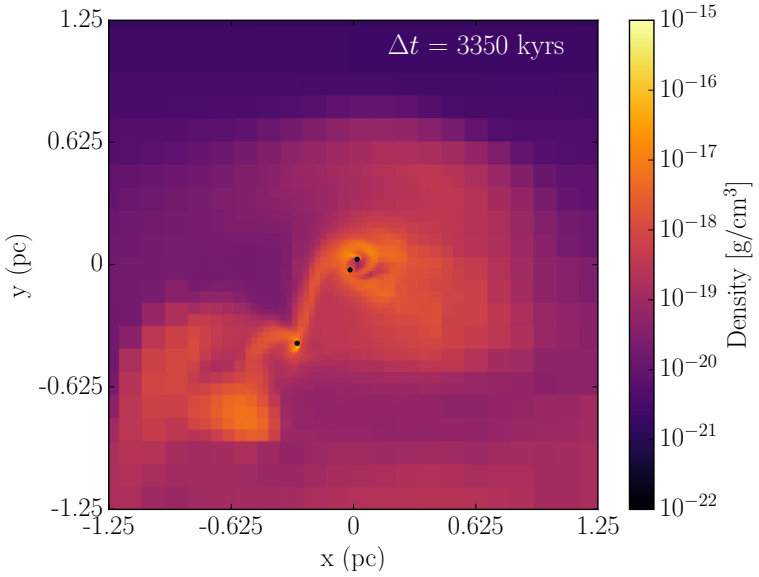

Figure 3.15: Density projection for the central 2.5 pc in halo B. The projection has been made along the z-axis. Black dots represent sink particles. This projection has been made at $\Delta t = 3.35$ Myrs after the formation of the first sink particle in this run.

Radial profiles

In addition to the density projections, I show radial profiles for these simulations in Figure 3.17. I include density, temperature, H_2 fraction and mass infall rate. The profiles are also plotted for the same Δt I have used in Figures 3.12 and 3.13. All the plots are centered in the first sink particle formed, and they span from resolution scales $\sim 10^{-2}$ pc up to 1 kpc in order to sample the whole halo. Virial radii range from 0.8 up to 1.1 kpc at the end of the run. They are smaller compared to the $J_{21} = 10000$ runs since gravitational collapse occurs at a later cosmic age.

All density profiles exhibit a nearly isothermal profile $\rho \propto r^{-2}$ (gray dashed line) with some deviations. For all halos, there are some peaks in the profiles that represent overdense regions away from the chosen center, some of which host sink particles. In all cases, we can observe a decrease in central density with time, what is due to gas accretion in the central sink particle's neighborhood.

In Halo A we can visually identify a binary system from the Dynamics Section, with one of the components being the center of its radial profile. The other component of the binary is observed as peaks in density, which vary in position at different times. The position of the peaks ranges from 4 to 7 pc, which is due to the oscillating approach between both regions. See also Figure 3.14.

In Halo B some peaks relative to the isothermal profile are observed. They represent overdense regions as seen in Figure 3.12. At $\Delta t = 0$ Myr, we can see a small increase in density at ~ 30 pc, which has increased by $\Delta t = 1$ Myr. At $\Delta t = 2$ Myr, we can appreciate the same peak with a much higher value: this is caused by the collapse of that region. As

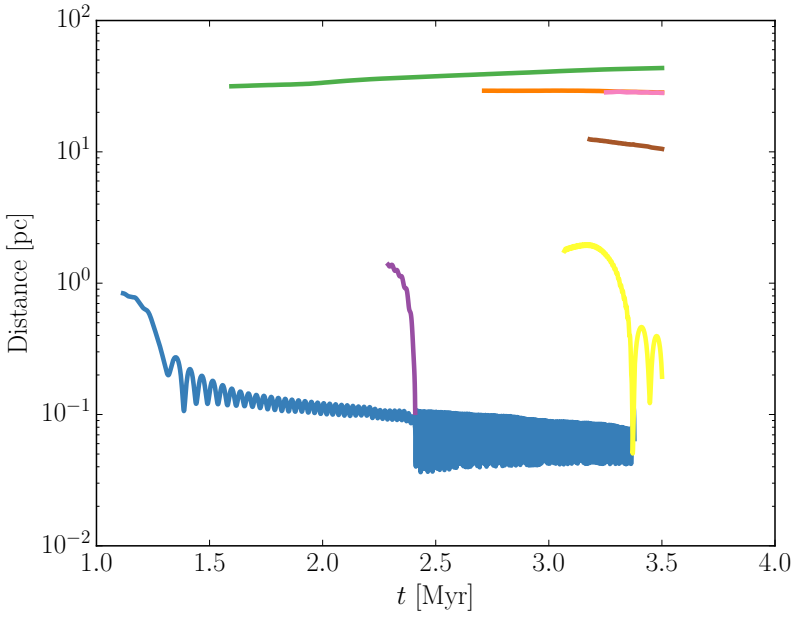

(a)

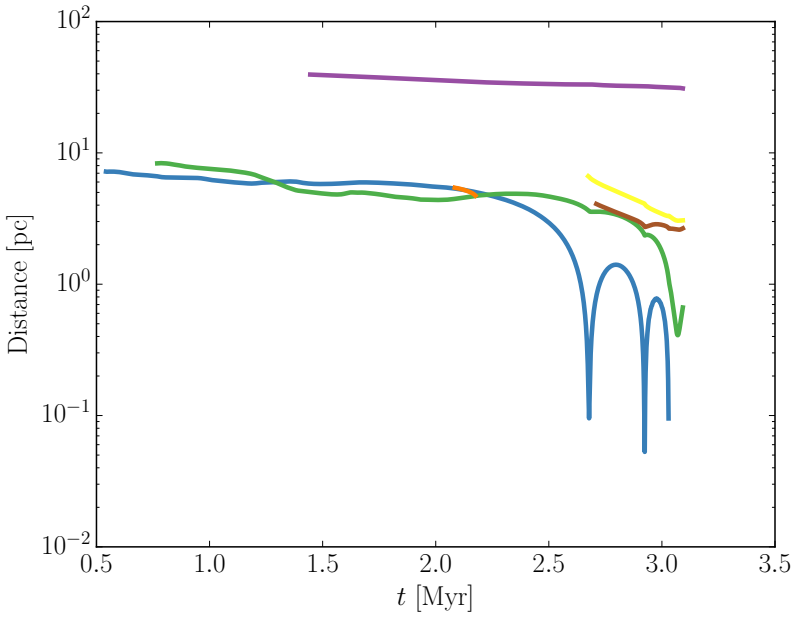

(b)

Figure 3.16: Sink particle distances to the most massive as a function of time for halo B (a) and halo C (b). Every color represents a different sink particle formed at a later age than the most massive one.

a consequence of fragmentation, more dense regions are formed. Three peaks are identified between 10 and 30 pc at $\Delta t = 3$ Myr. All density peaks observed in the density profile can be identified in Figure 3.12.

In Halo C, similarities to Halo B are found in terms of the formation of collapsing structures away from the center. These structures are seen in Figure 3.12 and are also identified by looking at peaks in the density profiles. At $\Delta t = 0$ Myr we observe two slight overdensities at $\sim$8 pc and at $\sim$41 pc. These are identified as regions that will collapse to form denser structures and sink particles. At $\Delta t = 1$ Myr we identify three peaks, two of which are at $\sim$6.5 pc and $\sim$44.5 pc, resembling the slight overdensities mentioned above. Also, a new overdensity is observed at $\sim$14 pc. By $\Delta t = 2$ Myr, density peaks have been displaced to 4.4, 7.0 and 38.2 pc, where sink particles have formed by this epoch.

Temperature varies more widely than in the $J_{21} = 10000$ case. For the three halos, we observe that temperature value is kept higher than 5000 K at distances higher than $\sim$ 100 pc from the center. This phenomenon tells us about the distance at which interactions and fragmentation are enclosed. Inside this region, gas cools down. For the three runs we observe that, as time goes on, central temperature rises. This is due to dynamical interactions between the central sink particle and its surroundings.

The H_2 fraction profile shows a similar behavior compared to temperature profiles for all halos. It shows a decrease in its value starting from a given distance. This decay leads to an increase in temperature. Usually, H_2 fraction and temperature behaviors are related: high H_2 concentrations cool down the system to low temperatures, and high temperatures lead to a lack of enough coolants. We appreciate such trend even at small radii for halo A. However, we do not observe such correlation in the central regions of halos B and C. As mentioned in section 3.0.2, halo B turns to form a central disk with sink particles orbiting each other in the center forming a binary system. The dynamical interaction between this binary and gas results into gas heating, which is compatible with high concentrations of molecular hydrogen and high temperatures. Halo C shows a similar behavior to B in terms of temperature and H_2 fraction. Though halo C does not form a tight structure compared to halo B, their sink particles do interact with each other heating up gas.

In addition to density, temperature, and H_2 fraction, I also added mass infall rates to radial profiles. Mass infall rates were calculated using the same procedure described in Section 3.0.1; Radial profiles subsection.

In all of our runs we observe regions in which gas is falling down to the center, and regions where the gas is moving away. At most radii, infall mass rate calculations turn out to be positive, implying that most gas is being accreted compared to gas being pushed away. But there are some regions where most gas is being pushed away, which create gaps in mass infall rate profiles. In halo A, we can observe the largest mass infall rate values at $\Delta t = 0$ in the center. At $\Delta t = 1$ Myr and $\Delta t = 2$ Myr we observe a decrease in the mass infall rate in the center, where gas has been accreted by the central sink particle. By $\Delta t = 3$ Myr, we can see the infall mass rate increasing with radii, which is due to the area used to made the calculation, with the exception of a peak between 4 and 5 pc. This peak corresponds to the radius where another sink particle and its accretion region are located.

Halo B shows the behavior explained for halo A at $\Delta t = 0$ Myr, with the exception of a gap around ~ 10 pc. At later times this value has decreased like all other cases. However, all interactions between sink particles and the formation of several consecutive binaries (see Section 3.0.2) lowers this value and more gaps appear since gas in being pushed away.

In halo C at $\Delta t = 3$ Myrs, we observe a similar behavior compared to halo A. In this halo infall mass rates increase with radii showing some enhancement between 1 and 20 pc, which is due to the approach of 3 sink particles.

Sink Particles

In Figure 3.13 every single sink particle is represented with a black dot, but they do not represent the total number, since sink particles are distributed wider than the 5 pc shown in that figure. In Figure 3.18 I present time evolution for all sink particles created. Mass and accretion rate time evolution are portrayed: dashed gray lines represent the times that have been used to picture the projection plots (Figures 3.12 and 3.13) and to calculate the radial profiles (Figure 3.17). Each color represents a single sink particle, the time in the x-axis is the time relative to the first sink particle formed in the respective run. Arrows represent merging particles in mass profiles, and accretion profiles have been smoothed for easy reading. Details of both procedures are in Section 3.0.1; Sink particles subsection.

In Figure 3.18 we can see how sink particles change with time. Their masses increase naturally, reaching values over 10^3 $M_\odot$. The most massive ones get masses over 10^4 $M_\odot$. I emphasize that these sink particles take more time to reach a significant amount of mass compared to the $J_{21} = 10000$ case, where they take hundreds of kyrs to do it. All sink particles start with accretion rates ~ 0.1 $M_\odot$/yr, whose value decays at least one order of magnitude in all cases. As fragmentation raises in these runs, regions where sink particles are created do not contain enough gas to reach initial accretion rate values compared to the $J_{21} = 10000$ runs. We can also observe a rapid decrease in accretion rates with time, which is mainly due to the fact that gas has been accreted. For halo A I recall that two main cores are formed with sink particles in their centers, one of these cores merges with another sink particle that is formed in its surroundings. Previous to its corresponding merger, both sink particles form a binary system. When both members of the binary approach, accretion rates for both sink particles are enhanced by a small amount. After the merger, this value decreases. For halo B, we can identify a succession of binaries and sink particle mergers. The participants are represented in Figure 3.18 in blue, red, purple, and yellow. Every time a merger happens, gravitational interactions push gas to sink particles increasing their accretion rates. Unlike isolated sink particles, we can observe accretion rates to experience oscillations in those cases. In Section 3.0.4 I show some accretion rates with no application of the smoothing technique in the binaries regime for halos A and B.

In halo C, the situation is completely different than in the previous cases, mainly due to the fact that sink particles are spread over 100 pc, which limit the interactions between them. Though the interactions are not comparable to the previous cases, we can observe a merger between two sink particles (green and orange lines in Figure 3.18). Unlike other mergers, we cannot appreciate oscillations in its accretion rate, since they skip the binary phase, merging

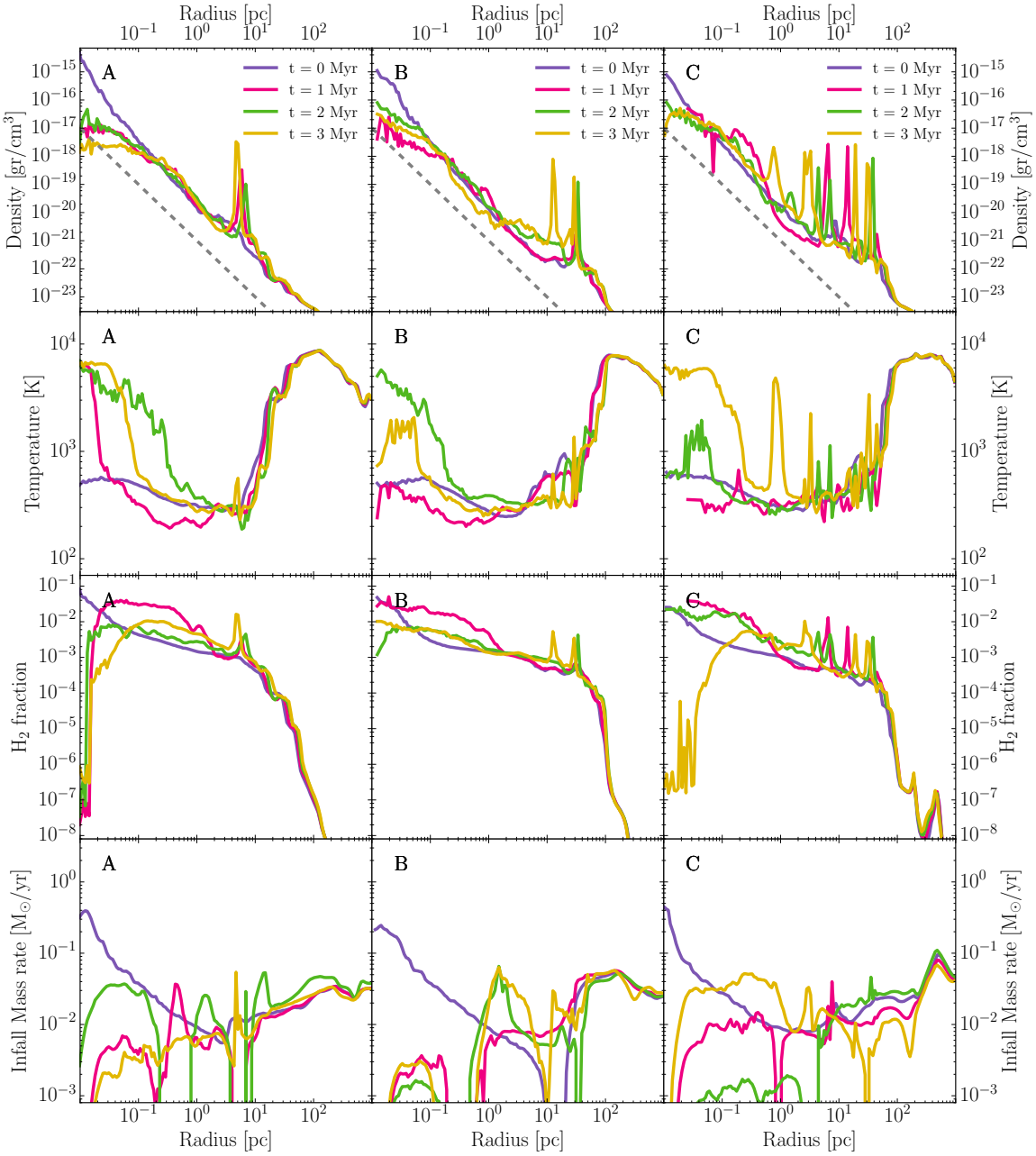

Figure 3.17: Radial profiles for the $J_{21} = 10$ runs. They include density, temperature, H_2 fraction and infall mass rate. Halos A, B and C go from left to right respectively. The profiles are calculated at the same times (Δt) shown in Fig. 3.12. In density profiles, we plot a dashed gray line that represents an isothermal profile $\rho \propto r^{-2}$.

directly. At the end of the run some sink particles approach to the first sink particle formed, though they do not merge, some little enhancements are produced in the accretion rates of the approaching particles, as can be seen in blue, red and purple lines in Figure 3.18.

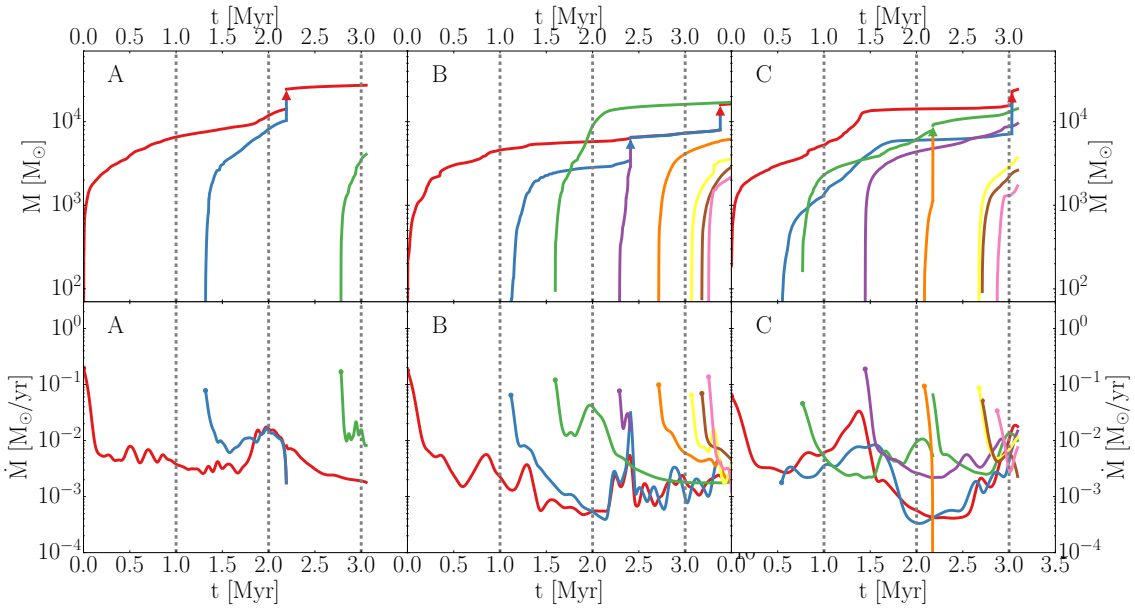

Figure 3.18: Mass and accretion rate time evolution for the $J_{21} = 10$ runs. Halos A, B, and C go from left to right. Each color represents a single sink particle, the time in the 'x'-axis is the time relative to the first sink particle formed in the respective run. Arrows represent merger in the mass profiles, they are bi-colored and start from the end of the mass profile of the least massive sink in the pair that is merging, and head to the new profile for the resulting sink particle. The color of the arrow's tail is the same as the one used for the least massive particle in the pair, while the head has the same color as the most massive sink particle. In mass and accretion rate profiles, the resulting new sink particle maintains the color used for the most massive sink particle in the pair. Accretion rate evolution has been smoothed, in order to follow the long-term evolution.

3.0.3 Extended UV intensity cases

In addition to the runs showed in Section 3, simulations for values of $J_{21} = 100$ and $J_{21} = 5$ were performed. There are no significant differences compared to the cases studied in the previous sections of this chapter, in this sense they are still presented for completeness.

In Figure 3.19 we can see density projections for halos A, B and C at scales of 3 kpc for the top panels, and at scale of 100 pc for the bottom ones in the re-simulations performed under the presence of a intermediate UV background ($J_{21} = 100$). In all cases just one sink particle is formed. In these runs, sink particle masses range between the ones gotten in the $J_{21} = 10000$ and $J_{21} = 10$ cases. In addition, gas distribution remains mainly central. Though all halos show some asymmetries, fragmentation and the formation of more than one sink particle is not observed in the time period the simulation was run. The formation of

the only sink particle happened at a redshift of 12.06, 10.80, 11.77 for halos A, B, and C, respectively. These values are in between the redshifts where the collapse was triggered for $J_{21} = 10000$ and $J_{21} = 10$. These intermediate results in mass and redshift show that the formation and evolution of sink particles is related with gas thermal evolution, therefore, UV radiation has an impact on it.

The most relevant difference is that halo C does not fragment nor produce more than one sink particle during the run (~ 1 Myr), which seems inconsistent with the fragmentation observed under the presence of a stronger UV flux (Section 3.0.1). However, such inconsistency makes sense when we look at the redshifts at which the sink particles form and the merger trees (Figure 2.4). At $z = 10.80$ the halo has suffered of a merger episode with another halo with a similar amount of mass, while at $z = 11.77$ the halo was close to that merger episode, but it has not happened yet. This phenomenon reveals again the importance of dynamics and the environment in which interactions are happening.

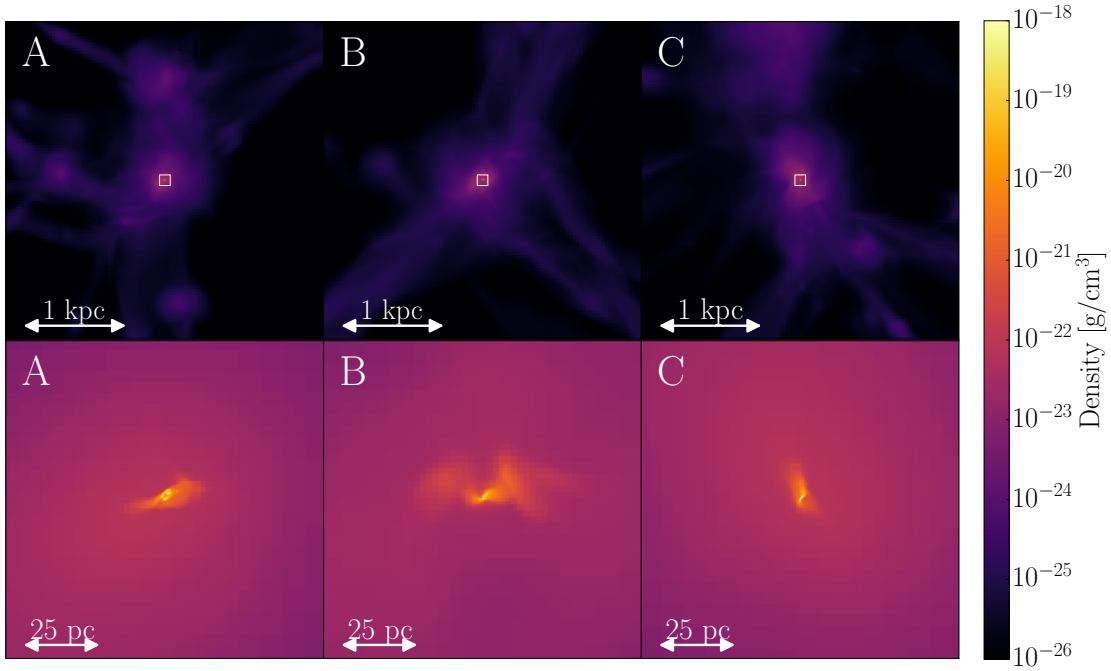

Figure 3.19: Density projection for re-simulated halos A, B, and C irradiated by a UV background of $J_{21} = 100$. The projections are made at the time the first sink particle is formed in the respective simulation. Halos A, B and C go from left to right respectively. At the top, projections correspond to 3 kpc, where white squares correspond to 100 pc regions, which are shown at the bottom.

In addition to the re-simulations under the presence of a UV flux with a $J_{21} = 100$, I also performed one re-simulation for halo B under the influence of a $J_{21} = 5$ UV background. I picked halo B, since various interactions between the sink particles formed are observed in its $J_{21} = 10$ run. This run includes deuteride species and their associated reactions, which are shown in Section 1.2.1. Although halo C seems to be the most promising halo to be re-

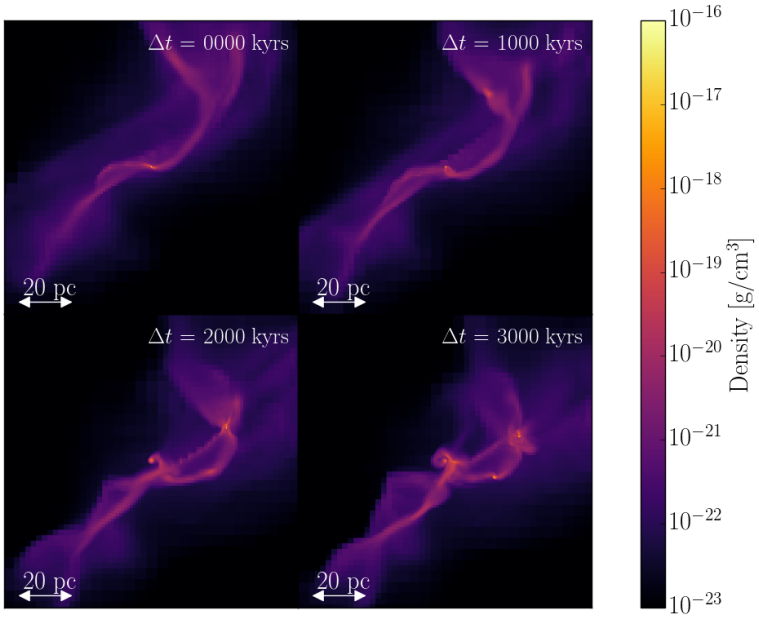

Figure 3.20: Density projections for the re-simulation of halo B under the influence of a uniform UV background of $J_{21} = 5$ that includes deuteride chemistry.

simulated, its $J_{21} = 100$ run reveals that sink formation precede a merger, event that triggers some fragmentation.

In Figure 3.20 we can see different density projections of halo B in the setup mentioned above, the structure in this run is too similar to the re-simulation of halo B, the filamentary structure is distributed similarly. In this run 9 sink particles are created, and two merger episodes are observed. All surviving sink particles end up with masses between 10^3 and 10^4 $M_\odot$.

3.0.4 Accretion Rates

In Section 3.0.2 accretion rates for halos A and B were revised. In Figure 3.18 a smoothing technique was applied to better visualize the differences between sink particles and to focus in the long-term variations. By doing this, I lose relevant information about time variations in their accretion rates due to gravitational interactions between sink particles. For instance, Goicovic et al. (2016) showed that for black hole binaries accretion rates oscillates with the rotation timescale of the system.

In Figure 3.21 accretion rate evolution is shown, ranging between $\Delta t = 1.7$ Myr and 2.1 Myr for halo A (relative to the first sink particle formed in the run). No smoothing technique has been applied, so we can appreciate raw values for accretion rates. A non-periodic oscillatory behavior is seen, that becomes more frequent with time due to the particles approaching.

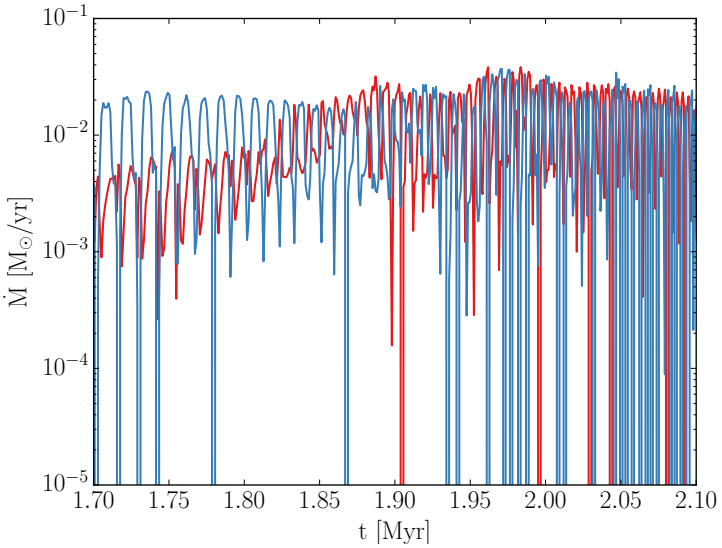

Figure 3.21: Accretion rate time evolution for halo A with no smoothing. Every color represents a sink particle, they are the same used for halo A in Figure 3.18.

Extreme variations are also observed, since the values oscillate between values $< 10^{-5}$ $M_\odot$/yr and $> 10^{-2}$ $M_\odot$/yr, specially for the least massive member of the binary (blue).

In Figure 3.22 we can observe accretion rates for halo B. Time ranges between $\Delta t = 1.8$ Myr and 3.0 Myr (relative to the first sink particle formed in the run). Similarly to halo A, we observe an oscillatory behavior. Unlike halo A, we see three *phases*, one from $\Delta t \leq 1.8$ to 2.2 Myrs, another from Δt =2.2 to 2.4 Myrs and a third one from Δt =2.4 to >3.0 Myrs. The first phase is related to the binary interaction between both members in the group. The behavior is similar to halo A, since there are only two particles interacting. The second *phase* is related to the approach of a dense region that forms a sink particle (purple line in Figure 3.18), which slightly enhances accretion rates by a little. It is interesting to note that this change in accretion rate begins before a sink particle is created, which merges with one of the binary members. Finally, a third regime is appreciated, which starts after the merger between the sink particles portrayed, with purple and blue in Figure 3.18. This regime is quite similar to the first one, since there are two sink particles interacting. However, as the mass of one of the members has increased substantially, accretion rate oscillations become more frequent and amplitudes are larger, having certain moments when accretion rates are below 10^{-5} $M_\odot$/yr for both members. There is a fourth regime, that happens when both members of the binary finally merge due to gravitational kicks produced by another sink particle (Yellow color in Figure 3.18). This fourth regime is not shown in Figure 3.22.

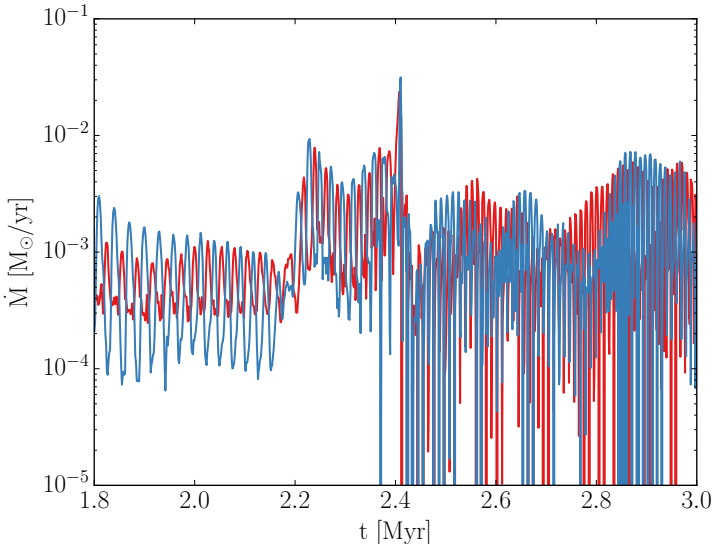

Figure 3.22: Accretion rate time evolution for halo B with no smoothing. Every color represents a sink particle, they are the same used for halo B in Figure 3.18.

Chapter 4

Discussion

In this thesis, the formation of supermassive black hole seeds has been studied including the role of fragmentation processes. The Direct Collapse Black Hole (DCBH) scenario seems very efficient forming massive seeds ($> 10^5$ $M_\odot$), which become massive black holes when the General Relativistic (GR) instability (Chandrasekhar, 1964) is triggered. Such black holes may end up in the center of the high redshift quasars observed. However, it demands several strong restrictions in order to fulfill its assumptions. Between these restrictions, gas fragmentation is a process not allowed, since it contradicts the aim of forming a central single massive structure.

I performed simulations in order to explore how gas behaves under different conditions, those include: dark matter host halo spin, dark matter halo merger history and UV intensity. Two of three re-simulated halos under the presence of a high UV intensity ($J_{21} = 10000$), namely A and B, replicate very well the DCBH scenario. They correspond to the halos with the lowest spin parameters, and also to halos formed out of a small number of mergers. These two features, i.e. halo spin parameter and merger history seems to be relevant for the formation of SMBH seed. These halos resemble the results reported in other works (Latif et al., 2013a,b), in which a central core is formed without any fragmentation.

In these simulations, just one sink particle is formed in each simulation during the whole run. The radial profiles for them support the formation of a central massive structure: density profiles follow nearly an isothermal profile, with a central decrease at later times, which is just the consequence of sink particle accretion. Temperature profile also resembles an isothermal profile, as an almost horizontal line with a small slope. At the same time the H_2 fraction profiles show some localized enhancement, however the fractions are not high enough to change drastically the temperature. Just a tiny drop in temperature at a radius of $\sim 2 \times 10^{-2}$ pc is seen. H_2-density and temperature-density diagrams reveal a transition between two phases, which are identified at a H_2 fraction about $\sim 10^{-4}$ and 10^{-3}, indicating that at those fractions the its abundance is relevant enough to produce molecular cooling. In addition to radial profiles, the evolution in mass and accretion rate for the single sink particle formed in halos A and B is followed. The initial mass of sink particles in halos A and B is 132 $M_\odot$ and 518 $M_\odot$ respectively, and their accretion rates are kept > 0.1 $M_\odot$/yr during the whole run, both sink particles end with 8.8×10^4 $M_\odot$ and 2.2×10^5 $M_\odot$ in halos A

and B respectively, which is a significant value for a seed.

On the other hand, in the re-simulation for halo C a different behavior is observed. It is recalled that halo C is the dark matter halo with the highest spin parameter from the ones chosen and formed out the interaction of a considerable amount of mergers. This halo starts in a similar fashion to A and B, however, as the simulation goes on, fragmentation processes appear in the central 5 pc, which is seen as a disk-like structure with a spiral arm from which sink particles are formed. Sink particles formed in this case are still massive enough with values close or higher than 10^4 $M_\odot$. One sink merger is observed, and according to the behaviour of the sink particles all could end up merging. In such a case, the final mass would be higher than 9.5×10^4 $M_\odot$. One of the most interesting phenomenon of this run, is the high concentration of molecular hydrogen as can be seen in the radial profiles and H_2 fraction projection for this. In addition to the analysis mentioned above, a Toomre parameter examination shows that the formation of sink particles is triggered by local instabilities.

In addition, three re-simulations were performed for halos A, B, and C under the presence of a weak UV background ($J_{21} = 10$). The evolution of these structures is much more different than in the other cases since fragmentation is observed, and at larger scales. Halo A is an interesting case, fragmentation is observed in the central 20 pc, and it is kept at that scale during the whole run. In this case two sink particles are formed in two core regions, they evolve independently to get bound at the end of the run, but not merging. Their masses by time the runs finish are 2×10^4 $M_\odot$ and 4×10^3 $M_\odot$. In halo B and C the fragmentation process is seen extended in 100 pc, the number of sink particles is the largest for all the simulations performed being 8 and 7 for halos B and C respectively. Also, in both halos the mass of the sink particles is higher than 10^3 $M_\odot$ at the end of the runs. An important fact is that sink particles approach to the most massive one with time, a few interactions and mergers are seen. An interesting fact of these simulations is that in all of them, the first sink particless reaches similar masses, being close to 10^4 $M_\odot$, while the ones formed at later times keep $\sim 10^3$ $M_\odot$ as can be seen in the sink evolutionary profiles.

Additionally, some UV extended cases were performed to study all possible differences. However, there are no major differences between them and the already performed simulations at high or low UV intensity, with the exception of one astonishing case. It is observed that halo C fragments at $J_{21} = 10000$ forming 5 sink particles, but it does not at $J_{21} = 100$ just forming one sink particle. This behaviour agrees with the fact that collapse happens at different times, being at $J_{21} = 10000$ the lowest redshift (i.e. highest cosmic time), being more vulnerable to interaction for a larger period of time. This event reveals the importance of a halo story in the feasibility in the fragmentation and the formation of a massive seed.

Several works have tried to find the critical UV intensity value ($J_{21}^{\rm crit}$) at which a DCBH can take place. Figure 4.1 shows a summary made by Latif et al. (2015) identifying different methods to estimate this value. They performed performed 3D cosmological simulations. As can be seen, the results differ by several orders of magnitude between 3D cosmological simulations and one-zone models. One-zone models solve the hydrodynamical equations in a small volume element without considering its spatial extent, they are performed to prioritize the thermal evolution of gas, therefore, they turn to be much cheaper computationally. On the side of these models, Glover (2015) have claimed that J_{21}^{crit} depends strongly in the set

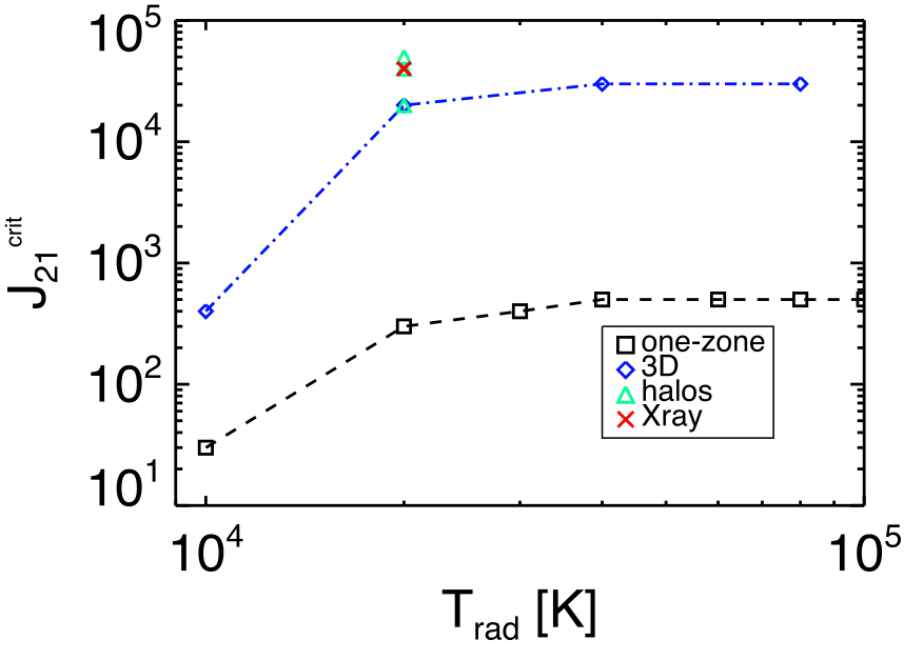

Figure 4.1: Critical UV intensity as a function of radiative spectra temperature. It contains data from 3D simulations, one-zone models. Image from Latif et al. (2015).

of chemical reactions, and he performed a set of relevant chemical reactions required to find J_{21}^{crit} to allow a DCBH scenario. Finally, from my results, J_{21}^{crit} seems to be a parameter very tight to the dynamics in a particular system rather than anything else. It seems that it is not possible to parameterize the phenomenon with the J_{21} parameter only, and the dynamic of the system plays a key role in the formation of SMBH seeds.

One of the caveats of the simulations performed is that they do not include radiative feedback in their implementation. It is known that stars radiate photons, supporting gas from being accreted into a black hole seed. Hosokawa et al. (2012, 2013) studied the evolution of rapid accreting supermassive stars (SMS). They found that accreting SMS at rates higher than > 0.1 $M_\odot$/yr evolve as supergiant stars, in which relativistic instability is triggered when they reach masses $\sim 10^5$ $M_\odot$, also they found that ionizing radiation is unlikely to operate. These findings are compatible with the analytical results found by Schleicher et al. (2013). More recently, Haemmerlé et al. (2018) studied accreting protostellar evolutionary models in a similar way to the previous works mentioned obtaining similar results. In their work, most massive stars evolve as red and cold supergiant stars, while the less massive ones evolve towards the ZAMS as blue and hot stars. They reduced the critical accretion rate at which ionizing radiation becomes negligible down to 0.005 $M_\odot$/yr. In addition, Chon et al. (2018) performed radiative hydrodynamical cosmological simulations to study the effect of radiation in the growing of the SMS, finding no major role in radiative feedback.

Requirements to keep radiation unimportant according to the conditions mentioned in the works above are met in all the simulations performed at high UV intensity. Though halo C fragments, all sink particles formed in this simulation meet the minimum accretion rate requirement and the masses to trigger the GR instability.

From an observational point of view, Pacucci et al. (2016) devised a method to identify supermassive black hole seed candidates, based on the spectra of radiative hydrodynamic simulations in the DCBH scenario. They claimed findings of two possible candidates, using infrared and X-ray photometry. James Webb Space Telescope is alleged to be a key instrument to obtain spectra from these objects unveiling clues in the understanding of the mechanism to form SMBHs. The recent detection of gravitational waves from the merging of a BH binary by LIGO (Abbott et al., 2016) has opened a new area of study. If sink particles formed are considered relativistic objects, their interaction would emit detectable gravitational waves . Gravitational Waves (GW) were speculated by Rees (1978) in this context. Pacucci et al. (2015a) showed that the gravitational signal in the context of an asymmetric collapse (Shapiro, 2003) lies above the foreseen sensitivity of the Ultimate-DECIGO observatory in the frequency range (0.8–300) mHz,

Considering the caveats in the simulations performed in this work, some factors need to be taken into account for future work. Radiative transfer calculations and more resolution should be required in new simulations. The physical meaning of the structure represented by the sink particle is still open, since the smallest scales are not yet fully understood. Stellar models following the evolution of supermassive Population III protostars have been studied in case the smallest structures may turn into them.

Conclusion

The main findings of this work are summarized in the following points:

- Dynamics is one the most important factors determining the feasibility in the formation of a massive object. The rotation of a dark matter halo hosting a proto-galaxy and its merger history help us to understand what kind of dynamical interactions we will deal with.
- There is no uniqueness in the strength of the UV intensity value required to achieve a DCBH, since it depends in other factors like the system dynamics.
- Local gravitational instabilities trigger the formation of sink particles in the simulations presented.
- There seems to be a correlation between the final mass of the sink particles and the UV intensity, which can be understood as the consequence of the increase in the Jeans mass due to the increase in temperature depending in the strength of the radiation.
- There is no correlation observed between the amount of sink particles formed and the strength of the UV radiation.
- A clear correlation is observed in the timescales that structures need to evolve and the UV intensity. For high UV intensities such a timescale takes $\sim$ 300 kyr - 500 kyr, while for low UV intensity it is $\sim$3 Myr.
- The first sink particle being formed is always the most massive one.
- Regardless of the dynamics and the intensity in the UV background, all sink particles reach masses over 10^3 $M_\odot$ at the end of run.
- In most cases the accretion rate of all sink particles at the time of their creation was very high (> 0.1 $M_\odot$), but it soon decreases due to a lack of gas.
- Fragmentation influences the mass acquired for the sink particles, but it does not avoid them from merging. In all simulation ended up with many sink particles, they all approach to most massive one with time.

Bibliography

Abbott B. P., et al., 2016, Physical Review Letters, 116, 061102

Abel T., Anninos P., Zhang Y., Norman M. L., 1997, New A, 2, 181

Abel T., Bryan G. L., Norman M. L., 2000, ApJ, 540, 39

Abel T., Bryan G. L., Norman M. L., 2002, Science, 295, 93

Aldrovandi S. M. V., Pequignot D., 1973, A&A, 25, 137

Alvarez M. A., Wise J. H., Abel T., 2009, ApJ, 701, L133

Bañados E., et al., 2018, Nature, 553, 473

Barkana R., Loeb A., 2001, Phys. Rep., 349, 125

Bate M. R., Bonnell I. A., Price N. M., 1995, MNRAS, 277, 362

Begelman M. C., 2010, MNRAS, 402, 673

Bennett C. L., et al., 1996, ApJ, 464, L1

Birdsall C. K., Fuss D., 1969, Journal of Computational Physics, 3, 494

Bleuler A., Teyssier R., 2014, MNRAS, 445, 4015

Boekholt T. C. N., Schleicher D. R. G., Fellhauer M., Klessen R. S., Reinoso B., Stutz A. M., Haemmerlé L., 2018, MNRAS, 476, 366

Boss A. P., Black D. C., 1982, ApJ, 258, 270

Bowman J. D., Rogers A. E. E., Monsalve R. A., Mozdzen T. J., Mahesh N., 2018, Nature, 555, 67

Bromm V., Coppi P. S., Larson R. B., 1999, ApJ, 527, L5

Bromm V., Coppi P. S., Larson R. B., 2002, ApJ, 564, 23

Bryan G. L., Cen R., Norman M. L., Ostriker J. P., Stone J. M., 1994, ApJ, 428, 405

Bullock J. S., Dekel A., Kolatt T. S., Kravtsov A. V., Klypin A. A., Porciani C., Primack J. R., 2001, ApJ, 555, 240

Capitelli M., Coppola C. M., Diomede P., Longo S., 2007, A&A, 470, 811

Carr B. J., 2003, in Giulini D., Kiefer C., Laemmerzahl C., eds, Lecture Notes in Physics, Berlin Springer Verlag Vol. 631, Quantum Gravity: From Theory to Experimental Search. pp 301–321 (arXiv:astro-ph/0310838), doi:10.1007/978-3-540-45230-0_7

Cen R., 1992, ApJS, 78, 341

Chandrasekhar S., 1964, Physical Review Letters, 12, 114

Chon S., Hirano S., Hosokawa T., Yoshida N., 2016, ApJ, 832, 134

Chon S., Hosokawa T., Yoshida N., 2018, MNRAS, 475, 4104

Colella P., 1990, Journal of Computational Physics, 87, 171

Coppola C. M., Longo S., Capitelli M., Palla F., Galli D., 2011, ApJS, 193, 7

Corrigan S. J. B., 1965, J. Chem. Phys., 43, 4381

Dalgarno A., Lepp S., 1987, in Vardya M. S., Tarafdar S. P., eds, IAU Symposium Vol. 120, Astrochemistry. pp 109–118

Devecchi B., Volonteri M., 2009, ApJ, 694, 302

Eisenstein D. J., Hut P., 1998, ApJ, 498, 137

Evrard A. E., 1990, ApJ, 363, 349

Fan X., et al., 2006, AJ, 132, 117

Ferland G. J., Peterson B. M., Horne K., Welsh W. F., Nahar S. N., 1992, ApJ, 387, 95

Forrey R. C., 2013, ApJ, 773, L25

Freese K., Bodenheimer P., Spolyar D., Gondolo P., 2008, ApJ, 685, L101

Galli D., Palla F., 1998, A&A, 335, 403

Galli D., Palla F., 2002, Planet. Space Sci., 50, 1197

Gay C. D., Stancil P. C., Lepp S., Dalgarno A., 2011, ApJ, 737, 44

Gerlich D., 1982, in Lindinger W., Howorka F., Maerk T. D., Egger F., eds, Symposium on Atomic and Surface Phys., 1982 Contrib..

Glover S. C. O., 2015, MNRAS, 451, 2082

Glover S. C. O., Savin D. W., 2009, MNRAS, 393, 911

Goicovic F. G., Cuadra J., Sesana A., Stasyszyn F., Amaro-Seoane P., Tanaka T. L., 2016, MNRAS, 455, 1989

Grassi T., Bovino S., Schleicher D. R. G., Prieto J., Seifried D., Simoncini E., Gianturco F. A., 2014, MNRAS, 439, 2386

Guth A. H., 1981, Phys. Rev. D, 23, 347

Haemmerlé L., Woods T. E., Klessen R. S., Heger A., Whalen D. J., 2018, MNRAS, 474, 2757

Hahn O., Abel T., 2011, MNRAS, 415, 2101

Harrison E. R., 1970, MNRAS, 147, 279

Heger A., Fryer C. L., Woosley S. E., Langer N., Hartmann D. H., 2003, ApJ, 591, 288

Heggie D. C., 1975, MNRAS, 173, 729

Hinshaw G., et al., 2007, ApJS, 170, 288

Hirano S., Hosokawa T., Yoshida N., Umeda H., Omukai K., Chiaki G., Yorke H. W., 2014, ApJ, 781, 60

Hockney R. W., Eastwood J. W., 1981, Computer Simulation Using Particles

Hosokawa T., Omukai K., Yorke H. W., 2012, ApJ, 756, 93

Hosokawa T., Yorke H. W., Inayoshi K., Omukai K., Yoshida N., 2013, ApJ, 778, 178

Hubble E., 1929, Proceedings of the National Academy of Science, 15, 168

Hut P., et al., 1992, PASP, 104, 981

Iocco F., 2008, ApJ, 677, L1

Janev R. K., Langer W. D., Evans K., 1987, Elementary processes in Hydrogen-Helium plasmas - Cross sections and reaction rate coefficients

Jessop C., Duncan M., Chau W. Y., 1994, Journal of Computational Physics, 115, 339

Johnson J. L., Bromm V., 2007, MNRAS, 374, 1557

Johnson J. L., Whalen D. J., Agarwal B., Paardekooper J.-P., Khochfar S., 2014, MNRAS, 445, 686

Karpas Z., Anicich V., Huntress W. T., 1979, J. Chem. Phys., 70, 2877

Katz H., Sijacki D., Haehnelt M. G., 2015, MNRAS, 451, 2352

Khlopov M. Y., 2010, Research in Astronomy and Astrophysics, 10, 495

Khokhlov A., 1998, Journal of Computational Physics, 143, 519

Kravtsov A. V., Klypin A. A., Khokhlov A. M., 1997, ApJS, 111, 73

Kreckel H., Bruhns H., Čížek M., Glover S. C. O., Miller K. A., Urbain X., Savin D. W., 2010, Science, 329, 69

Krumholz M. R., McKee C. F., Klein R. I., 2004, ApJ, 611, 399

Latif M. A., Ferrara A., 2016, PASA, 33, e051

Latif M. A., Volonteri M., 2015, MNRAS, 452, 1026

Latif M. A., Schleicher D. R. G., Schmidt W., Niemeyer J., 2013a, MNRAS, 430, 588

Latif M. A., Schleicher D. R. G., Schmidt W., Niemeyer J. C., 2013b, MNRAS, 436, 2989

Latif M. A., Bovino S., Van Borm C., Grassi T., Schleicher D. R. G., Spaans M., 2014a, MNRAS, 443, 1979

Latif M. A., Schleicher D. R. G., Bovino S., Grassi T., Spaans M., 2014b, ApJ, 792, 78

Latif M. A., Bovino S., Grassi T., Schleicher D. R. G., Spaans M., 2015, MNRAS, 446, 3163

Latif M. A., Lupi A., Schleicher D. R. G., D'Amico G., Panci P., Bovino S., 2018, arXiv e-prints,

Lemaître G., 1931, MNRAS, 91, 490

Martel H., Shapiro P. R., 1998, MNRAS, 297, 467

Martin P. G., Schwarz D. H., Mandy M. E., 1996, ApJ, 461, 265

Mielke S. L., Peterson K. A., Schwenke D. W., Garrett B. C., Truhlar D. G., Michael J. V., Su M.-C., Sutherland J. W., 2003, Physical Review Letters, 91, 063201

Mitchell G. F., Deveau T. J., 1983, ApJ, 266, 646

Miyake S., Stancil P. C., Sadeghpour H. R., Dalgarno A., McLaughlin B. M., Forrey R. C., 2010, ApJ, 709, L168

Mortlock D. J., et al., 2011, Nature, 474, 616

Navarro J. F., White S. D. M., 1993, MNRAS, 265, 271

Omukai K., 2001, ApJ, 546, 635

Oosterom A. V., Strackee J., 1983, IEEE Transactions on Biomedical Engineering, BME-30, 125

Pacucci F., Ferrara A., Marassi S., 2015a, MNRAS, 449, 1076

Pacucci F., Volonteri M., Ferrara A., 2015b, MNRAS, 452, 1922

Pacucci F., Ferrara A., Grazian A., Fiore F., Giallongo E., Puccetti S., 2016, MNRAS, 459, 1432

Pagels H. R., 1983, Astrophys. Lett., 23, 151

Peebles P. J. E., 1968, ApJ, 153, 1

Peebles P. J. E., 1969, ApJ, 155, 393

Peirani S., Mohayaee R., de Freitas Pacheco J. A., 2004, MNRAS, 348, 921

Penzias A. A., Wilson R. W., 1965, ApJ, 142, 419

Perlmutter S., et al., 1998, Nature, 391, 51

Perlmutter S., et al., 1999, ApJ, 517, 565

Planck Collaboration et al., 2016, A&A, 594, A13

Portegies Zwart S. F., McMillan S. L. W., 2002, ApJ, 576, 899

Portegies Zwart S. F., Makino J., McMillan S. L. W., Hut P., 1999, A&A, 348, 117

Poulaert G., Brouillard F., Claeys W., McGowan J. W., Van Wassenhove G., 1978, Journal of Physics B Atomic Molecular Physics, 11, L671

Press W. H., Teukolsky S. A., Vetterling W. T., Flannery B. P., 1992, Numerical recipes in FORTRAN. The art of scientific computing

Rees M. J., 1978, The Observatory, 98, 210

Regan J. A., Haehnelt M. G., 2009, MNRAS, 396, 343

Reinoso B., Schleicher D. R. G., Fellhauer M., Klessen R. S., Boekholt T. C. N., 2018, A&A, 614, A14

Ricotti M., Ostriker J. P., Mack K. J., 2008, ApJ, 680, 829

Riess A. G., et al., 1998, AJ, 116, 1009

Sakurai Y., Hosokawa T., Yoshida N., Yorke H. W., 2015, MNRAS, 452, 755

Saltzman J., 1994, Journal of Computational Physics, 115, 153

Savin D. W., 2001, ArXiv Astrophysics e-prints,

Savin D. W., Krstić P. S., Haiman Z., Stancil P. C., 2004, ApJ, 606, L167

Schleicher D. R. G., Palla F., Ferrara A., Galli D., Latif M., 2013, A&A, 558, A59

Schmidt B. P., et al., 1998, ApJ, 507, 46

Shang C., Bryan G. L., Haiman Z., 2010, MNRAS, 402, 1249

Shapiro S. L., 2003, in Centrella J. M., ed., American Institute of Physics Conference Series Vol. 686, The Astrophysics of Gravitational Wave Sources. pp 50–60 (arXiv:astro-ph/0310070), doi:10.1063/1.1629414

Shavitt I., 1959, J. Chem. Phys., 31, 1359

Shchekinov Y. A., Vasiliev E. O., 2006, MNRAS, 368, 454

Spolyar D., Freese K., Gondolo P., 2008, Physical Review Letters, 100, 051101

Springel V., et al., 2005, Nature, 435, 629

Steigman G., 2007, Annual Review of Nuclear and Particle Science, 57, 463

Stenrup M., Larson Å., Elander N., 2009, Phys. Rev. A, 79, 012713

Stone N. C., Küpper A. H. W., Ostriker J. P., 2017, MNRAS, 467, 4180

Susa H., Hasegawa K., Tominaga N., 2014, ApJ, 792, 32

Teyssier R., 2002, A&A, 385, 337

Toomre A., 1964, ApJ, 139, 1217

Truelove J. K., Klein R. I., McKee C. F., Holliman II J. H., Howell L. H., Greenough J. A., 1997, ApJ, 489, L179

Turk M. J., Smith B. D., Oishi J. S., Skory S., Skillman S. W., Abel T., Norman M. L., 2011, The Astrophysical Journal Supplement Series, 192, 9

Verner D. A., Ferland G. J., 1996, ApJS, 103, 467

Volonteri M., 2010, A&A Rev., 18, 279

Volonteri M., Bellovary J., 2012, Reports on Progress in Physics, 75, 124901

Volonteri M., Silk J., Dubus G., 2015, ApJ, 804, 148

Wolcott-Green J., Haiman Z., Bryan G. L., 2011, MNRAS, 418, 838

Wu X.-B., et al., 2015, Nature, 518, 512

Yoshida N., Omukai K., Hernquist L., Abel T., 2006, ApJ, 652, 6

Zeldovich Y. B., 1972, MNRAS, 160, 1P

Zeldovich Y. B., Kurt V. G., Syunyaev R. A., 1968, Zhurnal Eksperimentalnoi i Teoreticheskoi Fiziki, 55, 278

de Jong T., 1972, A&A, 20, 263

del Valle L., Escala A., 2014, ApJ, 780, 84

del Valle L., Escala A., 2015, Astronomische Nachrichten, 336, 820